FABRICATION METHODOLOGIES FOR INTEGRATED PHOTONIC DEVICES IN LITHIUM NIOBATE

DENG JUN

(B.Sc., University of Electronic Science and Technology of China)

A THESIS SUBMITTED

FOR THE DEGREE OF DOCTOR OF PHILOSOPHY

DEPARTMENT OF ELECTRICAL AND COMPUTER ENGINEERING

NATIONAL UNIVERSITY OF SINGAPORE

2013

DECLARATION

I hereby declare that the thesis is my original work and it has been written by me in its entirety.

I have duly acknowledged all the sources of information which have been used in the thesis.

This thesis has also not been submitted for any degree in any university previously.

Deng Jun
08 August 2013

Acknowledgments

This thesis would have been impossible without the contributions and kind help of my mentors, colleagues and friends.

First and foremost, I would like to express my sincerest and earnest appreciation to my supervisor, Prof. Aaron J. Danner, for his immense guidance, endless support and kind encouragement throughout the whole PhD journey. It was an honor for me to work with him and I will never forget his encouragement to me: “Yes you will”.

I would also like to deeply thank my co-supervisor Dr. Ching Eng Png for his insightful suggestions and enormous supports during the whole study. I would like to express my special thanks to Prof. Noriaki Toyoda of the University of Hyogo for our collaborations on the GCIB technique and for allowing me to visit his laboratory. I also greatly thank Dr. Lim Soon Thor of IHPC for his valuable suggestions on Rsoft simulations.

My special thanks to Dr. Sudheer K. Vanga of the NUS Physics Department for his kind help in implantation processes, and for teaching me about optical measurements and allowing me to use their measurement setup.

I would like express my appreciations to Dr. Jia Wei and Dr. Xin Maoqing for their valuable advice on my PhD studies and research projects. I would like to thank Dr. Si Guangyuan for helping me in FIB milling and proton exchange methods. I am very grateful to Mr. Sajid Hussain for his valuable help in electron beam lithography. I would also like to thank my colleagues: Ms. Wong E. Laine, Mr. Le Hong Vu, Mr. Mridul Sakhujia, Mr. Lamine Benaissa, Dr. Liang Guanquan and Mr. Siew Shawn Yohanes. My

gratitude goes to all of them.

Last but not least, I dedicate this thesis to my parents who love me and support me through all my life.

08 August 2013

Table of Contents

Acknowledgments....i

Table of Contents iii

Abstract....vi

List of Tables.... viii

List of Figures....ix

List of Abbreviations....xvi

Chapter 1 Introduction 1

1.1 Background and motivation....1

1.2 Lithium niobate: an overview 4

1.2.1 Crystal growth....4

1.2.2 Optical properties of $LiNbO_3$....5

1.2.3 $LiNbO_3$ modulators and fabrication methods 7

1.3 Research objectives....12

1.4 Outline of thesis 13

References....14

Chapter 2 Characterization of ICP etched $LiNbO_3$....19

2.1 Introduction....19

2.1.1 Plasma etching methodology 19

2.1.2 Literature review of $LiNbO_3$ etching 22

2.1.3 Motivation....26

2.2 Fabrication procedures....27

2.3. Etching characterization under different metallic masks and gas compositions 29

2.4 Deep anisotropic etching....33

2.4.1 Image reversal mode of photoresist 34

2.4.2 The effect of He backside cooling 36

2.4.3 The effect of RIE power....40

2.4.4 The effect of total gas flow and deep etching 43

2.5 Reducing the sidewall roughness with GCIB techniques....46

2.5.1 Introduction of the GCIB technique 47

2.5.2 Results of Ar GCIB irradiations on etched $LiNbO_3$ structures

....49
2.6 Conclusion 52
References...53

Chapter 3 Suspended structures in $LiNbO_3$ 57

3.1 Introduction...57
3.1.1 Literature review of ion implantation used in $LiNbO_3$ photonic device fabrication..57
3.1.2 Motivation...62
3.2 Fabrication procedures...63
3.3 Fabrication of three-dimensional optical microstructures 69
3.3.1 Suspended microwires 69
3.3.2 Suspended microdisks..73
3.3.3 Mechanical problems related to suspended microstructures ..74
3.3.4 The significance of PhC profile in a suspended membrane....76
3.4 Conclusion 78
References...78

Chapter 4 Fano resonances of free-standing $LiNbO_3$ PhC slabs 82

4.1 Introduction...82
4.1.1 Photonic crystals 82
4.1.2 Guided resonances – Fano resonances in PhC slabs..............85
4.1.3 Literature review of guided resonances 87
4.1.4 Motivation of investigating guided resonances of free-standing $LiNbO_3$ PhC slabs 91
4.2 Numerical modeling of $LiNbO_3$ PhC slabs.......................................93
4.2.1 The effect of slab thickness on transmission properties 95
4.2.2 The effect of lattice types on transmission properties.............98
4.2.3 The effect of radius of air holes on transmission properties .100
4.2.4 The effect of polarization of incident light on transmission properties...101
4.2.5 The effect of asymmetrical structures on transmission properties 103
4.3 Fabrication of free-standing $LiNbO_3$ PhC slabs 105
4.4 Optical characterization 109
4.4.1 Measurement setup 109
4.4.2 Measurement results of free-standing $LiNbO_3$ PhC slabs with different dimensions...110
4.5 Conclusion 113

References 115
Chapter 5 $LiNbO_3$ PhC waveguide 119
5.1 Introduction 119
5.1.1 APE technique 120
5.1.2 PhCs in APE waveguides 122
5.2 Fabrication procedures 124
5.3 Composition characterization by SIMS 128
5. 4 Optical characterization 129
5.4.1 APE waveguide measurement results 129
5.4.2 Transmission spectrum of PhC waveguide 132
5.5 Conclusion 134
References 134
Chapter 6 Conclusion and Future Work 138
6.1 Conclusion 138
6.2 Future Work 140
6.2.1 Extended research on free-standing PhC slabs 140
6.2.2 Optical microcavities fabrication in APE waveguides and nonlinear effect investigation 141
6.2.3 Ring resonators used in microwave photonics 142
References 146
Appendix: publications 147

Abstract

$LiNbO_3$ is one of the most commonly used materials in active photonic devices. It is desirable to build photonic integrated circuits on the $LiNbO_3$ platform for next generation communication networks. However, the fabrication of integrated $LiNbO_3$ devices is still quite challenging due to the well-known resistance of the material to dry etching. This thesis explores different fabrication methods to solve these issues and realize significant structures including deep anisotropic ridges, suspended membranes and photonic crystal slabs on bulk $LiNbO_3$. The optical properties of photonic crystals on $LiNbO_3$ were studied theoretically and experimentally in order to explore their potential for compact and low loss $LiNbO_3$ photonic integrated circuits.

Firstly, we performed a detailed examination of inductively coupled plasma etching methods. Smooth etched surfaces were obtained by using Cr as an etching mask combined with SF_6/Ar etching gases. The influences of He backside cooling, power, and gas flows were investigated in detail. Deep (> 3 μm) and highly anisotropic $LiNbO_3$ etching with smooth surfaces was achieved in a single-step run. Ar gas cluster ion beam irradiation was employed to smooth the rough sidewalls of etched $LiNbO_3$ structures for the first time.

Secondly, a monolithic approach to fabricate suspended $LiNbO_3$ structures is demonstrated by employing ion implantation and selective wet etching. Three-dimensional microstructures such as suspended wires and microdisks were successfully fabricated. Free-standing $LiNbO_3$ photonic

crystal slabs with vertical sidewall air holes were also fabricated and their Fano resonance phenomena were systematically investigated for the first time. Numerical simulations were performed to analyze the transmission spectrum under free-space illumination and results showed that resonant modes could be controlled by varying design parameters such as radii of holes, slab thickness and polarization of incident light. Optical measurements of fabricated photonic crystal slabs were carried out and were in good agreements with simulation results. These results confirm that such device has great potential for active photonic integrated circuits.

Thirdly, we performed an exploratory study on in-plane transmission properties of photonic crystals by incorporating them into an annealed proton exchange $LiNbO_3$ waveguide by focused ion beam milling. A channel waveguide with 2.5 μm depth and 6 μm width was fabricated by immersing $LiNbO_3$ wafers in molten benzoic acid. Our results showed that thermal annealing was an effective method to reduce propagation loss in proton exchange $LiNbO_3$ waveguides. A photonic band gap was observed and the extinction ratio was estimated to be 15 dB. Such incorporation of photonic crystals into channel waveguides should provide new strategies for decreasing interaction length in $LiNbO_3$ modulators, which is a key challenge for future work.

List of Tables

Table 2.1: Summary of recent work on dry etching of $LiNbO_3$......................24

Table 2.2: Plasma etching parameters, average etching rates and selectivities. 33

Table 4.1: 3D FDTD simulation parameter setup for 2D PhC $LiNbO_3$ slab. ..95

List of Figures

Figure 1.1: Configuration of a MZI modulator in x-cut $LiNbO_3$ [29]. 8

Figure 1.2: An example of etched ridge $LiNbO_3$ waveguides [30].................10

Figure 1.3: Schematic illustration of the $LiNbO_3$ channel waveguides formation using O^{2+} implantation [31]. 10

Figure 1.4: An ion sliced $LiNbO_3$ thin film bonded on a BCB layer [32]. 11

Figure 2.1: Schematic diagram of the ICP system used in this work. 22

Figure 2.2: Setup of PE process..28

Figure 2.3: Illustration of the ridge structures fabrication process. 29

Figure 2.4: SEM image of etched $LiNbO_3$ with Ag as an etching mask. The $LiNbO_3$ substrate shows better surface condition than mask area...30

Figure 2.5: SEM images of the surface condition of etched $LiNbO_3$ with Ni as etching mask. (a) Image of etched $LiNbO_3$ using a SF_6/Ar gas mixture. The Ni mask remains on the surface; (b) Image of etched $LiNbO_3$ using a CHF_3/Ar gas mixture. (The Ni mask had already been removed by wet etching.)...30

Figure 2.6: (a) SEM image of etched $LiNbO_3$ using a Cr mask and a CHF_3/Ar gas mixture. The surface is very rough; (b) SEM image of etched $LiNbO_3$ using a Cr mask and a SF_6/Ar gas mixture........................31

Figure 2.7: (a) Top view of fabricated ridge waveguide on $LiNbO_3$ with smooth surface; (b) SEM image showing cross section of the ridge waveguide. 33

Figure 2.8: SEM images of top view of Cr patterns on $LiNbO_3$ after lift-off (a) with normal positive AZ5214E and (b) with image reverse mode of

AZ5214E. Schematics of different photoresist sidewall slopes: (c) positive sidewall slope and (d) negative sidew 35

Figure 2.9: (a) – (e) Illustration of AZ5214E patterning process using image reversal mode; (f) SEM image showing a cross section of AZ5214E in image reversal mode. 36

Figure 2.10: SEM cross-sectional image of a perfect rectangular etched structure with 90° slope angle at 90/800 W (RIE/ICP power), 7 mTorr pressure. 38

Figure 2.11: SEM images of etched $LiNbO_3$ surface condition at (a) continuous mode (b) intermittent mode. 40

Figure 2.12: $LiNbO_3$ etching rate as a function of RIE power. 41

Figure 2.13: SEM images of the etched $LiNbO_3$ surface condition with different RIE power at (a) 60 W (b) 90 W (c) 150 W. 41

Figure 2.14: SEM images of etched $LiNbO_3$ cross section with RIE power at (a) 60 W (b) 90 W (c) 150 W. Slope angles are shown. 42

Figure 2.15: $LiNbO_3$ etching rate as a function of total gas flow. The ratio of SF_6 and Ar is fixed at 1:1. 43

Figure 2.16: SEM images of etched $LiNbO_3$ cross section with slope angle at different total gas flow of (a) 10 sccm (b) 30 sccm (c) 60 sccm. 45

Figure 2.17: SEM images of deep and highly anisotropic $LiNbO_3$ etching at 3.5 μm depth under 800 W ICP power, 90 W RIE power, 7 mTorr pressure, and 50 sccm SF_6/Ar gas mixture. The total etching time is 30 minutes. 46

Figure 2.18: Schematic diagram of a GCIB system [23]. 48

Figure 2.19: Illumination of the sample holder and the ion irradiation direction. 49

Figure 2.20: SEM images of the surface and sidewall conditions of etched $LiNbO_3$ structures. (a) before GCIB process; (b) after GCIB process. 50

Figure 2.21: SEM images of etched $LiNbO_3$ after GCIB with 20 KeV Ar irradiations. (a) ion dose=3×10^{16} ions/cm^2; (b) ion dose=1×10^{17} ions/cm^2; (c) ion dose=2×10^{17} ions/cm^2..51

Figure 3.1: Fabrication process of a three-dimensional microstructure.. 62

Figure 3.2: Schematic of ion implantation process (left) and a simulated ion distribution in $LiNbO_3$ after implantation by SRIM (right). 65

Figure 3.3: Fabrication process of the suspended $LiNbO_3$ structures.............65

Figure 3.4: A pattern milled on an implanted $LiNbO_3$ substrate by FIB. 66

Figure 3.5: SEM images of the cross section of implanted $LiNbO_3$ samples after wet etching. 68

Figure 3.6: Fabricated suspended waveguide with a length of 35 μm, a width of 1.2 μm and an air gap of 1.1 μm. (a) View at an angle of 45°; (b) View at an angle of 70°; (c) Top view. 69

Figure 3.7: Fabricated suspended waveguide with a length of 35 μm, a width of 550 nm. (a) View at an angle of 45°; (b) Top view. 71

Figure 3.8: Two examples of the suspended structures with large width on samples implanted by (a) 1 MeV, 1.1 MeV and 1.23 MeV; (b) 400 KeV, 500 KeV and 650 KeV. 72

Figure 3.9: Fabricated suspended microdisk with a diameter of 13.3 μm and an air gap of 1.1 μm between micodisk and $LiNbO_3$ substrate. 74

Figure 3.10: SEM image of a cracked suspended wire..................................75

Figure 3.11: A buckling phenomenon occurred in a suspended wire. 75

Figure 3.12: (a) Typical cross section of air holes milled by FIB; (b) cross section of truncated air holes in a suspended slab. The measured slope angle of the holes in the slab is 89°. The part of the hole with a conical shape is truncated by the air gap, of which the measured slope angle is less than 40°. 77

Figure 4.1: 2D PhC slab patterned by square lattice of holes in a dielectric slab with radius of air holes (*r*), lattice constant (*a*) and slab thickness (*t*) indicated. 84

Figure 4.2: Band diagram of a typical 2D PhC slab. 85

Figure 4.3: (a) Schematic of a PhC slab with square lattice of air holes under free-space illumination. Fano resonant peaks occur in the transmission and reflectance spectrum; (b) A simulated transmission spectrum of PhC slab under free-space illumination, which exhibits a sharp asymmetric shape due to the Fano resonance [7]..................86

Figure 4.4: PhC slab structure with rectangular air holes in order to achieve polarization control on transmission spectrum [19]........................88

Figure 4.5: Fabrication process for PhC slabs transferred on PET substrate. (a) Single layer PhC pattern; (b) Release; (c) Transfer; (i) SEM image of top and (ii) side view of patterned Si PhC slabs on SOI substrate; (iii) SEM image of patterned Si PhC slab after removing the oxidation layer; (iv) a micrograph of a 3 $\times$ 3 mm patterned Si PhC slab transferred onto 1 inch $\times$ 1 inch flexible PET substrate [25]. 91

Figure 4.6: Side view of a 3D FDTD simulation layout. The entire simulation domain with two monitors is shown with purple lines. The top right of the layout shows the coordinate system. 94

Figure 4.7: Simulated normal-incident transmission spectra of PhC slabs with various slab thicknesses (a) 300 nm; (b) 700 nm; (c) 1500 nm. The lattice constant (*a*) and radius (*r*) of holes keep the same value: a = 900 nm and a ratio of r/a = 0.28. 97

Figure 4.8: Comparison of simulated transmission spectra of PhC slabs for

different lattice types. The transmission spectra of PhC slabs with a square lattice are shown with solid lines, while transmission spectra of PhC slabs with a triangular lattice are shown with dashed lines. (a) The structure consists of a slab thickness t = 800 nm, lattice constant a = 800 nm and the ratio of r/a = 0.1; (b) The structure consists of a slab thickness t = 800 nm, lattice constant a =800nm and the ratio of r/a = 0.31 99

Figure 4.9: Comparison of simulated transmission spectra of triangular lattice PhC slabs with a radius of (a) r / a = 0.1; (b) r / a = 0.153; (c) r / a = 0.26; (d) r / a =0.31. The lattice constant (a) and slab thickness (t) are kept at: a =800 nm, t =800 nm. 101

Figure 4.10: (a) Comparison of simulated transmission spectra of polarized light normally incident on a $LiNbO_3$ PhC slab.. 102

Figure 4.11: Side view of 3D FDTD simulation layout for the asymmetrical structure in a $LiNbO_3$ PhC slab. 104

Figure 4.12: Comparison of the transmission spectra between a free standing membrane and a slab over a substrate with only a 200 nm air gap. 105

Figure 4.13: Fabrication process of free-standing PhC Slabs. 1. The x-cut $LiNbO_3$ wafer; 2. He implantation with multi-energy; 3. Focused ion beam milling to pattern PhCs; 4. Wet etching by immersing the wafer into acid. The acid reaches the damaged layer through the air holes to form the suspended PhC slabs. 105

Figure 4.14: SEM image showing a cross section of free-standing PhC slabs. An air gap formed by wet etching is clearly visible. 107

Figure 4.15: SEM images of the fabricated free-standing PhC slabs in $LiNbO_3$. 1. Square lattice with lattice constant a = 800 nm and r/a = 0.308 (a) view with a tilt angle of 45°; after wet etching the air holes become slightly elliptically shaped instead of circularly shaped; (b) Side view; 2. Square lattice with lattice constant a =1000 nm and radius of r/a = 0.15 (c) view with a tilt angle of 45°; (d) Side view. 108

Figure 4.16: (a) Side view of the etching profile in a suspended membrane. The thickness of membrane is not uniform; (b) Side view of PhC slabs fabricated in our procedure. The uniform slab thickness is obvious. 109

Figure 4.17: (a) microspectrophotometer; (b) Schematic for reflection measurement. 110

Figure 4.18: Reflection spectra of un-polarized light incident normally on a fabricated PhC slab. Red solid line—measured reflection spectra. Blue dashed line—simulated reflection spectra............................ 111

Figure 4.19: (a) Comparison of measured normal-incidence reflection spectrum of the fabricated PhC slabs with square array of holes with different radii: 260 nm and 330 nm.The lattice constant for both structures is the same: a =1000 nm; (b)SEM images of the two PhC slabs viewed with a tilted angle of 60°. 112

Figure 4.20: (a) Measured normal-incidence reflection spectrum of the fabricated PhC slabs with square array of holes with a lattice constant of 1.2 μm and radius of 300 nm; (b) SEM images of the PhC slab viewed with a tilted angle of 45°...113

Figure 5.1: Illustration of the process steps to create PhC in an APE waveguide. (a) Cr deposition; (b) Photolithography; (c) Ion milling; (d) PE process; (e) PhC milled by FIB..126

Figure 5.2: SEM image of a fabricated squared lattice PhC on a 6 μm APE waveguide. Light propagates along the y direction of the $LiNbO_3$ crystal..127

Figure 5.3: SIMS profile of the concentration of Li and Nb vs depth, obtained after PE at 235^oC for 5 hours without annealing. 129

Figure 5.4: Schematic of the transmission spectra measurement. 130

Figure 5.5: (a) Light of TE mode propagates a 6 μm APE waveguide; (b) light of TM mode incidents to the APE waveguide and a weak coupling

occurs; (c) CCD image of the APE waveguide illuminated at a wavelength of 532 nm; (d) the output of waveguide is collected using a lensed fiber. 131

Figure 5.6: Transmission spectra of the APE channel waveguide before and after thermal annealing. 131

Figure 5.7: (a) Light of TE mode propagates through a PhC waveguide; (b) Measured optical transmission spectra through the PhC (red line) and through a standard APE $LiNbO_3$ waveguide (black line). 133

Figure 6.1: Optical microscope image showing SHG in an APE $LiNbO_3$ waveguide. 142

Figure 6.2: Configuration of a ring resonator in $LiNbO_3$. 143

Figure 6.3: Top view of the coupling area when light passed through the waveguide. 144

Figure 6.4: (a) Measurement setup to test EO tunability of the $LiNbO_3$ ring resonator; (b) Optical microscope image showing the two probes. 144

Figure 6.5: Normalized transmission spectra of the ring resonator before (red line) and after (green line) applying voltage (150 V). 145

List of Abbreviations

APE	annealed proton exchange
BCB	benzocyclobutene
CIS	crystal ion slicing
DBR	distributed bragg reflector
EO	electro–optic
FDTD	Finite-Difference Time-Domain
FIB	focused ion beam
GaN	gallium nitride
GaAs	gallium arsenide
GCIB	gas cluster ion beam
IBEE	ion beam-enhanced etching
InP	indium phosphide
ICP	inductively coupled plasma
LPE	liquid phase exitaxy
$LiNbO_3$	lithium niobate
MEMS	microelectromechanical systems
MZI	Mach–Zehnder interferometer
NLD	neutral loop discharge
PhC	photonic crystal
PIC	photonic integrated circuit
PML	perfectly matched layer
PE	proton exchange
PBG	photonic band gap
RIE	reactive ion etching
SOI	Silicon-On-Insulator
SIMS	secondary ion mass spectroscopy
SEM	scanning electron microscopy
SRIM	stopping and range of ions in matter
TIR	total internal reflection
VCSEL	vertical-cavity surface-emitting lasers

Chapter 1 Introduction

1.1 Background and motivation

Over the last decade telecommunication networking infrastructure has greatly expanded due to an increasing demand for bandwidth. After the invention of optical fiber, fiber-optic communication systems have become the dominant form of networking due to the large spectral bandwidth available. A typical fiber optical system contains many components including a light source (laser), an electrical amplifier, a modulator, optical fibers and a detector. Although these components have individually become faster and efficient, the integration of them into a single module is still a technical challenge, and this integration represents a major cost factor. It is thus highly desirable to build photonic integrated circuits (PICs), which would have considerable advantages over traditional fiber optical systems, such as compact size, low optical loss and low power consumption. Besides telecommunications, PICs can also be applied to many fields like optical computing and microelectromechanical systems (MEMS) to deliver more functionality.

Nowadays many materials systems are used to build optical components, such as Silicon-On-Insulator (SOI), lithium niobate ($LiNbO_3$), gallium arsenide (GaAs) and indium phosphide (InP). Among these materials, $LiNbO_3$ is extremely important in integrated and nonlinear optical device use because of its strong electro–optic (EO) coefficients, large transparency range and wide intrinsic bandwidth [1]. Due to its excellent EO and nonlinear properties, $LiNbO_3$ has found various applications in integrated optics. For example, $LiNbO_3$ external modulators, which provide large modulation bandwidth as

well as zero-chirp operation, play a key role in high speed communication systems [2]. Besides, $LiNbO_3$ can be also used in optical amplifiers [3], surface acoustic wave (SAW) devices [4], tunable filters (switching time < 50ns) [5], nonlinear wavelength converters [6] and all-optical switches [7]. Additionally, it can also be periodically poled, allowing quasi-phase matching (QPM) to obtain second harmonic generation (SHG) [8].

Most optical elements on the $LiNbO_3$ platform are based on a guided wave configuration. In such a structure, planar or channel waveguides are critical and even indispensable components. Waveguides in $LiNbO_3$ crystals are traditionally fabricated by metal diffusion [9], proton exchange (PE) [10], and ion irradiation [11]. These methods, while well-established, have the drawback of small index contrast yields and subsequently weak guiding. For example, the Ti-indiffusion method only introduces an ordinary index change less than 0.01 and an extraordinary index change of 0.02 at λ=1.523 μm [12]. Meanwhile, resultant waveguides engineered with such a small index contrast cannot be bent with a small radius of curvature because of large bending losses. Consequently it is difficult to realize high density optical circuits as compact as their electronic counterparts or even as compact as equivalent structures built in the SOI system with its larger index contrast. These drawbacks are already obvious in commercial modulators. A high speed modulator requires considerably long interaction arms and traveling-wave electrodes, which lead to an overall typical device length of 3 to 5 centimeters [13].

Although ridge waveguides have been fabricated to improve the confinement of optical modes in $LiNbO_3$ modulators [14, 15], a long interaction length on the order of millimeters is still required to achieve the necessary velocity match between the optical and the microwave signals on

the driving electrodes. In addition, most developed ridged modulators are based on a combination of channel diffused waveguides and subsequent selective etching of ridges. Diffused waveguides cannot provide a high refractive index contrast in the vertical direction on their own. Furthermore, sidewall and surface roughness owing to high etching resistance of $LiNbO_3$ also limits the ridge depth. Because of these serious fabrication limitations, there is still much work that can be pursued in the area of $LiNbO_3$ modulator fabrication with deep ridge structures, which can be further developed to provide low loss devices and reduce component size.

Besides waveguides, many other novel optical components have been developed in various materials systems in order to achieve interesting/improved device performance and new applications, like photonic crystals (PhCs), microring resonators and microdisks. These components provide unique functionalities and are promising candidates for use in components in next generation communication networks. For example, the slow light effect in PhCs, in which low group velocities occur in the vicinity of photonic band edges, is a promising tool for shrinking the interaction length of modulators and enhance light–matter interactions [16, 17]. Another example is the whispering gallery modes in microdisk resonators with light localized near the microdisks' rim. Such resonators provide many unique features like narrow resonant line widths, high quality factors and large free spectral ranges [18, 19]. These components have already been fabricated in many other materials like GaAs [20], SOI [21] and gallium nitride (GaN) [22]. For example, McNab *et al.* already fabricated membrane-type PhC waveguides on SOI wafers [23]. In this type of structure, Si mode confinement in the vertical direction is accomplished by index guiding, while lateral confinement

within the silicon slab plane is defined by a photonic band gap (PBG). Losses for these devices have been reduced to only 8 dB/cm. However, such PhCs are very difficult to realize on bulk $LiNbO_3$ due to the well-known resistance of this material to standard fabrication techniques, so much work remains to implement many of these recent advances in this important material system.

Due to the unique optical properties of $LiNbO_3$ such as acousto-optic, EO, piezoelectric, and ferroelectric effects, this material, especially single crystal bulk $LiNbO_3$, plays an extremely important role in integrated optics. In view of the fast response of the EO effect and excellent nonlinear properties, $LiNbO_3$ cannot always be replaced by other materials in the field of integrated optics. For example, the Pockels effect in $LiNbO_3$ is much faster and the loss is much lower than carrier-induced index changes in silicon-based devices. As a result, modulators based on $LiNbO_3$ still dominate in the high speed modulator market. Consequently, it is necessary to develop novel optical components like PhCs in the $LiNbO_3$ platform.

1.2 Lithium niobate: an overview

1.2.1 Crystal growth

The first $LiNbO_3$ crystals were fabricated from a Li_2O-Nb_2O_5 melt composition in 1949 [24]. The congruent composition for the starting materials contains 45 to 50 mol% Li_2O. Crystals grown from different compositions exhibit variations in the Li/Nb ratio and optical properties. For example, a crystal grown from melts with a composition ranging between 47.8 and 48.8 mol% Li_2O exhibit a range in extraordinary index of 50×10^{-4} [25]. Because of fast growth techniques and good homogeneity, nowadays most

single crystal $LiNbO_3$ wafers are grown from a melt of congruent composition using the Czochralski technique [26].

At temperatures below its Curie point (about 1200°C), $LiNbO_3$ is a negative uniaxial crystal and the crystalline structure corresponds to the trigonal *3m* point group. Both the Li and Nb atoms are located on the three-fold symmetry axis. In the trigonal system both hexagonal and rhombohedral unit cells can be chosen. In the conventional hexagonal unit cell, the crystal exhibits three-fold rotation symmetry about the z axis (which is called the optical axis). The three equivalent axes lie in a plane normal to the z axis. Above the Curie temperature the crystal transits from a ferroelectric phase into a paraelectric phase and loses its strong dipole moment. In the paraelectric phase many excellent optical features of $LiNbO_3$ vanish. However, because the Curie temperature of $LiNbO_3$ is so high, a wide range of operation temperatures of $LiNbO_3$ devices is possible.

1.2.2 Optical properties of $LiNbO_3$

In this section we discuss the properties of $LiNbO_3$ relative to optical device applications.

In the principal coordinate system of $LiNbO_3$, the dielectric permittivity ε is a second-rank tensor which can be expressed by the following matrix:

$$\varepsilon_{ij} = \begin{pmatrix} \varepsilon_{11} & 0 & 0 \\ 0 & \varepsilon_{22} & 0 \\ 0 & 0 & \varepsilon_{33} \end{pmatrix} \qquad (1-1)$$

it can be seen that only the diagonal elements of the permittivity tensor are non-zero. Moreover, in $LiNbO_3$ $\varepsilon_{11} = \varepsilon_{22}$, which means that the permittivity is the same for any electric field direction in the plane perpendicular to the z axis. $LiNbO_3$ is an anisotropic material. Light propagating in $LiNbO_3$

experiences a refractive index which depends on its polarization and propagation directions. A construction can be used to understand how the refractive index changes with the polarization and propagation states, which is known as an index ellipsoid. The refractive index in an arbitrary direction can be obtained from this index ellipsoid.

The birefringence of $LiNbO_3$ is defined as the difference (n_e-n_o), where n_o is the ordinary refractive index and n_e is the extraordinary refractive index. The ordinary index corresponds to light polarized in the plane perpendicular to the z axis. The extraordinary index corresponds to light polarized along the z axis, and this is smaller than the ordinary index in $LiNbO_3$.

One of the most important features of $LiNbO_3$ is its excellent EO effect. When light propagates in $LiNbO_3$ in the presence of an externally-applied electric field, the refractive indices can be changed. The Pockels effect describes the linear relationship between the index change and the electric field, while the Kerr effect describes the quadratic relationship between the index change and electric field. Here we only introduce the Pockels effect since most electro-optic modulators are based on it, and because it is significantly larger than the Kerr effect here. Traditionally the Pockels effect can be expressed as

$$\Delta(1/n^2)_{ij} = \sum_k r_{ijk} E_k \qquad (1-2)$$

where n is the refractive index, r_{ijk} are the elements of the second-order EO tensor and E_k are the applied electric fields.

With application of contracted notation and the $3m$ symmetry of $LiNbO_3$, the EO tensor can be reduced to a 6×3 matrix,

$$r_{ijk} = \begin{pmatrix} 0 & -r_{22} & r_{13} \\ 0 & r_{22} & r_{13} \\ 0 & 0 & r_{33} \\ 0 & r_{42} & 0 \\ r_{42} & 0 & 0 \\ -r_{22} & 0 & 0 \end{pmatrix} \qquad (1-3)$$

where r_{33}=30.8 pm/V, r_{13}=8.6 pm/V, r_{22}=3.4 pm/V and r_{42}=26 pm/V. Assuming the electric field is applied along the z axis of $LiNbO_3$, and since the EO coefficients are very small, the refractive index change due to the electric field can be expressed as

$$\Delta n_x = -\frac{1}{2} n_o^3 r_{13} E_z \qquad (1-4)$$

$$\Delta n_y = -\frac{1}{2} n_o^3 r_{13} E_z \qquad (1-5)$$

$$\Delta n_z = -\frac{1}{2} n_e^3 r_{33} E_z \qquad (1-6)$$

It can be seen that a large extraordinary index change can be achieved in $LiNbO_3$ due to its large r_{33} value. This feature helps $LiNbO_3$ stand out from other materials. The EO effect is wavelength dependent and the dispersion properties have been studied in detail in references [27, 28]. They showed that when the wavelength becomes shorter, the EO effect becomes stronger.

1.2.3 $LiNbO_3$ modulators and fabrication methods

Based on the Pockels effect, modulators which transfer information into optical waves can be realized in the $LiNbO_3$ system. Commercial $LiNbO_3$ modulators are usually designed based on a Mach–Zehnder interferometer (MZI) configuration. Fig. 1.1 shows such a modulator in an x-cut $LiNbO_3$ substrate [29]. A channel waveguide splits into two parallel waveguides through a “Y-junction” coupler, and combine together through another “Y-junction” coupler. An electric field is applied to one of the two parallel waveguides. Light is coupled into the channel waveguide and separated into

two beams with equal intensities. Without an applied voltage, there is no phase shift between the two beams and constructive interference occurs at the output of the modulator, leading to maximum output intensity. When a voltage is applied, a phase shift between two optical paths is introduced due to the Pockels effect, and the two optical beams interfere destructively at the output of

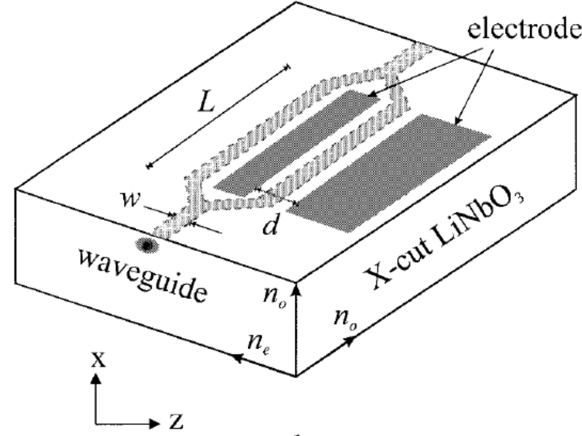

Figure 1.1: Configuration of a MZI modulator in x-cut $LiNbO_3$ [29].

the modulator.

When the phase difference between the two beams is π, a complete destructive interference occurs and gives zero output. The applied voltage needed to obtain a π phase difference is called the driving voltage (V_π). By using the equations (1-4), (1-5) and (1-6), V_π can be expressed as:

$$V_\pi = \frac{\lambda d}{n^3 r L \Gamma} \qquad (1-7)$$

where λ is the wavelength of incident light, d is the gap between the two electrodes, n is the refractive index of $LiNbO_3$, r is the EO coefficient, L is the length of the electrodes (also called "interaction length"), and Γ is the overlap factor between the optical field and the electric field.

The driving voltage of a commercial modulator is usually over 5 V, which is not desirable for high speed modulation. Therefore, reduction of the

driving voltage is an extremely important issue. It can be seen from equation (1-7) that in order to reduce the driving voltage, one possible method is to increase the length of the electrodes. However, a long interaction length leads to a large propagation loss and a large device size. In addition, the length of a conventional modulator is usually on the centimeter scale, which is too large to be embedded with other components. Another possible method of reducing the driving voltage is to increase the overlap between the applied electric field and the optical field. Chang *et al.* showed that the calculated overlap integral factor increased from 0.62 to 0.7 as the height of ridges increased from 0 to 2 μm [29]. Hence the use of ridge waveguides is a promising technique for future low drive voltage modulators.

A great deal of effort has been made to fabricate ridge waveguides. However, due to the well-known etching resistance of $LiNbO_3$, most efforts failed to obtain ridge waveguides with smooth surfaces and sidewalls, which are key factors to reduce propagation loss. In addition, low etch rate remains a significant limitation of the fabrication of deep ridges. Fig. 1.2 shows an example of etched ridge waveguides in $LiNbO_3$ [30]. It can be seen clearly that a rough surface and insufficient etch depth are present, which would lower the performance of the modulators. Therefore, etching techniques should be improved. To obtain a deeply etch structure with smooth surfaces and sidewalls is one of the main focuses of this work, which will be described in Chapter 2.

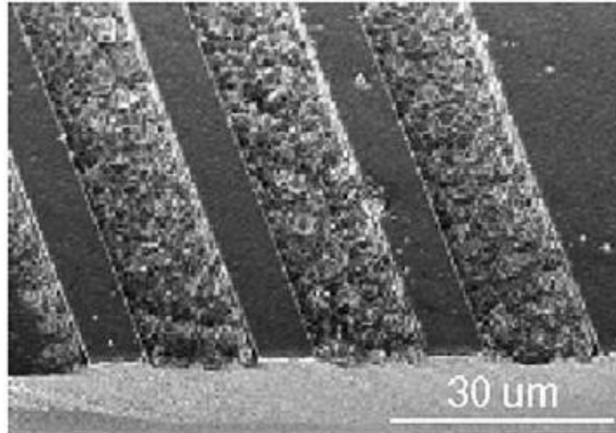

Figure 1.2: An example of etched ridge $LiNbO_3$ waveguides [30].

Apart from etching, some attempts have been made to apply other fabrication techniques to the creation of waveguides and complex structures. Ion implantation, which is widely used in the semiconductor industry, is a promising tool to fabricate novel devices in $LiNbO_3$. The mechanisms of ion implantation used to modify $LiNbO_3$ crystals are mainly based on two effects: the change of refractive index and lattice damage. The effect of refractive index change can be used to form a low refractive index optical barrier beneath the surface, leading to a form of planar waveguide. With the aid of photolithography, channel waveguides can also be fabricated, as shown in Fig. 1.3 [31].

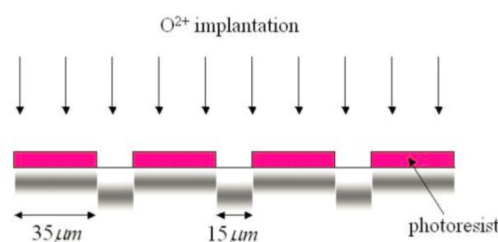

Figure 1.3: Schematic illustration of the $LiNbO_3$ channel waveguides formation using O^{2+} implantation [31].

Another effect, lattice damage caused by implantation with a high dose concentration (~ 10^{16} ions/cm^2), can be used to create a buried sacrificial layer. With subsequent lift-off, $LiNbO_3$ thin films with thickness on the micron scale can be fabricated. Such thin films are usually bonded with other substrates like SiO_2 and the adhesive polymer benzocyclobutene (BCB) to form hybrid structures. The ion-slide $LiNbO_3$ thin film has received considerable attention recently. Fig. 1.4 shows an example of a $LiNbO_3$ thin film bonded on a BCB layer, which is coated on a $LiNbO_3$ substrate [32].

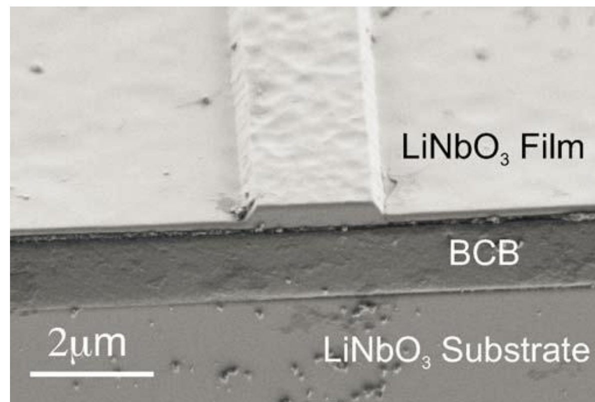

Figure 1.4: An ion sliced $LiNbO_3$ thin film bonded on a BCB layer [32].

However, it should be noted that such an ion sliced $LiNbO_3$ thin film failed to maintain the original EO properties of the bulk $LiNbO_3$. In addition, the index contrast between the thin film and substrate was still limited, leading to a weak confinement of the optical mode. In this study we aim to develop a monolithic approach to fabricate free-standing structures in bulk $LiNbO_3$, which would achieve a maximum index contrast between $LiNbO_3$ and surrounding air. A more detailed review of previous studies on ion implantation methods and our monolithic approach will be discussed in Chapter 3.

PhCs also represent a promising candidate to achieve PICs due to the

compact size and unique properties like the PBG. Only recently has it been demonstrated that PhCs can be fabricated in a $LiNbO_3$ substrate. However, it is still a challenging task to study PhCs in $LiNbO_3$. For example, so far, focused ion beam (FIB) milling is the main method to etch holes in $LiNbO_3$, but the conical shape of etched holes decreases the coupling between the optical mode and the PhC. Our goal is to realize PhCs in both free-standing slabs and channel waveguides and to study their optical properties, which will be presented in Chapters 4 and 5.

1.3 Research objectives

Despite the growing awareness of the importance of novel $LiNbO_3$ devices and PICs, there is still insufficient knowledge to solve problems associated with fabrication methodologies of bulk $LiNbO_3$ substrates. The overall objective of this thesis is to explore different fabrication methods and to develop novel devices which would be used as key components in next generation communications systems and $LiNbO_3$ PICs. The specific aims are the following:

- To investigate the dry etching properties of bulk $LiNbO_3$ systematically by using inductively coupled plasma (ICP) in order to obtain deep anisotropic structures in $LiNbO_3$ with smooth surface and vertical sidewalls, which are very important for achieving advanced compact devices on bulk $LiNbO_3$ substrate.
- To develop a monolithic method for suspended $LiNbO_3$ structure fabrication by using ion implantation and selectively wet etching.
- To fabricate PhCs in both suspended slabs and channel waveguides by using FIB milling.

- To study both out-of-plane and in-plane properties of PhCs in $LiNbO_3$ theoretically and experimentally in order to explore the potential of PhCs in further free-space and fiber-optical devices.

The realization of deep anisotropic ridge structures should overcome the fabrication difficulties of current $LiNbO_3$ modulators, while the realization of suspended structures should open up new avenues for the fabrication of compact and low loss PICs in bulk $LiNbO_3$. The incorporation of PhC into suspended slabs should exhibit some interesting features, while the incorporation of PhC into channel waveguide should provide new strategies for decreasing interaction length of $LiNbO_3$ modulators. It should be noted that the process of fabricating a modulator with ridge structures is very complicated and involves many engineering issues, but these are not central to this thesis and hence are beyond the scope of this thesis.

1.4 Outline of thesis

The remaining chapters of this thesis are organized as follows:

Chapter 2 investigates dry etching properties of $LiNbO_3$ by using ICP. A new technique, gas cluster ion beam (GCIB), is firstly employed to smooth the sidewalls of etched ridge structures in $LiNbO_3$ and the preliminary results are presented.

Chapter 3 presents the fabrication techniques of suspended $LiNbO_3$ structures by the combination of multiple-energy ion implantation and wet etching. Ion implantation technique used in $LiNbO_3$ membrane is reviewed. The influence of implantation parameters and some fabrication difficulties are discussed. Some important components with suspended structure such as microdisk and microwires are presented.

Chapter 4 proposes a free-standing monolithic $LiNbO_3$ PhC slabs. Their Fano resonance phenomena are systematically investigated for the first time. Both simulation and experimental characterizations are performed and the effects of structure dimensions are discussed.

Chapter 5 demonstrates an exploratory study on in-plane transmission properties of photonic crystals in annealed proton exchange (APE) $LiNbO_3$ waveguides. Background information on APE technique is introduced. Fabrication procedures of PhC using FIB are presented in detail.

Chapter 6 concludes the thesis and provides recommendations for future work.

References for the thesis are included at the end of each chapter.

References

[1] L. Arizmendi, "Photonic applications of lithium niobate crystals," Physica Status Solidi (a) **201**, 253-283 (2004).

[2] E. L. Wooten, K. M. Kissa, A. Yi-Yan, E. J. Murphy, D. A. Lafaw, P. F. Hallemeier, D. Maack, D. V. Attanasio, D. J. Fritz, G. J. McBrien, and D. E. Bossi, "A review of lithium niobate modulators for fiber-optic communications systems," IEEE Journal of Selected Topics in Quantum Electronics **6**, 69-82 (2000).

[3] R. Brinkmann, I. Baumann, M. Dinand, W. Sohler, and H. Suche, "Erbium-doped single- and double-pass Ti:$LiNbO_3$ waveguide amplifiers," IEEE Journal of Quantum Electronics **30**, 2356-2360 (1994).

[4] E. Dogheche, V. Sadaune, X. Lansiaux, D. Remiens, and T. Gryba, "Thick $LiNbO_3$ layers on diamond-coated silicon for surface acoustic wave filters," Applied Physics Letters **81**, 1329-1331 (2002).

[5] E. L. Wooten, R. L. Stone, E. W. Miles, and E. M. Bradley, “Rapidly tunable narrowband wavelength filter using $LiNbO_3$ unbalanced Mach-Zehnder interferometers,” Journal of Lightwave Technology **14**, 2530–2536 (1996).

[6] G.-W. Lu, S. Shinada, H. Furukawa, N. Wada, T. Miyazaki, and H. Ito, “160-Gb/s all-optical phase-transparent wavelength conversion through cascaded SFG-DFG in a broadband linear-chirped PPLN waveguide,” Optics Express **18**, 6064–6070 (2010).

[7] R. Schiek, Y. Baek, G. Krijnen, G. I. Stegeman, I. Baumann, and W. Sohler, “All-optical switching in lithium niobate directional couplers with cascaded nonlinearity,” Optics Letters **21**, 940–942 (1996).

[8] G. A. Magel, M. M. Fejer, and R. L. Byer, "Quasi-phase-matched second-harmonic generation of blue light in periodically poled $LiNbO_3$," Applied Physics Letters **56**, 108-110 (1990).

[9] K. Noguchi, H. Miyazawa, and O. Mitomi, "Frequency-dependent propagation characteristics of coplanar waveguide electrode on 100 GHz Ti:$LiNbO_3$ optical modulator," Electronics Letters **34**, 661-663 (1998).

[10] A. Loni, G. Hay, R. M. De La Rue, and J. M. Winfield, "Proton-exchanged $LiNbO_3$ waveguides: the effects of post-exchange annealing and buffered melts as determined by infrared spectroscopy, optical waveguide measurements, and hydrogen isotopic exchange reactions," Journal of Lightwave Technology **7**, 911-919 (1989).

[11] F. Lu, G. Fu, C. Jia, K. Wang, H. Ma, and D. Shen, "Lithium niobate channel waveguide at optical communication wavelength formed by multienergy implantation," Optics Express **13**, 9143-9148 (2005).

[12] S. Fouchet, A. Carenco, C. Daguet, R. Guglielmi, and L. Riviere,

"Wavelength dispersion of Ti induced refractive index change in $LiNbO_3$ as a function of diffusion parameters," Journal of Lightwave Technology **5**, 700-708 (1987).

[13] M. M. Howerton, R. P. Moeller, A. S. Greenblatt, and R. Krahenbuhl, "Fully packaged, broad-band $LiNbO_3$ modulator with low drive voltage," Photonics Technology Letters **12**, 792-794 (2000).

[14] W. K. Burns, M. M. Howerton, R. P. Moeller, R. Krahenbuhl, R. W. McElhanon, and A. S. Greenblatt, "Low drive voltage, broad-band $LiNbO_3$ modulators with and without etched ridges," Journal of Lightwave Technology **17**, 2551-2555 (1999).

[15] W. J. Park, W. S. Yang, W. K. Kim, H. Y. Lee, J. W. Lim, M. Isshiki, and D. H. Yoon, "Ridge structure etching of $LiNbO_3$ crystal for optical waveguide applications," Optical Materials **28**, 216-220 (2006).

[16] T. Baba, "Slow light in photonic crystals," Nature Photonics **2**, 465-473 (2008).

[17] M. Solja, S. G. Johnson, S. Fan, M. Ibanescu, E. Ippen, and J. D. Joannopoulos, "Photonic-crystal slow-light enhancement of nonlinear phase sensitivity," Journal of the Optical Society of America B **19**, 2052-2059 (2002).

[18] J. U. Fürst, D. V. Strekalov, D. Elser, A. Aiello, U. L. Andersen, C. Marquardt, and G. Leuchs, "Quantum light from a whispering-gallery-mode disk resonator," Physical Review Letters **106**, 113901 (2011).

[19] L. Ding, C. Baker, P. Senellart, A. Lemaitre, S. Ducci, G. Leo, and I. Favero, "High frequency GaAs nano-optomechanical disk resonator," Physical Review Letters **105**, 263903 (2010).

[20] E. Homeyer, J. Houel, X. Checoury, G. Fishman, S. Sauvage, P. Boucaud, S. Guilet, R. Braive, A. Miard, A. Lemaître, and I. Sagnes, "Thermal emission of midinfrared GaAs photonic crystals," Physical Review B **78**, 165305 (2008).

[21] L. Zhou and A. W. Poon, "Silicon electro-optic modulators using p-i-n diodes embedded 10-micron-diameter microdisk resonators," Optics Express **14**, 6851-6857 (2006).

[22] L. Dang Hoang, H. In-Kag, and R. Sang-Wan, "Design Optimization of Photonic crystal structure for improved light extraction of GaN LED," IEEE Journal of Selected Topics in Quantum Electronics **15**, 1257-1263 (2009).

[23] S. J. McNab, N. Moll, and Y. A. Vlasov, "Ultra-low loss photonic integrated circuit with membrane-type photonic crystal waveguides," Optics Express **11**, 2927-2939 (2003).

[24] B. T. Matthias and J. P. Remeika, "Ferroelectricity in the Ilmenite Structure," Physical Review **76**, 1886-1887 (1949).

[25] G. E. Peterson and S. R. Lunt, "Refractive index measurements of lithium niobate integrated optical substrates by total internal reflection," Ferroelectrics **75**, 99-108 (1987).

[26] K. Nassau, H. J. Levinstein, and G. M. Loiacono, "Ferroelectric lithium niobate. 1. Growth, domain structure, dislocations and etching," Journal of Physics and Chemistry of Solids **27**, 983-988 (1966).

[27] A. Yariv and P. Yeh, "Optical wave crystals," John Wiley & Sons, New York (1983).

[28] A. Mendez, A. Garcia-Cabanes, E. Dieguez, and J. M. Cabrera, "Wavelength dependence of electro-optic coefficients in congruent and

quasistoichiometric $LiNbO_3$," Electronics Letters **35**, 498-499 (1999).

[29] S. J. Chang, C. L. Tsai, Y. B. Lin, J. F. Liu, and W. S. Wang, "Improved electrooptic modulator with ridge structure in x-cut $LiNbO_3$," Journal of Lightwave Technology **17**, 843-847 (1999).

[30] W. S. Yang, H. Y. Lee, W. K. Kim, and D. H. Yoon, "Asymmetry ridge structure fabrication and reactive ion etching of $LiNbO_3$," Optical Materials **27**, 1642-1646 (2005).

[31] F. Lu, G. Fu, C. Jia, K. Wang, H. Ma, and D. Shen, "Lithium niobate channel waveguide at optical communication wavelength formed by multienergy implantation," Optics Express **13**, 9143-9148 (2005).

[32] G. Poberaj, M. Koechlin, F. Sulser, A. Guarino, J. Hajfler, and P. Gunter, "Ion-sliced lithium niobate thin films for active photonic devices," Optical Materials **31**, 1054-1058 (2009).

Chapter 2 Characterization of ICP etched $LiNbO_3$

2.1 Introduction

Etching plays an important role in the quest to realize ultra-small PICs. However, compared with many traditional semiconductor materials like Si, GaAs, etc., $LiNbO_3$ is known as a difficult material to etch. This difficulty strongly hinders the use of $LiNbO_3$ in modern photonic devices. Consequently the development of appropriate etching recipes becomes a necessity.

2.1.1 Plasma etching methodology

There are two main methods for etching: wet etching and dry etching. Wet etching is the immersion of wafers into baths containing liquid chemicals or etchants, and was typically used in the early days of semiconductor fabrication. Wet etching, based on a mixture of HF and HNO_3, is a simple process for etching $LiNbO_3$ according to the following reaction:

$$LiNbO_3 + 9HF \rightarrow LiHF_2 + H_2NbF_7 + 3H_2O \qquad (2-1)$$

This method can provide a reasonable selectivity. In recent decades wet etching, combined with a variety of methods, including PE [1], ion implantation [2], metal deposition [3], and domain inversion [4] have been reported for fabricating ridge $LiNbO_3$ waveguides. However, wet etching is a time consuming process due to its low etching rate. The poor anisotropic property of wet etching is also a drawback. In a recent work Hu *et al.* reported a modified method to etch $LiNbO_3$ by a mixture of HF and HNO_3 for ridge waveguide formation [5]. Hu's contribution is the addition of ethanol into the mixture,

which produces a smoothly etched surface. However, the reported etching rate was only 10 nm/min. Furthermore, the proposed wet etching method only can be applied to z-cut $LiNbO_3$ because of the relative high etching rate along the z axis of the crystals. For x-cut or y-cut samples the etching rate along the x or y axe was respectively very low. In Hu's work, the reported etching rate of an x-cut sample was lower than 3 nm/hour.

Most wet etching processes used in the past are no longer utilized for high quality industrial fabrication, and have been replaced by dry etching. Dry etching has many advantages over wet etching because it is highly controllable and highly anisotropic. Thus, dry etching is widely used in general microfabrication applications. Several dry etching techniques have been reported for etching $LiNbO_3$, such as direct laser writing [6], FIB milling [7], neutral loop discharge plasma (NLD) [8], and reactive ion etching (RIE) [9, 10]. Among these dry etching techniques, plasma etching has drawn much attention due to many advantages. The first advantage is that reactive chemical species can be produced in a plasma which can etch more vigorously than species in a non-plasma environment. This significantly enhances the etching rate. Secondly, owing to the applied electric fields normal to the sample surface, strongly anisotropic etching is possible in plasma etching. This avoids under-cutting and etch bias which are typically seen in wet etching. Anisotropic etching is a consequence of avoiding the under cutting and etch bias.

The two major mechanisms in plasma etching are chemical etching and physical sputtering. Chemical etching is caused by reactive neutral species in the plasma. These free radicals have incomplete bonding so that they are highly reactive. They will react with the samples quickly to achieve a bonded state with the material to be etched. The volatile byproducts evaporate easily into the

gas phase, allowing further reaction between samples and free radicals. The second mechanism, physical sputtering, arises due to the high voltage difference between the plasma and the electrode. This potential difference causes ions in the plasma to accelerate towards and bombard the wafer surface. Compared with chemical etching which is isotropic, this physical component is an anisotropic process due to the directionality of the electric field. However, physical etching loses selectivity owing to sputtering being a purely physical reaction.

A more anisotropic etching can be obtained by lowering the gas pressure. A low gas pressure reduces ion collisions during the etching process, thereby creating more ion flux normal to the surface of the wafer. Moreover, lower gas pressure also leads to higher sheath voltage and ion energy. However, standard plasma etching systems such as RIE typically uses only one RF system to control both the plasma density and ion energy, and as a result they are closely coupled. This means that lower pressure leads to fewer gas atoms and therefore reduced plasma density. As a result, a gas pressure of 10 to 100 mTorr is typically used in RIE systems.

Recently, ICP etching has drawn increased attention because of the greater control possible over the resultant etch profile relative to other methods. There are two RF sources in a typical ICP system. One RF source is used to generate a high density plasma. Another RF source is used to generate a bias voltage on the sample holder, which controls the acceleration energy of ions toward the sample surface. Therefore, the plasma density and the ion energy are controlled independently, which means both high etching rate and high anisotropy can be achieved in an ICP system.

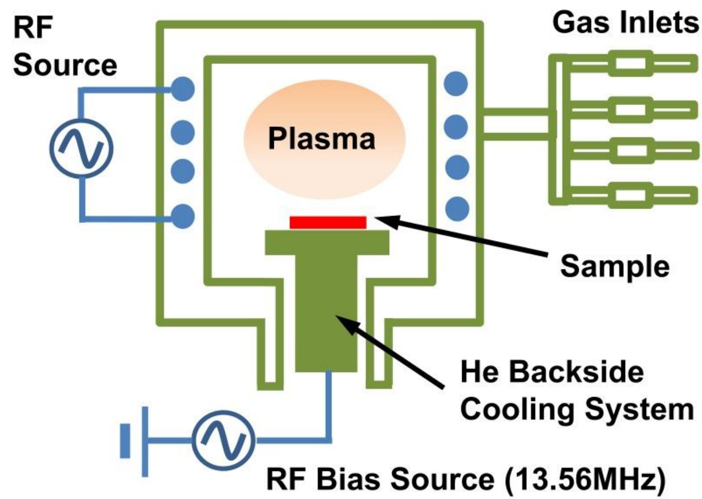

Figure 2.1: Schematic diagram of the ICP system used in this work.

The ICP system used in our work is a Plasma-Therm SLR model 770 with a load lock, as shown in Fig. 2.1. The plasma is formed by ionized gases and contains electrons, free radicals and reactive ions. In an ICP system, the plasma is excited by RF power coupled to an inductive circuit element. A mass flow controller is used to control gas flow. A dielectric vessel encircled by an inductive coil is used to generate high density plasma. Another RF bias is superimposed at the substrate to control ion energy with a frequency of 13.56 MHz. A helium (He) gas cooling system is installed in the chuck through an engraved groove to control the temperature of the wafer. A small amount of He gas is employed between wafer and chuck. This creates a thin cushion of He and heat is transferred uniformly from wafer to chuck. In all our etching work, the initial substrate temperature is set at room temperature (20°C). Before etching, a cleaning process of oxygen plasma is applied to clean the chamber and remove any residual impurity.

2.1.2 Literature review of $LiNbO_3$ etching

Recently some efforts based on ICP using SF_6, CF_4, and CHF_3 plasmas have

been devoted to the dry etching of $LiNbO_3$. In 2006 Hu *et al.* used ICP to etch bulk $LiNbO_3$ for the first time [11]. They demonstrated a method that avoided redeposition of LiF, a main bottleneck in the development of dry etching techniques for $LiNbO_3$, by preliminarily using a PE process. An etched ridge of 1.5 μm was fabricated but a rough surface condition was obvious after the etch. Following this breakthrough, Ren *et al.* studied the etching conditions on PE $LiNbO_3$ in 2008 [12]. With optimized parameters, a ridge waveguide with thickness of 1.2 μm was fabricated. Subsequently, Ulliac *et al.* reported nanometric rods fabricated in $LiNbO_3$ by ICP etching [13]. By properly choosing the dry etching conditions, a smoothly etched surface was obtained. However, these etches cannot produce perfectly vertical sidewalls; instead sidewalls with etched angles less than 85° are produced. Ulliac *et al.* also reported poor mask selectivity during the etching process. In a more recent work, an array of holes at a submicron pitch with a depth of 60 to 80 nm was etched by ICP using CHF_3 [14]. This result indicated that ICP etching is possible for the production of densely integrated $LiNbO_3$ devices. However, only holes at larger diameters and shallower depths were achieved with a very low etching rate. Longer etching periods introduced rougher surfaces and significant distortion with only a 400 nm depth.

Table 2.1 summarizes and compares recent results on the dry etching of $LiNbO_3$. Most of the dry etching work has been done by ICP, and different gas compositions were used. However, because of the lack of a suitable mask, it is challenging for plasma etching to produce a smooth surface, which is important to mitigate optical loss in resultant waveguides. The deterioration of the surface after etching is caused by different mechanisms, like physical sputtering of the mask during etching and redeposition of LiF and NbFx. In addition, there are

only a few extant studies on profile control of $LiNbO_3$ etching. From Table 2.1 it can be seen that after etching the sidewall angles in most studies are lower than 85°, resulting in trapezoidal ridges. Ridges with vertical sidewalls are necessary to obtain a better control of optical modes and an improvement of electric\optical fields overlap.

Table 2.1: Summary of recent work on dry etching of $LiNbO_3$.

Reference	Etching Methodology	Etching Gas	Etching Rate	Etching Depth	Sidewall Angle
[8]	Neutral Loop Discharge Plasma (NLD)	C_3F_8 /Ar	150 nm/min	1.5 μm	70°
[10]	Reactive Ion Etching(RIE)	—	50 nm/min	10 μm	73°
[11]	Inductively Coupled Plasma(ICP)	CHF_3 /Ar	95 nm/min	1.5 μm	—
[13]	Inductively Coupled Plasma(ICP)	CF_4/He	280 nm/min	400 nm	75°
[12]	Inductively Coupled Plasma(ICP)	SF_6/Ar	190 nm/min	1.1 μm	85°
[15]	Inductively Coupled Plasma(ICP)	C_4F_8//He	—	3 μm (repeat 10 times)	—

Moreover, in Table 2.1, only shallow etched structures with a depth of less than 2 μm were obtained, and this is generally true of all dry etching studies in $LiNbO_3$. Compared with shallow waveguides, deep waveguides can provide better optical confinement, so this is our goal. Deep ridge waveguides have lower loss and can be bent sharply (due to the greater index contrast) to reduce component size. Therefore, deep, vertical etching is a key strategy for realizing future compact integrated devices. The etching profile of a waveguide must be considered and carefully controlled during deep etching processes. Vertical sidewalls and rectangular structures allow fabrication of waveguides

with better mode profiles and reduced insertion loss, which are especially important in multimode interference and MZI [16]. The ability to realize low-loss rectangular waveguide structures would lead to improved performance of MZI modulators, by enabling the use of PhCs, ring resonators, etc., which require a high index contrast not achievable with traditional $LiNbO_3$ waveguide fabrication processes. In this chapter, we focus on $LiNbO_3$ etching, but it is also worth pointing out that high index contrast vertical confinement is also often desirable for low-loss optical waveguiding, and that monolithic techniques do exist to create slabs of $LiNbO_3$. Although in this study we etched bulk $LiNbO_3$, the ICP methods under investigation could also apply for such slabs.

In this study, we also use the PE technique to reduce the concentration of Li ions in the $LiNbO_3$ surface, leading to less redeposition of LiF and an improved etching rate. Because $LiNbO_3$ is a difficult material to etch, there have been no prior reports of deeply-etched anisotropic structures (> 2 μm) realized in a single etch step. L. Gui *et al.* [15] recently reported a relatively deep etch (3 μm depth) using ICP with a C_4F_8 and He gas mixture. Their process was lengthy (> 40 minutes) and samples needed to be taken out and cleaned in SC-1 (RCA) solution to remove a brown layer. After etching the surface of $LiNbO_3$ substrate was very rough, so a post annealing process was required to smooth the surface. The main reason why it is hard to realize deep structures in $LiNbO_3$ is the formation of LiF during the etching process [17]. LiF has a high boiling point of 1676 ℃. In addition, metal particles sputtered by ion bombardment and other fluoride based inhibitors that get deposited on the $LiNbO_3$ surface during etching serve to prevent further etching after a given time. For deep structure etching, the redeposition of such inhibitors is a critical issue to overcome. As etching time increases, inhibitors will

accumulate on the surface and sidewalls causing the etching rate to decrease significantly. Consequently, careful control over the etching conditions is very important for lengthy etching processes. In addition, the deposition of a thick metal mask is also a critical issue. The mask needs to be thick enough to prevent strong physical sputtering, which is necessary to remove the residue.

2.1.3 Motivation

Based on the above review, it is clear that there is much work that needs to be done due to many difficulties involved during etching. In this chapter, we performed systematic investigations on the etching of $LiNbO_3$ and focused our efforts on achieving deep ridges with vertical profiles, smooth surfaces and sidewalls. Our studies were divided into three steps:

Firstly, in order to find a suitable mask and gas mixtures for smooth-surface etching, a dry etching processes using different metal masks and gases was investigated. Three metallic masks, silver (Ag), nickel (Ni), chromium (Cr) and three gas mixtures, CHF_3/Ar, SF_6/Ar, CF_4/Ar were used. These will be described in Section 2.3.

Secondly, based on the suitable mask and gas mixtures found in Section 2.3, our goal was to realize deep anisotropic ridges. To achieve this goal, the influences of He backside cooling, power, and gas flows during etching process were investigated, which will be described in Section 2.4.

Thirdly, after the realization of deep anisotropic structures, it is worthwhile to achieve smooth sidewalls of etched ridges. For this purpose, a dry polishing technique, GCIB, was employed for post etching modifications and irradiation parameters were optimized, which will be described in Section 2.5.

2.2 Fabrication procedures

As previously mentioned, the PE method can reduce the concentration of Li ions near the $LiNbO_3$ surface. This reduces the re-deposition of LiF and therefore improves the overall etching rate. During the PE process hydrogen ions will diffuse into samples, changing the wafer surface composition to a certain depth into $H_xLi_{1-x}NbO_3$. In our experiments benzoic acid was chosen because, compared to the alternatives, it is less toxic and requires a lower temperature for the proton exchange. The boiling point of benzoic acid is 250 ℃.

Our setup for the PE process is shown in Fig. 2.2. Although benzoic acid is less toxic, there is still a safety issue that must be considered. In the presence of an ignition source, vapor from molten benzoic acid may form an explosive mixture with air in sufficient concentrations, resulting in an explosion risk. Because of the low flash point of 121 ℃ for benzoic acid, a flash-proof hotplate was used. In addition, the whole process was performed in a fume hood. A hotplate adjustable temperature heats a reaction beaker that contains the benzoic acid. When the temperature exceeds 122 ℃, the liquid in the beaker starts to evaporate at a significant rate, and as a result an aluminum foil was used to cover the beaker to impede vapor leaking. With the aid of a thermocouple, the heating temperature deviation was kept to less than 1 ℃. After standard cleaning with acetone, isopropanol and de-ionized water, $LiNbO_3$ wafers were put in a Teflon container and immersed in molten benzoic acid at 235 ℃ for 5 hours. In this chapter the PE process was performed on all $LiNbO_3$ samples before ICP etching.

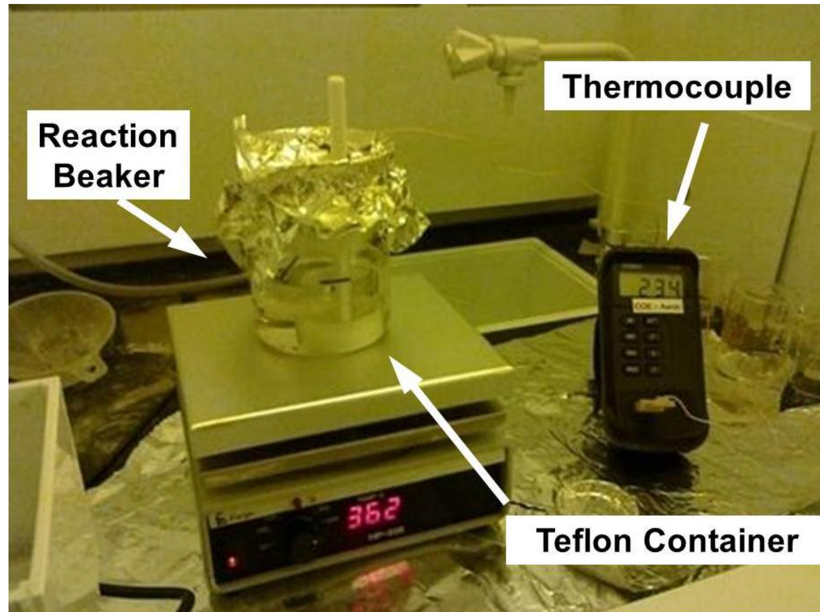

Figure 2.2: Setup of PE process.

The fabrication process is depicted schematically in Fig. 2.3. Etching studies were performed on $LiNbO_3$ wafers which were cut into 1.4 $\times$ 1 cm^2 samples. A positive photoresist (AZ5214E) was spin-coated onto the substrate. Stripes of 2-18 μm width were patterned by photolithography. Then a metallic film of thickness 150 nm was deposited on the samples by thermal evaporation (for Cr) or electron beam evaporation (for Ni and Ag). A titanium (Ti) film of 10 nm was deposited before Ag deposition to enhance the adhesion between Ag and $LiNbO_3$. Prior to the etching, we used O_2 plasma to clean the chamber of any impurities for 15 minutes with RIE power of 150 W, chamber pressure of 10 mTorr and gas flow of 20 sccm. In the subsequent etching process, Ar was added to the fluorine-based gas which can increase the physical etching component and enhance the anisotropy. After ICP etching, metallic masks were removed by wet etching. The surface condition and profile of etched ridges were characterized by scanning electron microscopy (SEM). The etching depth was measured by a surface profiler.

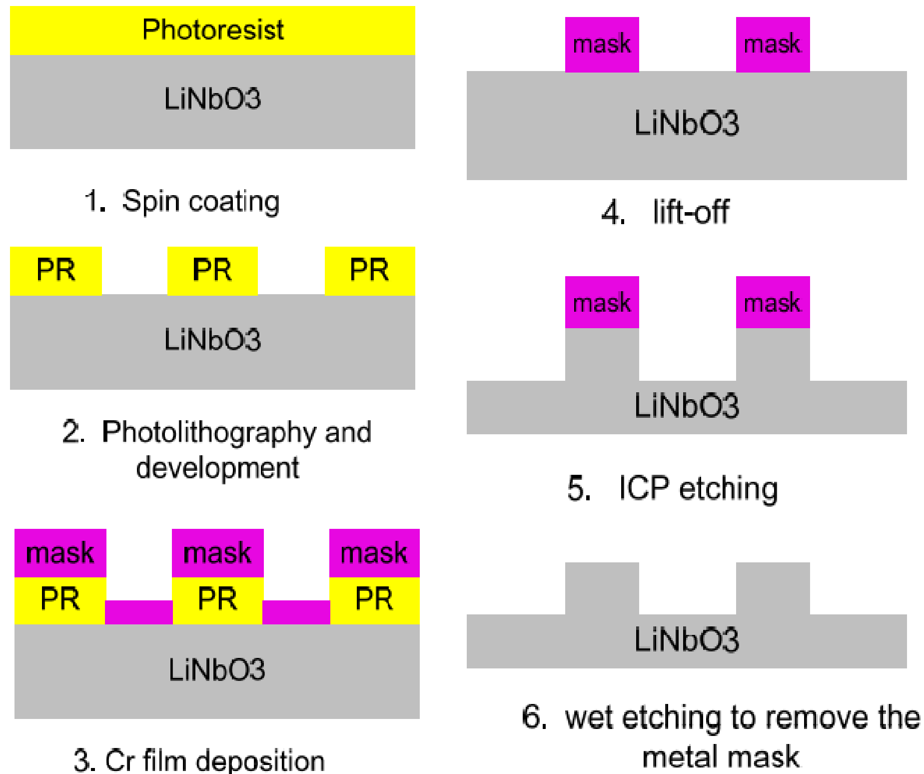

Figure 2.3: Illustration of the ridge structures fabrication process.

2.3. Etching characterization under different metallic masks and gas compositions

Figure 2.4 is a SEM image which shows the surface condition of $LiNbO_3$ after ICP etching with a 150 nm Ag mask. The etching gas is a CF_4/Ar mixture, and the etching time is 20 minutes. It seems that the metallic mask was etched strongly with $LiNbO_3$ because there is no clear depth difference between the mask and the uncovered $LiNbO_3$ substrate. After the ICP process, a Ag mask was hard to remove by strong acids such as HF or HCL+HNO_3. This is partly due to the reaction between Ag and etching gases. After etching, the composition of the metallic mask had already changed [26].

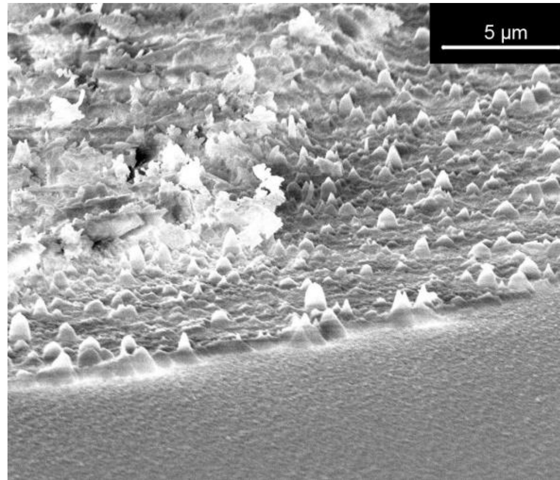

Figure 2.4: SEM image of etched $LiNbO_3$ with Ag as an etching mask. The $LiNbO_3$ substrate shows better surface condition than mask area.

A similar situation happened when a Ni mask was used in ICP etching, as shown in Figs. 2.5 (a) and (b). The gases we used were a SF_6/Ar mixture and CHF_3/Ar mixture. The surface roughness is obvious. Comparing with Ag, there is an advantage for a Ni mask in that it can be easily removed by HNO_3. Fig. 2.5 (a) shows the surface before removing the Ni mask. The surface roughness caused by physical sputtering and redeposition of the mask is clear in Fig. 2.5 (a). Fig. 2.5 (b) shows the surface after removing the Ni mask.

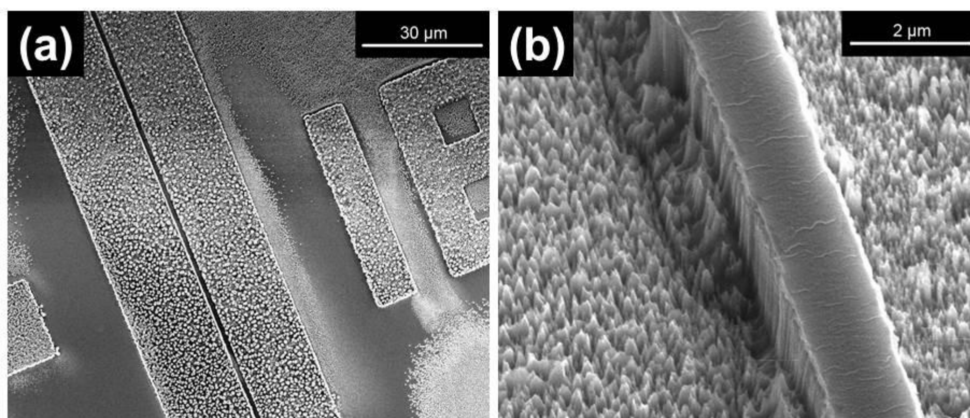

Figure 2.5: SEM images of the surface condition of etched $LiNbO_3$ with Ni as etching mask. (a) Image of etched $LiNbO_3$ using a SF_6/Ar gas mixture. The Ni mask remains on the surface; (b) Image of etched $LiNbO_3$ using a CHF_3/Ar gas mixture. (The Ni mask had already been removed by wet etching.)

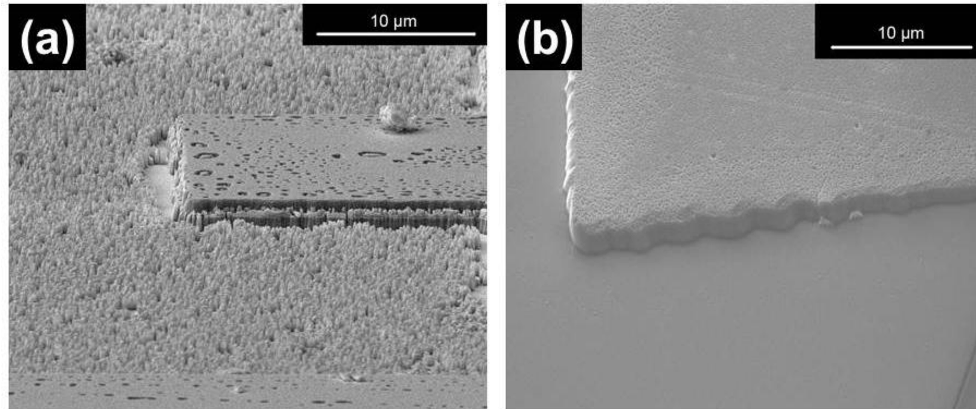

Figure 2.6: (a) SEM image of etched $LiNbO_3$ using a Cr mask and a CHF_3/Ar gas mixture. The surface is very rough; (b) SEM image of etched $LiNbO_3$ using a Cr mask and a SF_6/Ar gas mixture.

Figures 2.6 (a) and (b) show the surface of $LiNbO_3$ after the ICP and wet etching process using Cr as a metal mask. By using CHF_3/Ar as etching gases, it can be found that the surface is very rough, especially in the uncovered area. It may be due to intensive ion bombardment to the mask and physical sputter. The Cr metal sputtered from the covered area is deposited on the uncovered area and serves as an undesirable etch mask. The other important reason why CHF_3 and CF_4 cannot lead to a smooth surface is that a LiF layer is formed during etching (the structure of the LiF layer is amorphous for CHF_3 while it is crystalline for CF_4) [10]. Comparing with use of CHF_3/Ar as an etching gas, SF_6/Ar combinations lead to better surface conditions and can avoid roughness greatly, as shown in Fig. 2.6 (b). The etched area of the sample is very smooth. The Cr mask can be easily removed by commercial etchant.

Table 2.2 shows the ICP etching parameters, and the calculated etching rates and selectivities. Two masks, Cr and Ni, were used because compared with Ag alone, they can be easily removed by commercial etchant. Three different gases were studied in ICP etching processes: CHF_3, CF_4 and SF_6. Argon is a

useful inert gas for dry etching, which can be used to physically bombard the target and enhance the sputtering process. In this work, Ar was added to the three gases to enhance the etching rate and profile. A surface profiler was used to measure etching depths shown in Table 2.2.

In order to characterize the effect of different gases for ICP etching, the same etching parameters were used, gas pressure=8 mTorr, ICP power=500 W, RIE power=100 W (No. 1-4, Table 2.2). All recipes show relatively high selectivity, ranging from 8.1:1 to 16:1. The recipe using a Cr mask and CF_4/Ar mixture shows the highest selectivity, 16:1 (No.3, Table 2.2). A slightly smaller selectivity, 15.8:1, was also achieved in recipe 4 using a Ni mask and CHF_3/Ar gases mixture. It means that both Cr and Ni are efficient etching masks for $LiNbO_3$-based device fabrication.

According to Table 2.2 (No. 1-3), it can be seen that the etching rate of $LiNbO_3$ is dependent on the gas mixture. For the Cr mask, the highest etching rate, 94 nm/min, can be reached by using CHF_3/Ar gases (No. 3). In addition, comparing No. 1 and No. 4, the etching rate of $LiNbO_3$ is found to be dependent on the etch mask. An etching rate of 79 nm/min can be reached by using a Ni mask; meanwhile, the etching rate of $LiNbO_3$ is only 57 nm/min by using a Cr mask under the same conditions.

According to the comparison, we find that although CHF_3 or CF_4 can lead to higher etching rates, using a Cr mask combined with SF_6/Ar gases can lead to the best surface condition of etched $LiNbO_3$. Consequently, we fabricated ridge waveguides on $LiNbO_3$ substrate by using a Cr mask combined with a SF_6/Ar mixture. Fig. 2.7 (a) shows the top view of a ridge waveguide on $LiNbO_3$ fabricated by ICP etching using SF_6/Ar gases and a Cr mask. In order to improve the profile of the waveguide, an etching condition of Cr mask and

SF_6/Ar=1:1 was used to fabricate a ridge waveguide of approximately 600 nm depth and 5 μm width, as shown in Fig. 2.7 (b). A smooth top surface and nearly vertical sidewall were achieved.

Table 2.2: Plasma etching parameters, average etching rates and selectivities.

Sample No.	Metallic Mask	Gas Mixture (sccm)	Etching Rate (nm/min)	Selectivity ($LiNbO_3$: Cr)
1	Cr	CHF_3 : 25 Ar : 20	57	8.1:1
2	Cr	SF_6 : 25 Ar : 20	48	12:1
3	Cr	CF_4 : 25 Ar : 20	94	16:1
4	Ni	CHF_3 : 25 Ar : 20	79	15.8:1

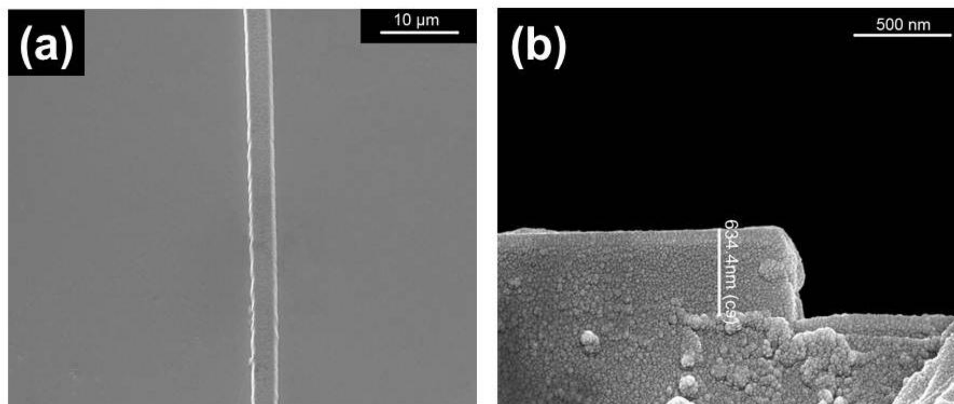

Figure 2.7: (a) Top view of fabricated ridge waveguide on $LiNbO_3$ with smooth surface; (b) SEM image showing cross section of the ridge waveguide.

2.4 Deep anisotropic etching

Based on the suitable mask (Cr) and gas mixtures (SF_6 and Ar) found in the previous section, here we investigate the influences of He backside cooling,

RIE power, and gas flows on characteristics such as etching rate, sidewall slope angle etc. in order to obtain ridge structures with large heights and vertical sidewall profiles.

2.4.1 Image reversal mode of photoresist

In our experiments, a positive photoresist AZ5412E was used for photolithography. The selectivity of Cr :$LiNbO_3$ is about 15:1, this means that 100 nm Cr film is enough if we want to only etch less than a 2 μm ridge. Thus, in order to obtain very deep ridge structures, a thick Cr film (larger than 300 nm) has to be coated before etching. However, the positive photoresist AZ5214E cannot meet the requirement of lift off process because of its sidewall profile with a positive slope of approximately 75 °- 85 °, as shown in Fig. 2.8 (c). Our experience showed that the lift-off process cannot be performed when the thickness of the Cr film exceeded 250 nm by using such a photoresist. Consequently, by taking advantage of the image reversal mode of AZ5214E, two exposure steps were used to obtain a thick Cr film with good line edge, as shown in Fig. 2.9 (a) – (e). After the first exposure, exposed areas of AZ5214E were selectively cross-linked by applying a bake cycle. A flood exposure before development was used to convert unexposed areas into materials which can be removed easily by commercial photoresist remover, resulting in a wall profile with a slope of approximately 100 ° (negative slope), as shown in Fig. 2.8 (d). The profile generated by such processing allows for use in lift-off techniques.

From Fig. 2.8 (a) we can see with normal positive mode of AZ5214E, the strip pattern cannot be removed by lift-off. The thick metal film deposited is not disjointed over the step; it overlaps the sidewall forming a continuous surface over the photoresist. With image reversal mode, AZ5214E will produce a

negative sidewall slope which prevents the metal film from being attached to the sidewall. This allows for an easy lift-off as shown in Fig. 2.8 (b). Fig. 2.9 (f) shows a cross section of photoresist of AZ5214E in image reversal mode. The thickness of the photoresist is 2.2 μm.

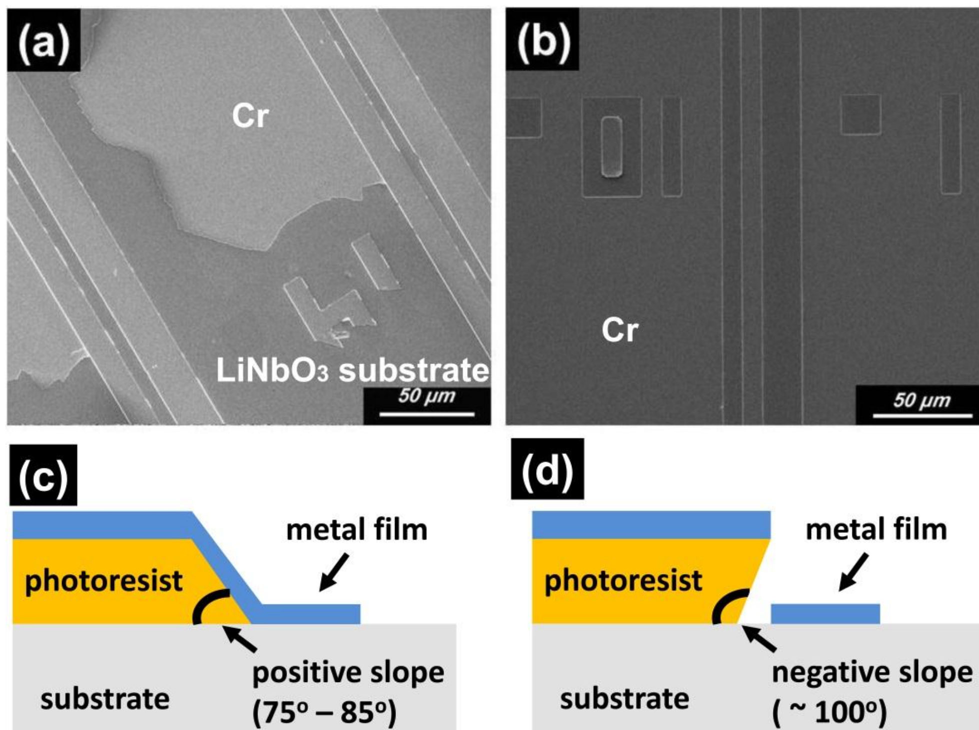

Figure 2.8: SEM images of top view of Cr patterns on $LiNbO_3$ after lift-off (a) with normal positive AZ5214E and (b) with image reverse mode of AZ5214E. Schematics of different photoresist sidewall slopes: (c) positive sidewall slope and (d) negative sidew

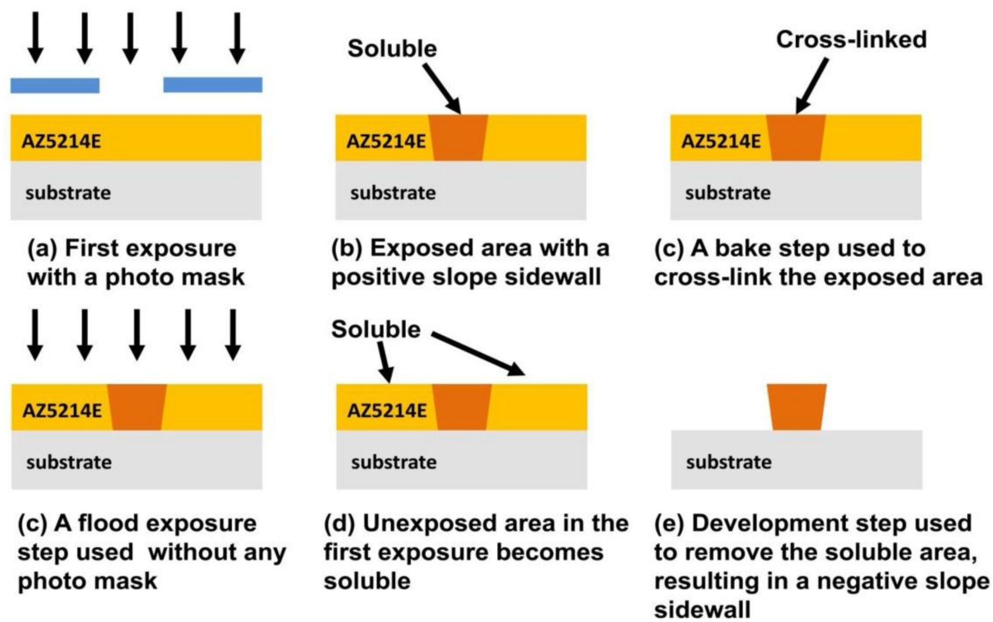

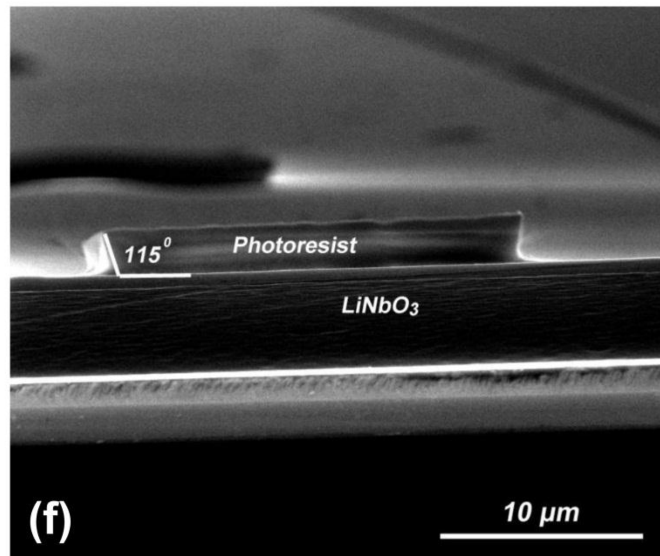

Figure 2.9: (a) – (e) Illustration of AZ5214E patterning process using image reversal mode; (f) SEM image showing a cross section of AZ5214E in image reversal mode.

2.4.2 The effect of He backside cooling

In our previous work we showed that Cr can lead to a better surface condition (post etch) and also can be easily removed using commercial Cr etchant relative to other metals. In addition, the high hardness (Mohs hardness of Cr is 8.5) among various metals helps prevent strong ion bombardment during etching and shows high selectivity. Consequently Cr was used as the etching mask.

Here, a 300 nm Cr film was deposited on the $LiNbO_3$ samples using an Edwards Auto 306 electron beam evaporator and patterned through a lift-off process. The gas composition affects the ultimate etching rate, smooth smoothness, and anisotropy significantly. As discussed in the previous section, SF_6 can lead to a smooth surface condition and the reduction of inhibitor formation. Consequently we chose SF_6/Ar as the gas mixture for these etching studies.

During a preliminary study of short etching processes, we found that the etching profile can be optimized at a 7.0 mTorr chamber pressure, 90 W RIE power and 800 W ICP power. A perfect rectangular structure with a sidewall slope angle of 90° was achieved, as shown in Fig. 2.10. The etching time was 20 minutes, and samples were etched in two steps (10 minutes each) to obtain 1.2 μm total depth. Note that on both sides of the ridge, etched microtrenching can be observed. This microtrenching is due to ions glancing off sidewalls of the ridge structure resulting in additional etching at the edges. For later long-duration single-step etching studies, we always kept the ICP power consistent at 800 W and chamber pressure at 7.0 mTorr, and other etching conditions were varied. After ICP etching, etching rates were obtained by measuring the depth of etched patterns with a surface profiler.

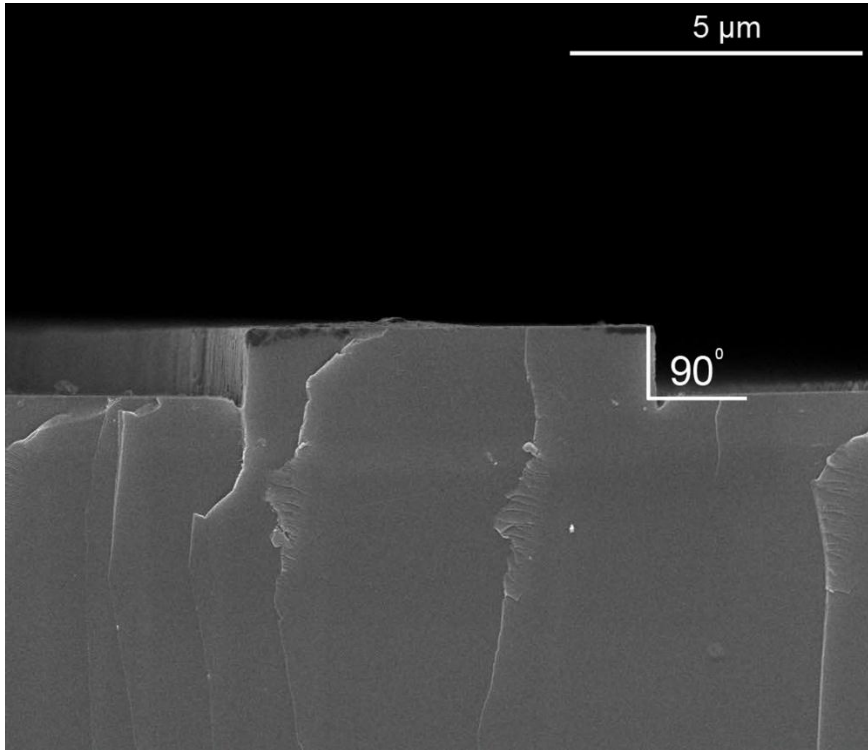

Figure 2.10: SEM cross-sectional image of a perfect rectangular etched structure with 90° slope angle at 90/800 W (RIE/ICP power), 7 mTorr pressure.

The effects of He backside cooling and two different etching modes (intermittent and continuous) were studied. The same ICP parameters were used for all samples: the ratio of SF_6 to Ar was fixed at 1:1, the ICP power was 800 W, RIE power was 90 W, chamber pressure was 7.0 mTorr and total gas flow was 10 sccm. For intermittent etching, there was a 2 minute break after every 10 minutes of etching. During the etch break, only Ar was introduced into the reactor chamber to maintain the chamber pressure, and all RF power was off. The total etching time was fixed at 30 minutes. For continuous etching, the etching process was performed continuously for 30 minutes. Continuous mode etching leads to a higher wafer surface temperature than intermittent mode, in which etching breaks allow some cooling of the wafer to occur.

A He cooling system integrated into the wafer chuck is commonly used

for wafer backside heat dissipation. Turning off the He cooling system also will lead to an increase in wafer temperature. Etching results show that the etching rate can be significantly improved by turning off the He backside cooling system and using continuous mode. The etching rate for the intermittent process increases from 47 nm/min with He cooling to 55.2 nm/min without He cooling, and the etching rate for the continuous etch process increases from 50 nm/min with He cooling to 61 nm/min without He cooling. For $LiNbO_3$ etching, the main byproducts are NbF_X, especially NbF_5. Either etching without He cooling or etching under continuous mode will cause the substrate temperature to increase significantly and help in the evaporation of NbF_5 and also assist in conversion of NbF_4 into NbF_5. Consequently, the etching rate will be increased significantly.

Figure 2.11 shows an SEM image of the surface condition (after etching) for intermittent and continuous modes. Intermittent mode etching resulted in a rough surface, as shown in Fig. 2.11 (b). In contrast, continuous etching for 30 minutes (Fig. 2.11 (a)) produced a smooth surface. The sidewall slope (nearly vertical) after continuous etching was also much more favorable than after intermittent etching.

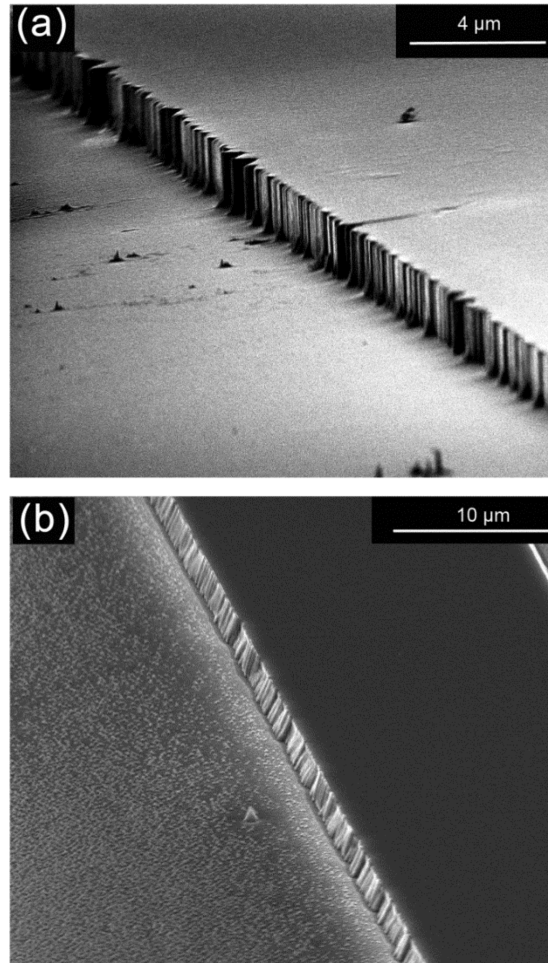

Figure 2.11: SEM images of etched $LiNbO_3$ surface condition at (a) continuous mode (b) intermittent mode.

2.4.3 The effect of RIE power

Figure 2.12 shows the measured etching rate as a function of RIE power. All other etching parameters were kept constant. The etching time is 30 minutes in continuous mode. RIE power varied from 60 W to 150 W. It can be seen that etching rate increases slightly as RIE power increases. An etching rate of 63.5 nm/min was achieved at 150 W RIE power. This can be explained by the fact that higher RIE power will cause higher DC bias voltage and higher ion energy, corresponding to strong ion bombardment and more efficient bond breaking in the $LiNbO_3$ substrate; thus increasing the etching rate.

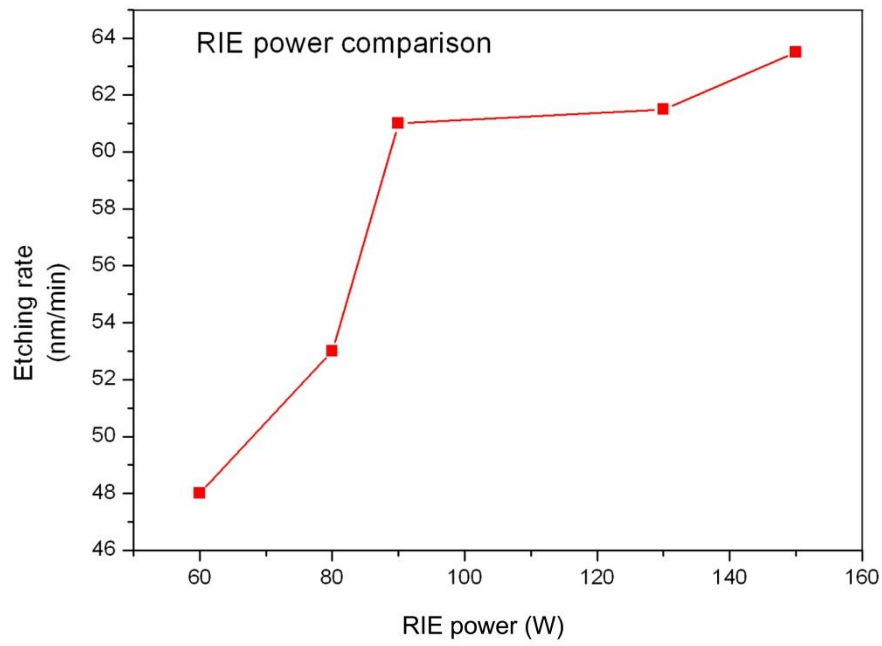

Figure 2.12: $LiNbO_3$ etching rate as a function of RIE power.

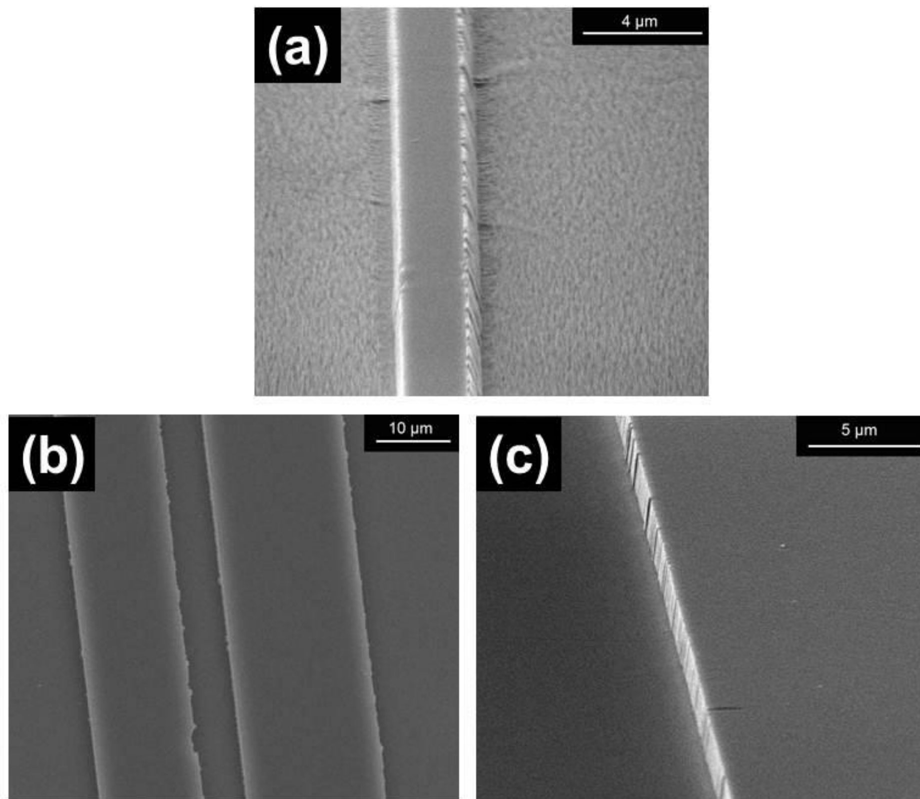

Figure 2.13: SEM images of the etched $LiNbO_3$ surface condition with different RIE power at (a) 60 W (b) 90 W (c) 150 W.

Figure 2.13 shows an SEM image of the $LiNbO_3$ surface condition after etching with different RIE powers. It can be seen that the surface conditions were less favorable at lower RIE power. This is due to insufficient ion energy (lower RIE power corresponds to lower DC bias voltage). When the RIE power is too low, weak ion bombardment cannot sputter away all inhibitors and etching residues on the surface, which then serve as micromasks, leading to a rougher surface.

Increasing the RIE power can also influence etching anisotropy, as shown in Fig. 2.14. At 60 W RIE power, an etched slope angle of 75° was obtained (Fig. 2.14 (a)), while powers of 90 W and 150 W resulted in etched slope angles of 89° and 88°, respectively (Figs. 2.14 (b) and 2.14(c)).

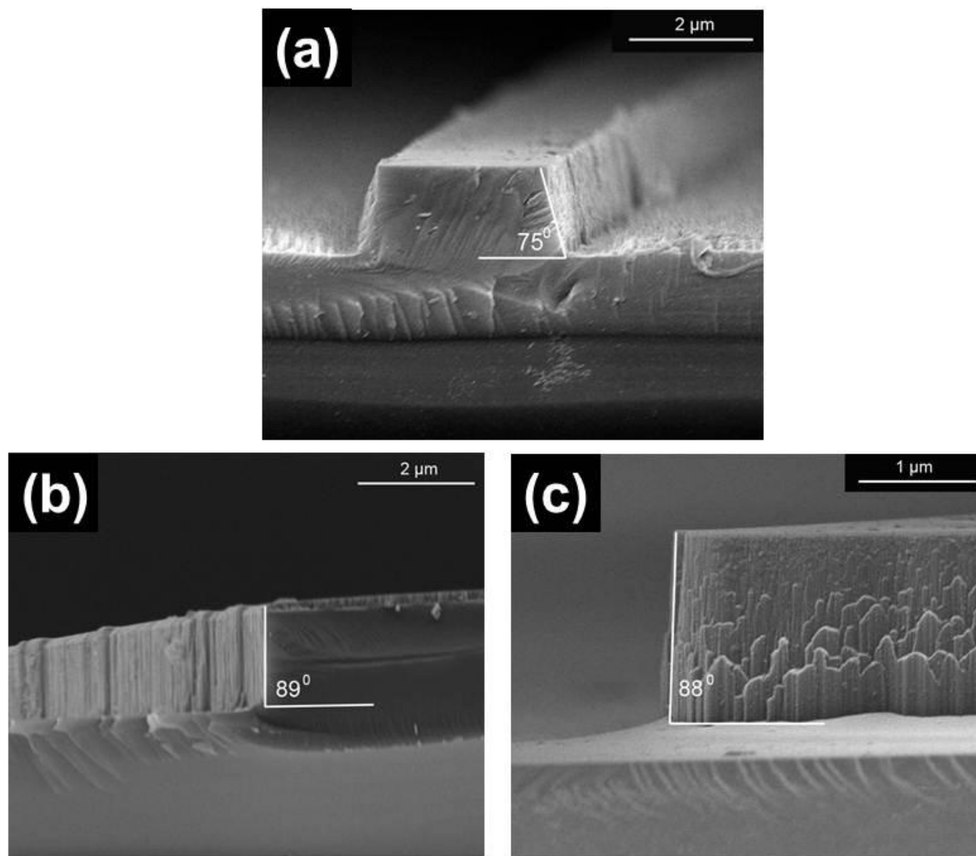

Figure 2.14: SEM images of etched $LiNbO_3$ cross section with RIE power at (a) 60 W (b) 90 W (c) 150 W. Slope angles are shown.

2.4.4 The effect of total gas flow and deep etching

Figure 2.15 presents the influence of total gas flow on the etch rate of $LiNbO_3$. The ratio of SF_6 to Ar was fixed at 1:1. It can be seen that the etching rate of $LiNbO_3$ is affected strongly by the total gas flow. There is a minimal difference in the etching rate between 10 sccm and 30 sccm. However, when gas flow was increased to 50 sccm, the etching rate improved significantly. An etching rate of 98.6 nm/min at 50 sccm gas flow was achieved for SF_6/Ar gas, which is almost double that achieved at 30 sccm gas flow, 48 nm/min. It was difficult to maintain the chamber pressure at 7.0 mTorr when a total gas flow of 100 sccm was used. During the etching process, the actual chamber pressure increased to 8.5 mTorr. It seems the etching rate decreased slightly when 50/50 sccm (SF_6/Ar) gas flow was used.

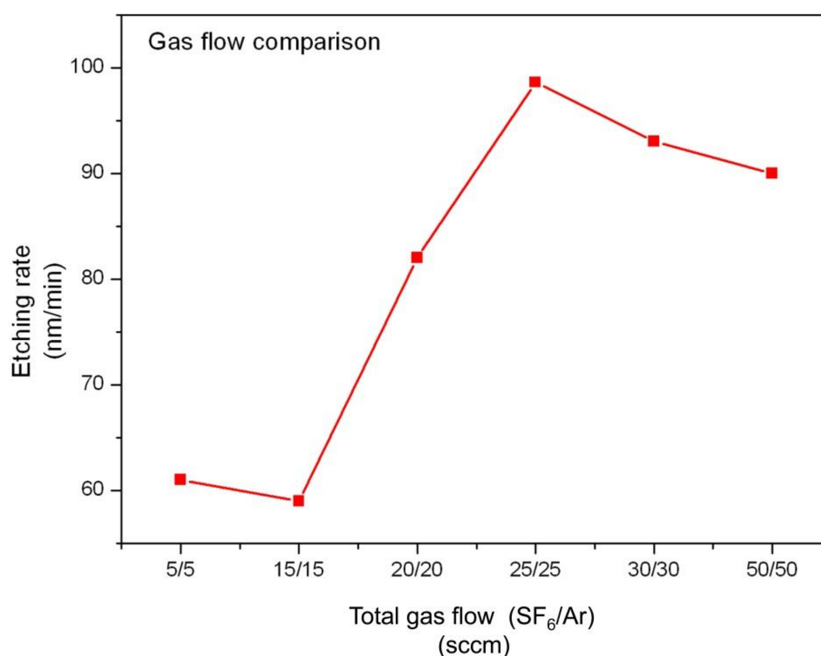

Figure 2.15: $LiNbO_3$ etching rate as a function of total gas flow. The ratio of SF_6 and Ar is fixed at 1:1.

Figure 2.16 shows the cross section of etched $LiNbO_3$ strips at different total gas flow rates. It can be seen that the total gas flow influences the etching anisotropy significantly. The etch structure with the highest slope angle (~ 90°) was obtained at a total gas flow of 10 sccm (Fig. 2.16 (a)). As the total gas flow increased, the slope angle decreased to 51° (Fig. 2.16 (c)). The inhibitor mechanism can explain the influence of gas flow on etching anisotropy. During etching, the fluorine reacts with $LiNbO_3$ and forms a nonvolatile inhibitor like LiF. With an increase of the gas flow, the formation of this inhibitor is enhanced. During lengthy etching processes, more and more inhibitor is deposited on the sidewall, impeding further etching there, while the inhibitor deposited on the bottom is removed by ion bombardment. Consequently, the sidewall slope angle decreases as gas flow increases. This phenomenon is much more significant in long-duration etching. In addition, notice that the surface of the $LiNbO_3$ substrate becomes rough at 30/30 sccm SF_6/Ar gas flow (Fig. 2.16 (c)), while a smooth surface was obtained at lower gas flow (Figs. 2.16 (a) and 2.16 (b)). The rough surface is also mainly due to the enhancement of the inhibitor. With an increase of the gas flow, the redeposition of the inhibitor (especially LiF) is enhanced greatly. The speed of redeposition of LiF is faster than the speed of physical sputtering. This indicates that the ion bombardment cannot remove all residues.

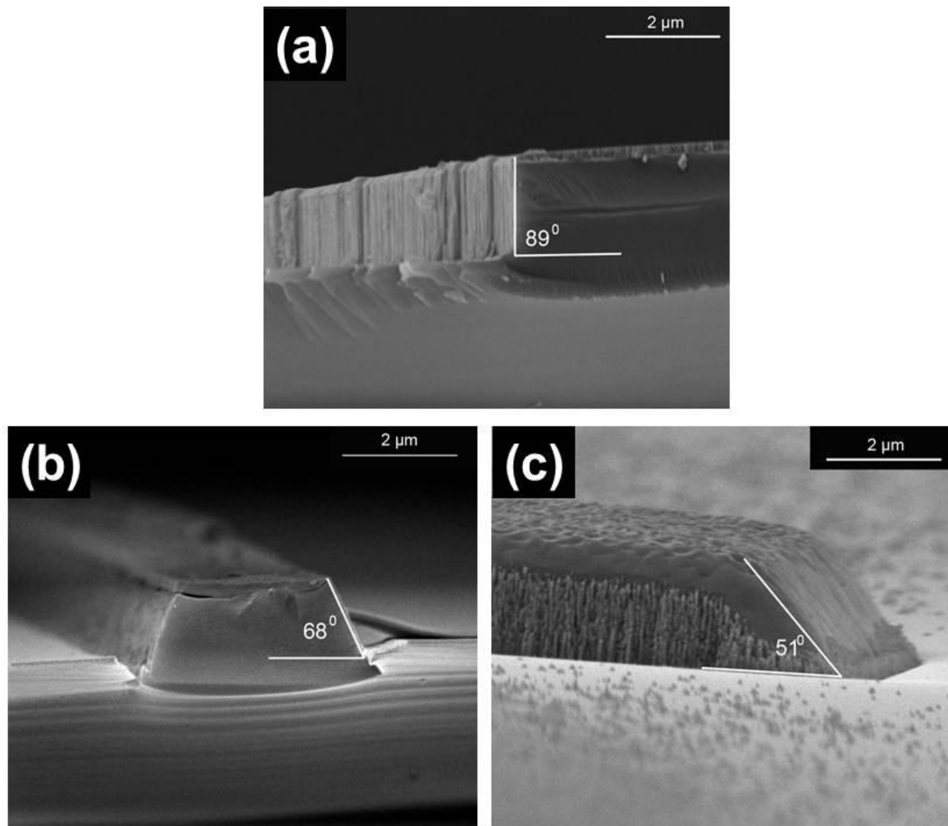

Figure 2.16: SEM images of etched $LiNbO_3$ cross section with slope angle at different total gas flow of (a) 10 sccm (b) 30 sccm (c) 60 sccm.

With relatively high gas flow and optimized etching conditions, structures with deep plasma $LiNbO_3$ etching (3.5 μm), ultra-smooth surfaces and high anisotropy were achieved, as shown in Fig. 2.17. This is the deepest and most vertical low-residue $LiNbO_3$ structure yet demonstrated using ICP in a single-step etching. As is clear in Fig. 2.17, trenching phenomenon appeared on both sides of the ridge. This was due to additional etching by ion reflection and charging of the sidewall. Fig. 2.17 shows the nearly vertical but very rough sidewalls which were caused by both imperfect photolithography and etching process. In the next section we focus on the issue of sidewall roughness reduction.

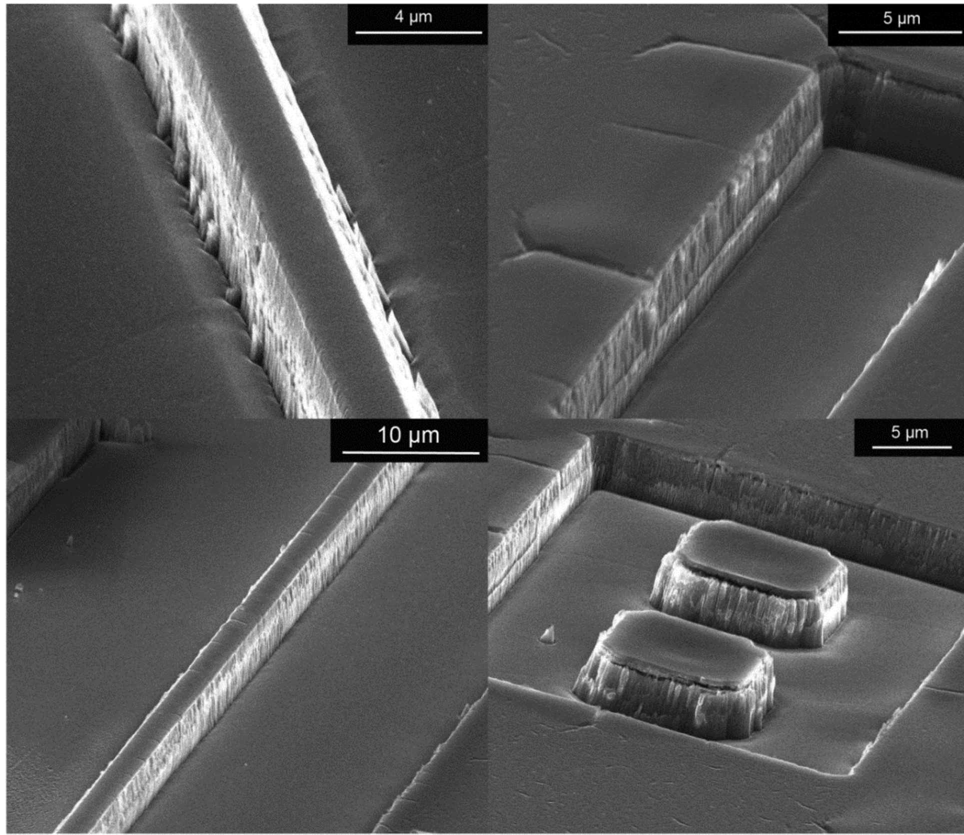

Figure 2.17: SEM images of deep and highly anisotropic $LiNbO_3$ etching at 3.5 μm depth under 800 W ICP power, 90 W RIE power, 7 mTorr pressure, and 50 sccm SF_6/Ar gas mixture. The total etching time is 30 minutes.

2.5 Reducing the sidewall roughness with GCIB techniques

One main factor that degrades waveguide performance is the scattering loss due to sidewall roughness. This is a common problem in dry etching process for any material. This problem is amplified when optoelectronic integrated circuits (OEICs) are miniaturized to the micro and nanometer scale, as the roughness of the sidewalls become significant in relation to the device size. Many techniques have been developed to mitigate sidewall roughness. The introduced roughness is chiefly due to the replication of the roughness present in the mask, and as a result, careful choice and optimizing of the etching mask can sidestep

some of these issues [18]. Lee *et al.* reported a large improvement in the sidewall roughness of etched holes in InP by adding nitrogen gas into a Cl_2/BCL_3 plasma in an ICP-RIE etching process [19]. The results show that when the N_2 ratio is above 65%, smooth sidewalls can be obtained. Another method is to introduce an additional step to smooth sidewalls after fabrication. One example from another material system is the oxidation smoothing technique for Si waveguides [20]. The rough etched sidewalls of a Si waveguide can be oxidized to form thin SiO_2 films, to be removed by HF acid, resulting in relatively smooth sidewalls. Similar work has been done to smooth etched AlGaAs ridge structures [21]. In this work etched AlGaAs ridges were oxidized and removed by a dilute buffered HF solution. However, these methods are mainly based on chemical reactions .It is difficult to find a chemical to react with $LiNbO_3$ to form a layer which can be removed by acid. Therefore they are not suitable for smoothing the sidewalls of an etched $LiNbO_3$ ridge structure. The importance of $LiNbO_3$ as an optical material creates the need for sidewall smoothing techniques on $LiNbO_3$. However, until now little effort had been devoted to this area.

2.5.1 Introduction of the GCIB technique

Recently the Gas Cluster Ion Beam (GCIB) technique has been developed as a dry polishing technique for surface and sidewall smoothing. GCIB is a new type of ion beam developed by Yamada [22], which is different from a monomer ion beam. It has both low energy and high current features. A gas cluster contains tens of thousands of atoms that are accelerated after ionization. In the cluster the number of atoms is much larger than the number of charges. Therefore, it is able to transport much larger number of atoms than a monomer

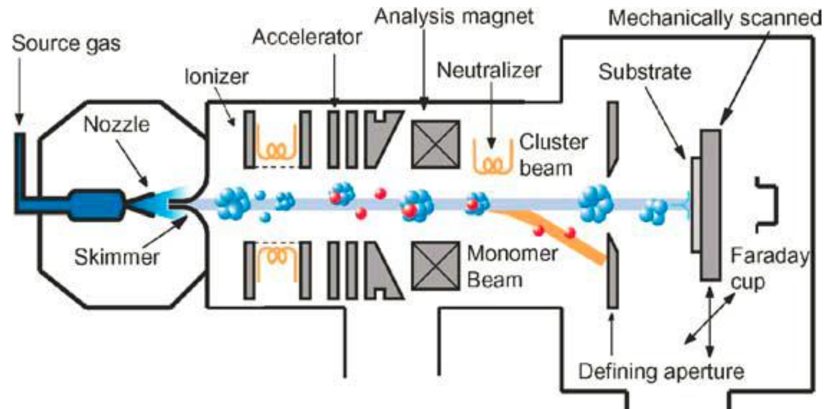

Figure 2.18: Schematic diagram of a GCIB system [23].

ion beam with the same current. In addition, the energy of an atom in a gas cluster is much lower than that of a monomer ion beam [23].

GCIB is very useful material modification method which is used to clean surfaces and smooth rough sidewalls. Compared with the monomer ion sputtering where the surface atoms are removed layer by layer, largely resulting in an unchanged surface morphology, the cluster ion beam sputtering mechanism is completely different and is termed as "lateral sputtering" [24]. When cluster ion atoms arrive at the surface, multiple-collisions occur between incident atoms and the sample atoms, resulting in a large number of atoms sputtered along the plane with with the surface. As a result of this unique mechanism, GCIB can be used for surface and sidewall smoothing processes. In a remarkable publication the sidewall of a Si pillar structure etched by ICP was smoothed by SF_6 GCIB irradiations [25]. Before the treatment, the Si pillars' sidewalls had periodic scalloping produced by cyclic etching and protective coating. This scalloping completely disappeared after GCIB treatment. Many gas sources including Ar, O_2, N_2 and reactive gas mixtures like SF_6 and CF_4 are used to produce cluster ion beams. In our experiment, an Ar GCIB is used to physically smooth the surface and sidewall, as shown in Fig. 2.18. Neutral

clusters are formed by supersonic expansion of a gas from a nozzle and pass through an aligned skimmer to an ionizing chamber. Then the ionized clusters are accelerated and monomer ion beams are filtered out through a magnetic filter. A neutralizer is used to avoid the charging effect. Mechanical scanning is employed and the sample stage is designed for applying various incident angles.

2.5.2 Results of Ar GCIB irradiations on etched $LiNbO_3$ structures

In this work we have collaborated with Prof. Toyoda from the University of Hyogo (Japan) to apply GCIB techniques to smooth etched $LiNbO_3$ ridge sidewalls. As previously discussed, a $LiNbO_3$ wafer was firstly proton exchanged in benzoic acid at 235°C for 5 hours. Ridge structures were defined by photolithography, metallic mask transformation and ICP etching. After these procedures the samples were sent to the University of Hyogo for GCIB smoothing. Fig. 2.19 shows the position of the sample and beam direction in the GCIB chamber.

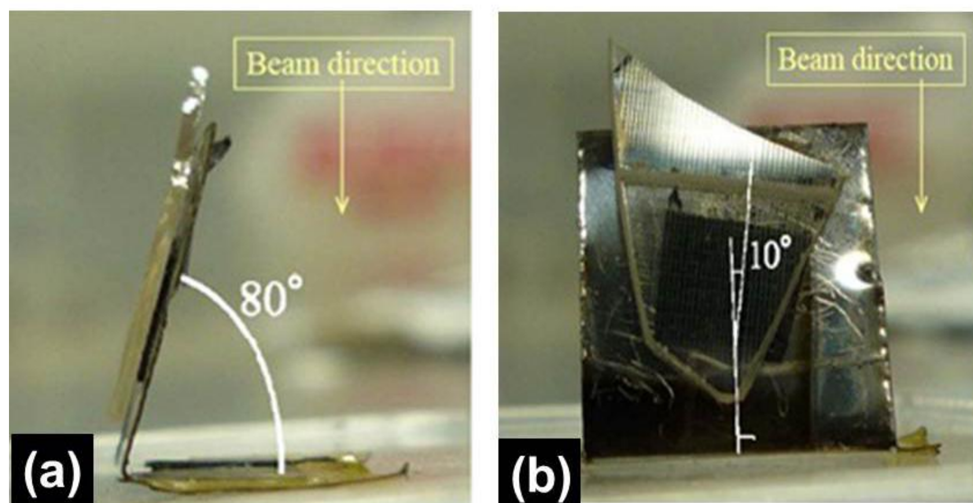

Figure 2.19: Illumination of the sample holder and the ion irradiation direction.

The ion beam was incident along the vertical direction from the top of the chamber. The stage was bent at an 80° angle to the bottom of the chamber (Fig. 2.19 (a)). Samples were stuck on the stage to make sure the etched ridge structures have been rotated 10° from the vertical direction, as shown in Fig. 2.19 (b). Firstly low dose irradiation was used. The Ar GCIB irradiation was carried out with total acceleration voltage of 20 KeV and ion dose of 3×10^{16} ions/cm^2. The duration of GCIB irradiation was 1 hour. Fig. 2.20 shows the SEM image of etched $LiNbO_3$ ridge structures before and after GCIB irradiation. The SEM images were taken at a 15° tilt angle to show both the surface and sidewall of the etched ridge clearly. It can be observed from Fig. 2.20 that before GCIB, both the surface and sidewall of our etched $LiNbO_3$ samples were very rough. After GCIB irradiation, the bumpy surface became smoother although there are some hillocks on the surface due to the irradiation. The top smooth surface of the ridge structure is unaffected by the GCIB process. Therefore, the surface smoothing effect by GCIB irradiations is very effective in smoothing the rough surface, but it will not cause any deterioration to an already smooth surface. However, after the GCIB process, the sidewalls still show some roughness. This is mainly due to using an insufficient ion dosage.

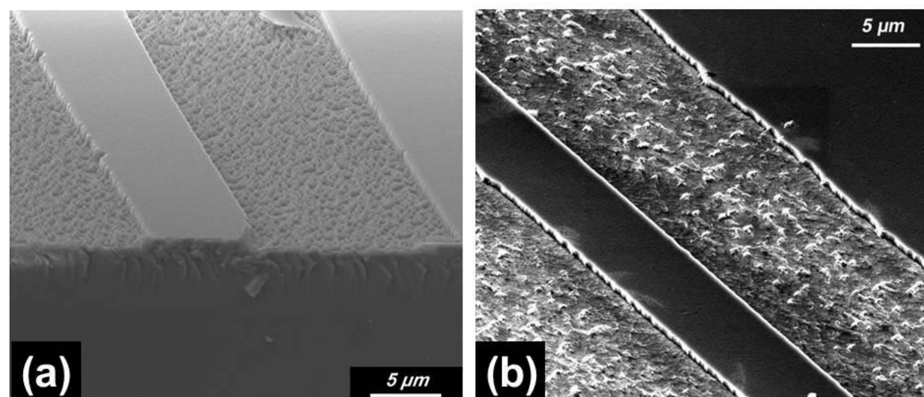

Figure 2.20: SEM images of the surface and sidewall conditions of etched $LiNbO_3$ structures. (a) before GCIB process; (b) after GCIB process.

To study the smoothening effect dependence on the ion dosage, the total acceleration voltage kept constant at 20 KV. Different ion doses were used: 3×10^{16} ions/cm^2, 1×10^{17} ions/cm^2 ， and 2×10^{17} ions/cm^2. Fig. 2.21 shows a comparison of SEM images of $LiNbO_3$ samples after different GCIB ion dose irradiations. It can be seen that when ion dose increased from 3×10^{16} ions/cm^2 (Fig. 2.21 (a)) to 1×10^{17} ions/cm^2 (Fig. 2.21 (b)), the rough surfaces were flattened although many small "valleys" appear on the surface. The zigzag shape of the sidewall disappeared. However, the ridges were not completely smoothed. Nonetheless, when the ion dose further increased to 2×10^{17} ions/cm^2 (Fig. 2.21 (c)), both surface and sidewall became smooth enough for optical device applications. Consequently, increasing the ion dose concentration improved both surface and sidewall roughness significantly. It is evident that Ar GCIB irradiation is an effective smoothing technique for $LiNbO_3$ optical devices.

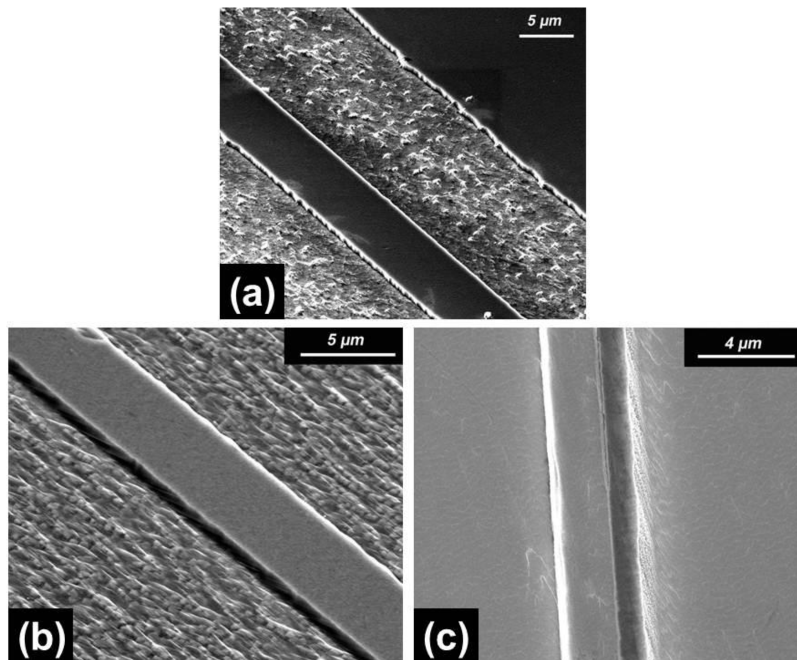

Figure 2.21: SEM images of etched $LiNbO_3$ after GCIB with 20 KeV Ar irradiations. (a) ion dose=3×10^{16} ions/cm^2; (b) ion dose=1×10^{17} ions/cm^2; (c) ion dose=2×10^{17} ions/cm^2.

2.6 Conclusion

In this chapter we reported the etching characterization of $LiNbO_3$ by ICP. Firstly the etching characteristics under various metallic masks and different gases were studied. We find the roughness can be avoided greatly when using a Cr mask and SF_6 gas in the etching process. Mask selectivity > 15:1 was achieved under both Ni and Cr conditions. A relatively high etch rate of 97.5 nm/min was achieved by using CHF_3/ Ar gases and a Cr mask. Using a Ni mask and CHF_3/Ar gases also lead to a high etching rate: approximately 80 nm/min. Subsequently, $LiNbO_3$ etching was studied in SF_6/Ar plasmas as a function of process parameters to achieve deep anisotropic etching and a smooth surface. The effects of He backside cooling, RIE power and total gas flow were investigated. The results showed that a high etching rate and a smooth post-etch surface condition can be obtained without He cooling. Higher RIE power can improve the etching rate and surface condition, also leading to highly anisotropic etching. The total gas flow can significantly affect the etching rate, anisotropy and surface roughness. The etching rate can be improved to 98.6 nm/min when the total gas flow increases to 25/25 sccm (SF_6/Ar), while the slope angle will decrease from 89° at 5/5 sccm SF_6/Ar to 51° at 30/30 sccm SF_6/Ar. Deep (>3 μm) and highly anisotropic PE $LiNbO_3$ structures with ultra-smooth surfaces were achieved in a single-step run, with parameters of 30 minutes at 800 W ICP power, 90 W RIE power, 7 mTorr chamber pressure and 50 sccm total gas flow. Finally Ar GCIB irradiation was employed to smooth the rough sidewalls of etched $LiNbO_3$ structures for the first time and irradiation parameters were optimized to achieve good sidewalls and surface condition. These results show promise that deep etching on $LiNbO_3$ may be an attractive

method to realize a variety of structures and fabricate optical and MOEMS devices.

References

[1] C. Wei-Lin, C. Rei-Shin, L. Jeng Hong, W. Wang, and Seen, "Lithium niobate ridge waveguides by nickel diffusion and proton-exchanged wet etching," IEEE Photonics Technology Letters **7**, 1318-1320 (1995).

[2] D. M. Gill, D. Jacobson, C. A. White, C. D. W. Jones, Y. Shi, W. J. Minford, and A. Harris, "Ridged $LiNbO_3$ modulators fabricated by a novel oxygen-ion implant/wet-etch technique," Journal of Lightwave Technology **22**, 887-894 (2004).

[3] H. Hu, R. Ricken, and W. Sohler, "Low-loss ridge waveguides on lithium niobate fabricated by local diffusion doping with titanium," Applied Physics B **98**, 677-679 (2010).

[4] I. E. Barry, G. W. Ross, P. Smith, and R. W. Eason, "Ridge waveguides in lithium niobate fabricated by differential etching following spatially selective domain inversion," Applied Physics Letters **74**, 1487-1488 (1999).

[5] H. Hu, R. Ricken, W. Sohler, and R. B. Wehrspohn, "Lithium niobate ridge waveguides fabricated by wet etching," IEEE Photonics Technology Letters **19**, 417-419 (2007).

[6] A. Ródenas, A. H. Nejadmalayeri, D. Jaque, and P. Herman, "Confocal Raman imaging of optical waveguides in $LiNbO_3$ fabricated by ultrafast high-repetition rate laser-writing," Optics Express **16**, 13979-13989 (2008).

[7] G. Y. Si, A. J. Danner, S. L. Teo, E. J. Teo, J. H. Teng, and A. A. Bettiol,

"Photonic crystal structures with ultrahigh aspect ratio in lithium niobate fabricated by focused ion beam milling," Journal of Vacuum Science and Technology B **29**, 021205 (2011).

[8] W. S. Yang, W. K. Kim, D. H. Yoon, J. W. Lim, M. Isshiki, and H. Y. Lee, "Surface roughness of Ti : $LiNbO_3$ etched by Ar/C_3F_8 plasma and annealing effect," Journal of Vacuum Science and Technology B **24**, 675-677 (2006).

[9] W. J. Park, W. S. Yang, W. K. Kim, H. Y. Lee, J. W. Lim, M. Isshiki, and D. H. Yoon, "Ridge structure etching of $LiNbO_3$ crystal for optical waveguide applications," Optical Materials **28**, 216-220 (2006).

[10] S. Benchabane, L. Robert, J. Y. Rauch, A. Khelif, and V. Laude, "Highly selective electroplated nickel mask for lithium niobate dry etching," Journal of Applied Physics **105**, 094109 (2009).

[11] H. Hu, A. P. Milenin, R. B. Wehrspohn, H. Hermann, and W. Sohler, "Plasma etching of proton-exchanged lithium niobate," Journal of Vacuum Science and Technology A **24**, 1012-1015 (2006).

[12] Z. Ren, P. J. Heard, J. M. Marshall, P. A. Thomas, and S. Yu, "Etching characteristics of $LiNbO_3$ in reactive ion etching and inductively coupled plasma," Journal of Applied Physics **103**, 034109 (2008).

[13] G. Ulliac, B. Guichardaz, J.Y. Rauch, S. Queste, S. Benchabane, and N. Courjal, "Ultra-smooth $LiNbO_3$ micro and nano structures for photonic applications," Microelectronic Engineering **88**, 2417-2419 (2011).

[14] O. Yavuzcetin, H. P. Novikov, R. L. Dally, S. T. Malley, N. R. Perry, B. Ozturk, and S. Sridhar, "Photonic crystal fabrication in lithium niobate via pattern transfer through wet and dry etched chromium mask," Journal of Applied Physics **112**, 074303 (2012).

[15] L. Gui, H. Hu, M. Garcia Granda, and W. Sohler, "Local periodic poling of ridges and ridge waveguides on X- and Y-Cut LiNbO3 and its application for second harmonic generation," Optics Express **17**, 3923-3928 (2009).

[16] J. S. Parker, E. J. Norberg, R. S. Guzzon, S. C. Nicholes, and L. A. Coldren, "High verticality InP/InGaAsP etching in $Cl_2/H_2/Ar$ inductively coupled plasma for photonic integrated circuits," Journal of Vacuum Science and Technology B **29**, 011016 (2011).

[17] H. Nagata, N. Mitsugi, K. Shima, M. Tamai, and E. M. Haga, "Growth of crystalline LiF on CF_4 plasma etched $LiNbO_3$ substrates," Journal of Crystal Growth **187**, 573-576 (1998).

[18] U. K. Chakrabarti, S. J. Pearton, and F. Ren, "Sidewall roughness during dry etching of InP," Semiconductor Science and Technology **6**, 408 (1991).

[19] K. H. Lee, S. Guilet, G. Patriarche, I. Sagnes, and A. Talneau, "Smooth sidewall in InP-based photonic crystal membrane etched by N_2-based inductively coupled plasma," Journal of Vacuum Science and Technology B **26**, 1326-1333 (2008).

[20] K. K. Lee, D. R. Lim, L. C. Kimerling, J. Shin, and F. Cerrina, "Fabrication of ultralow-loss Si/SiO_2 waveguides by roughness reduction," Optics Letters **26**, 1888-1890 (2001).

[21] D. Liang and D. C. Hall, "Reduction of etched AlGaAs sidewall roughness by oxygen-enhanced wet thermal oxidation," Applied Physics Letters **91**, 061110 (2007).

[22] I. Yamada, “New horizons in material processing with GCIB,” Conference Proceedings of 14th Ion Sources Ion-Assisted Technol.,

Tokyo, Japan, 227–235,1991.

[23] N. Toyoda and I. Yamada, "Gas Cluster Ion Beam Equipment and Applications for Surface Processing," IEEE Transactions on Plasma Science **36**, 1471-1488 (2008).

[24] Z. Insepov and I. Yamada, “Molecular dynamics simulation of cluster ion bombardment of solid surfaces,” Nuclear Instruments and Methods in Physics Research Section B **99**, 248–252 (1995).

[25] E. Bourelle, A. Suzuki, A. Sato, T. Seki, and J. Matsuo, "Sidewall polishing with a gas cluster ion beam for photonic device applications," Nuclear Instruments and Methods in Physics Research Section B: Beam Interactions with Materials and Atoms 241, 622-625 (2005).

[26] J. Deng, G. Y. Si, and A. J. Danner, "Dry etching of $LiNbO_3$ using inductively coupled Plasma," in 2010 Photonics Global Conference Singapore (2010).

[27] J. Deng, W. Jia, C. E. Png, G. Y. Si, J. Son, H. Yang, and A. J. Danner, "Deep anisotropic $LiNbO_3$ etching with SF_6/Ar inductively coupled plasmas," Journal of Vacuum Science and Technology B **30**, 011208 (2012).

Chapter 3 Suspended structures in $LiNbO_3$

3.1 Introduction

Many traditional methods such as Ti indiffusion have been proposed for fabricating $LiNbO_3$ waveguides. These methods, while well-established, have drawbacks of small index contrast yields and weak guiding. In this chapter we will describe a method of fabricating suspended microwire and microdisk structures on a bulk $LiNbO_3$ substrate such that maximum index contrast can be achieved.

The ion implantation method is widely used in the semiconductor industry to fabricate p-type and n-type Si wafers. Recently, ion implantation techniques have been widely studied and have become a very promising method to fabricate $LiNbO_3$ integrated photonic devices. Photonic structures and devices based on ion-beam processed $LiNbO_3$ waveguides or thin films have exhibited promising prospects for various applications. Our approach to fabricate suspended structures is based on the ion implantation method and subsequent wet etching.

3.1.1 Literature review of ion implantation used in $LiNbO_3$ photonic device fabrication

Ion implantation has been used to fabricate channel waveguides in the early years of optical device fabrication. Ion implantation forms an optical barrier beneath the surface, which generates low refractive index layers by nuclear damage caused by incident ions, e.g., He^+ or H^+. These barrier-confined refractive index profiles are quite typical for ion-implanted waveguides in various materials, and are particularly common for those related to light ion

implantation. The earliest work on light-ion-implanted $LiNbO_3$ waveguides was performed by Townsend *et al*. in 1976 [1]. Many researchers studied the refractive index change and showed that $LiNbO_3$ based planar waveguides produced by light ion implantation have a typical "barrier" n_o and "well+barrier" n_e profile. In addition, multiple-layer barriers can also be formed to construct multiple waveguides. This work was done by Chandler *et al.* in 1989 [2]. Heavy ions are not suitable to make a waveguide because most heavy ions will not only induce a nuclear damaged layer at the end of the ion track, but induce a nuclear damaged layer along the ions' trajectories as well. In addition, defects and damage will be induced both in waveguide and optical barrier regions if heavy ions are used. However, in recent years Wang *et al.* showed that low-dose middle-light mass ions such as Si or Ni with energies of 3 – 6 MeV can be used for waveguide fabrication. In this case, large refractive index changes can be achieved [3].

To fabricate 2D channel waveguides, two steps of light ion implantation are needed. Firstly, a light ion implantation is needed to form a planar waveguide with a barrier buried inside the $LiNbO_3$ wafer. Secondly, one should perform continuous lower-energy implantations with suitable stripe masking to build up the "sidewalls". The barrier walls have lower indices for both n_e and n_o, so in this configuration, the $LiNbO_3$ waveguides guide both extraordinary and ordinary polarized light.

Recently a new fabrication method preparing $LiNbO_3$ thin film was developed: crystal ion slicing (CIS) in combination with wafer bonding techniques. Thin films of $LiNbO_3$ which have been transferred to silicon and $LiNbO_3$ substrates can yield optical waveguides with high index contrast. This method is also called ''Smart Cut" [4], which was originally discovered and

applied for the fabrication of SOI wafers. One of the most significant advantages of CIS is the high vertical index contrast provided by the substrate. In addition, CIS provides the feasibility of large-scale thin layers (usually of several cm^2). CIS involves light ion implantation into a $LiNbO_3$ substrate to form a sacrificial layer, which makes a thin film of $LiNbO_3$ that can be lifted off from the bulk substrate and bonded with another substrate. This method was first applied to $LiNbO_3$ in 1998 by Levy *et al.*, producing a 9 μm-thick $LiNbO_3$ film with preserved crystal properties by using 3.8 MeV He ions at a dose of 5×10^{16} ions/cm^2 [5]. The thickness of the film was reduced by Payam *et al.* in 2005 [6]. They used 200 KeV He ions to implant bulk $LiNbO_3$ and subsequently bonded $LiNbO_3$ wafers onto a SiO_2 film which was deposited on another $LiNbO_3$ wafer. After heat treatment at 220°C for 14 hours, a 680 nm-thick $LiNbO_3$ thin film was formed. It has been demonstrated that the crystal quality and optical properties for the transferred layer are comparable to those of bulk single crystals. Subsequently, an excellent work was done by A. Guarino *et al*. in 2007 [7]: due to the strict requirements of direct bonding with respect to surface roughness and imperfections, they bonded $LiNbO_3$ film on BCB, a well-known adhesion material. Following this work, a ring resonator on $LiNbO_3$ film was successfully fabricated. This breakthrough showed the great potential of $LiNbO_3$ in chip-scale integrated optical devices.

In spite of the above success, there was a reduction in the electro–optic coefficient of $LiNbO_3$ thin film compared with the bulk one, owing to implantation induced defects. Thermal annealing can reduce these defects, but not eliminate them. Additionally, the required temperature is about 800°C, higher than the maximum temperature allowed in BCB processes (320°C), so thermal annealing cannot be used in a $LiNbO_3$ film bonded on BCB layer.

There is a way to overcome this problem. By applying a chemical mechanical polishing process to polish the SiO_2 layer, a $LiNbO_3$ thin film can be directly bonded onto an SOI wafer, as reported by Hu *et al.* [8]. Large area films (3 inch lateral dimension) have been fabricated and have become a promising material to make $LiNbO_3$-based devices.

Ion beam-enhanced etching (IBEE) is a combination of ion implantation and chemical wet etching. After ion implantation, large numbers of defects are induced due to energy transfer to the crystal lattices, forming amorphized layers. Consequently, the chemical resistance of this damaged layer is reduced. As a result, the irradiated regions can be removed by wet chemical etching. Normally, the etching rate is mainly determined by the damage density and the crystallographic orientation. Compared with the CIS method, IBEE allows ultrathin $LiNbO_3$ films and hence monolithic free-standing structures become possible. In addition, maximum index contrast can be achieved in free-standing membranes.

The IBEE technique was first employed to fabricate ridge waveguides. In 2004, D. M. Gill *et al.* reported that the then-novel ion beam enhanced etching (IBEE) process was used to fabricate a deep (3.5 μm) ridge waveguide [9]. Subsequently, Hartung *et al.* developed a method to form Zn-doped $LiNbO_3$ ridge waveguides by combining liquid phase exitaxy (LPE) and IBEE [10]. Similar Ar ion implantation/wet-etching processes were applied eight times, creating a ridge with a depth of 3.7 μm. In particular a side wall angle of almost 90° was demonstrated.

Then, excellent work was carried out by Schrempel *et al.* in 2009 [11], in which $LiNbO_3$ membranes with an ultralow thickness of 200 nm were demonstrated. In their process, different ion fluences from 1×10^{16} cm^{-2} to

6.5×10^{16} cm^{-2} were used to create amorphous layers and wet etching was then performed in a 3.7% HF solution at 40 ^{o}C. They found that when the ion fluences exceeded a critical value, cracks were formed in the surface layer owing to the thin membrane which could not stand the stress caused by gas bubbles. Consequently, ion irradiation preformed at low temperature of 100 K was developed to overcome this problem.

Recently, IBEE has been applied to realize complex guiding devices in $LiNbO_3$ such as PhCs. In 2010, a 450 nm suspended PhC slab was fabricated by Hartung *et al.* [12]. In this work two ion implantation steps were used; one was for the photonic crystal structure and another was for a buried damaged layer, which formed the suspended structure. They have shown well-preserved optical properties relative to those of bulk crystals. Similar work has been done in [13], in which selective implantations were performed by using Cr as an implanted mask. However, the optical characterization of such PhC has not yet been investigated experimentally.

Very recently, Wang *et al*. fabricated three-dimensional microstructures in $LiNbO_3$ by using IBEE in 2011, as shown in Fig. 3.1 [14]. In this work the undercut structures included microwires, microdisks and microrings on z-cut $LiNbO_3$ and were fabricated with selective ion implantation and wet etching. A Cr film was deposited and patterned by photolithography to act as a hard mask. Because HF has a high etching rate on the z-face of $LiNbO_3$, both the exposed $LiNbO_3$ substrate and the buried amorphous layers can be etched quickly, leaving the suspended microstructures under the Cr film protected. The main difference compared with Hartung's work is that only one implantation process was required. Subsequently a microdisk resonator was fabricated by this group in 2012 [15]. Thermal treatment was used to reshape the microdisk

and a tapered fiber was used to measure the transmission spectrum. An FSR of 16.43 nm and Q factor of 2.6×10^4 were obtained. These results indicated a great potential application of such a microdisk resonator in $LiNbO_3$. However, one of the main drawbacks is that this fabrication procedure can only be applied to z-cut LN samples due to the considerable etching rate of HF for the −z face of $LiNbO_3$. This method cannot make use of the largest electro-optical coefficient r_{33} in $LiNbO_3$, which requires etching on x or y-cut samples. In addition, the etching time to form a ridge structure and to remove the buried amorphous layer is very long, around 10 to 24 hours.

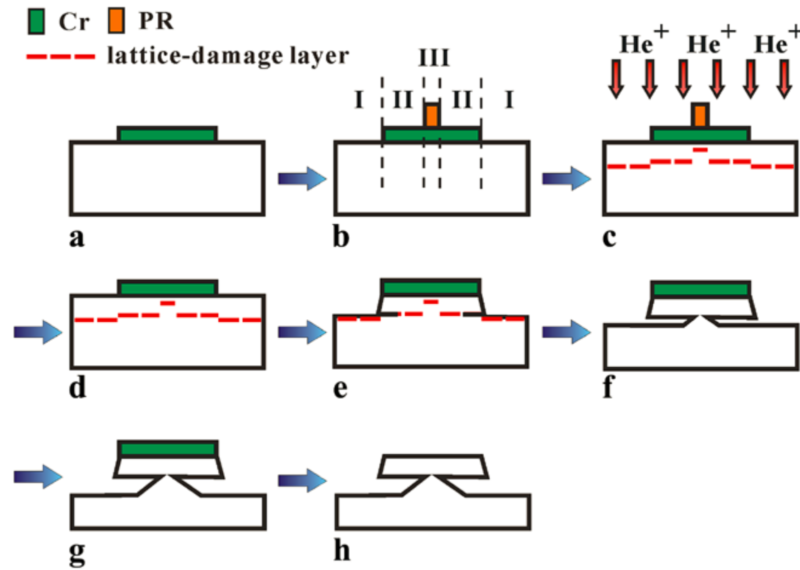

Figure 3.1: Fabrication process of a three-dimensional microstructure. (a) Cr-film deposition; (b) PR patterning; (c) Ion implantation; (d) PR removal; (e) Etching in diluted HF; (f) Etching out the lattice-damaged layer in region II; (g) Completing etching; (h) Cr film removal [14].

3.1.2 Motivation

Our group developed a different fabrication procedure based on the IBEE technique at the same time as Hartung's and Wang's work reviewed above [16]. In our process, focused ion beam (FIB) milling was combined with IBEE

to achieve a variety of structures. Unlike the use of different implantation steps or selective HF etching in previously reported work, FIB can directly mill patterns on a $LiNbO_3$ substrate without any mask. Additionally, there are no crystalline orientation limits and good anisotropic patterns can be obtained using FIB. In ref. [16] He^+ ions with single energy of 1 MeV were implanted normal to the surface of a z-cut $LiNbO_3$ sample and an air gap of approximately 350 nm was obtained.

In this chapter we continue this work by employing multi-energy implantations to achieve a large air gap, which is important for optical isolation. The Stopping and Range of Ions in Matter (SRIM) program was used to calculate the defect concentration distribution. Different implantation conditions were designed to achieve a desirable structure and experiment results were in good agreement with simulation. Based on these multi-energy implantations, different microstructures have been produced.

3.2 Fabrication procedures

In ion implantation, ions generally pass through a surface and get stopped at a certain depth (projected range). Ions lose their energy gradually near the surface where electron scattering dominates so the damage caused is not so high. The electron scattering does not disrupt the lattice strongly so the area near the surface is mostly crystalline, retaining bulk $LiNbO_3$ properties. When ions move towards the end of their trajectories, nuclear scattering dominates, causing significant damage to the crystal lattice. Most ions are trapped at a certain depth (also called “projected range”) beneath the surface, forming a damaged layer. This damaged layer is chemically reactive due to lattice defects and disorder. To accurately predict the projected range, damage and

ion distributions, an effective CAD package, SRIM is developed in [17]. We used this simulation tool to predict the implantation profile. Fig. 3.2 shows a SRIM simulation result of ion distributions for He^+ implantation into $LiNbO_3$ with an energy of 400 KeV. We can see that most ions stop in a 300 nm layer 1 μm beneath the surface. It indicates that implantation with 400 KeV can only form a slab with 1 μm thickness and an air gap with around 300 nm thickness, which is not enough for optical isolation.

The process of fabrication of suspended $LiNbO_3$ structures is divided into 3 steps, as shown in Fig. 3.3. Firstly, $LiNbO_3$ wafers were cut into 2×1.5 cm^2 samples and a 20 nm Au layer was coated on the top surface to prevent charging. After cleaning in acetone, isopropanol and deionized water, He^+ implantations with multiple-energies over an area of 1 cm × 1 cm were performed using a large area irradiation facility at the Centre for Ion Beam Applications, National University of Singapore. In order to obtain high quality suspended structures, all implantation conditions like current density and dose concentration were carefully controlled. During implantation the ion current density was optimized at 800 nA as larger current density can break the samples. In all implantation experiments the ion concentration was kept constant at 1×10^{16} $ions/cm^2$.

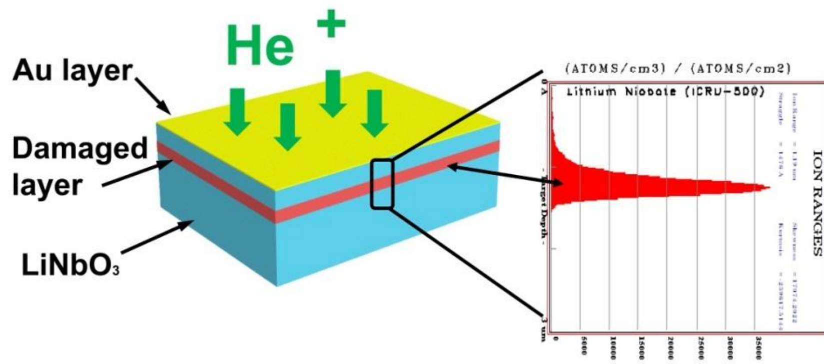

Figure 3.2: Schematic of ion implantation process (left) and a simulated ion distribution in $LiNbO_3$ after implantation by SRIM (right).

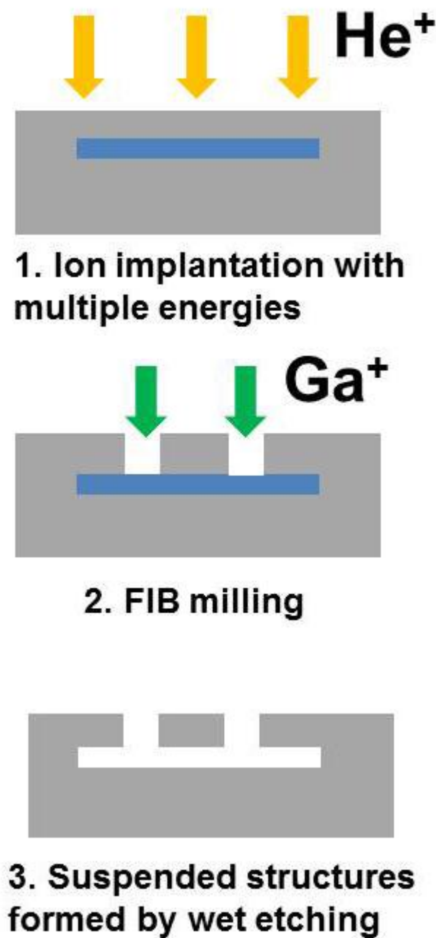

Figure 3.3: Fabrication process of the suspended $LiNbO_3$ structures.

Secondly, FIB milling was used to form different patterns and trenches which allow wet etchant to access the sacrificial layer. In our process a typical

voltage of 30 KV and current of 0.1 nA was chosen for milling of large patterns. Fig. 3.4 shows a pattern with a depth of 3 μm milled by FIB on one of the implanted samples. The duration of FIB milling to produce this pattern was 30 min. It can be seen that a pattern with an anisotropic shape can be obtained. The etchant can go through the etched pattern and reach the sacrificial layer to form an undercut structure. Then, samples were immersed into an acid (65% HNO_3 : 49% HF =2:1) at room temperature. The etching rate of the damaged layer is approximately 100 nm/min. After wet etching, suspended structures with an air gap were formed.

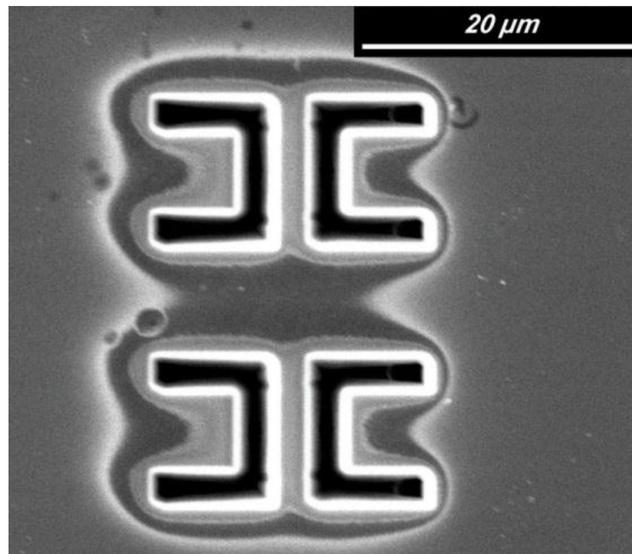

Figure 3.4: A pattern milled on an implanted $LiNbO_3$ substrate by FIB.

Different ion energy combinations can be used to adjust the implantation depth. Before the implantation process, ion energies are chosen based on SRIM calculation. Fig. 3.5 shows cross sectional SEM images of damaged layers formed by different implantation parameters and SRIM simulation results of the ion damage profile. As can be seen in Fig. 3.5 (a), by using ion energies of 400 KeV, 500 KeV and 650 KeV, an air gap of thickness 800 nm and a slab with thickness of 750 nm was obtained. The adjacent energies need

to be chosen to have a proper overlap of the damaged layer. By increasing the energy combination to 1 MeV, 1.1 MeV and 1.23 MeV, a large air gap with thickness over 1 μm and a deeper suspended slab with thickness of 1.7 μm was obtained, as can be seen in Fig 3.5 (b). In another case by carefully designing the energies to have a separation between these two damage profiles, an ultrathin membrane can be fabricated, as shown in Fig 3.5 (c). A suspended membrane with a thickness less than 150 nm was fabricated successfully by using ion energies of 1 MeV and 1.25 MeV. From Fig. 3.5 we can see all simulation profiles are in good agreement with experimental results.

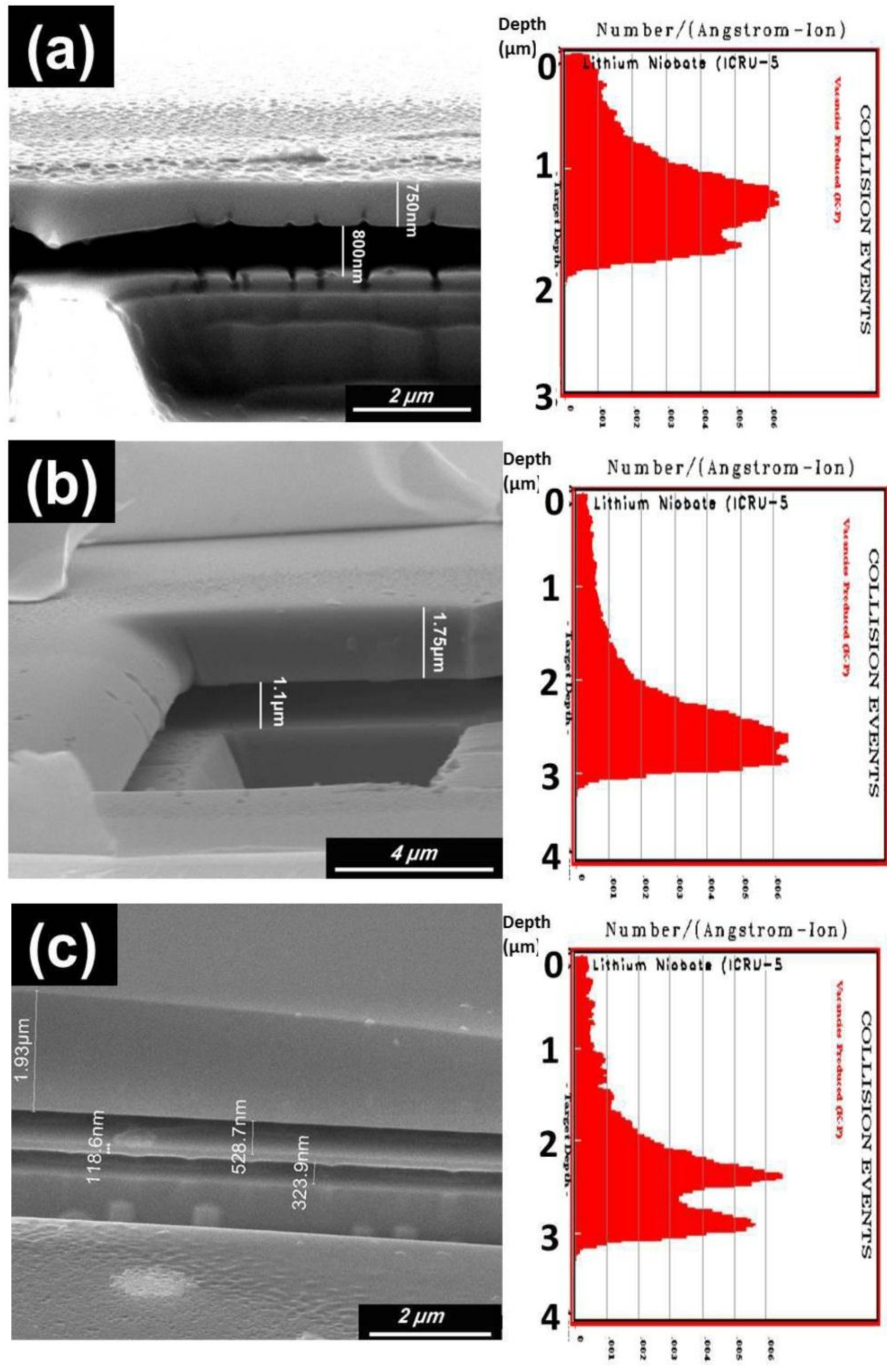

Figure 3.5: SEM images of the cross section of implanted $LiNbO_3$ samples after wet etching. Implantation energy is (a) 400 KeV, 500 KeV and 650 KeV, (b) 1 MeV, 1.1 MeV and 1.23 MeV, (c) 1 MeV and 1.25 MeV. The damage profile of each case is simulated, which is shown in the right side.

3.3 Fabrication of three-dimensional optical microstructures

3.3.1 Suspended microwires

Suspended waveguides are promising candidates for $LiNbO_3$ PICs due to the strong confinement of light. To demonstrate this possibility, suspended microwire structures with different dimensions were produced. Fig. 3.6 shows a fabricated suspended microwire with a length of 35 μm on a $LiNbO_3$ substrate implanted with a multiple energies of 1 MeV, 1.1 MeV, 1.23 MeV, and an ion dose of 1×10^{16} ions/cm^2. This suspended wire was pattered by FIB followed by wet etching. It can be seen that after wet etching both the surface and sidewall of the bridge structure are very smooth.

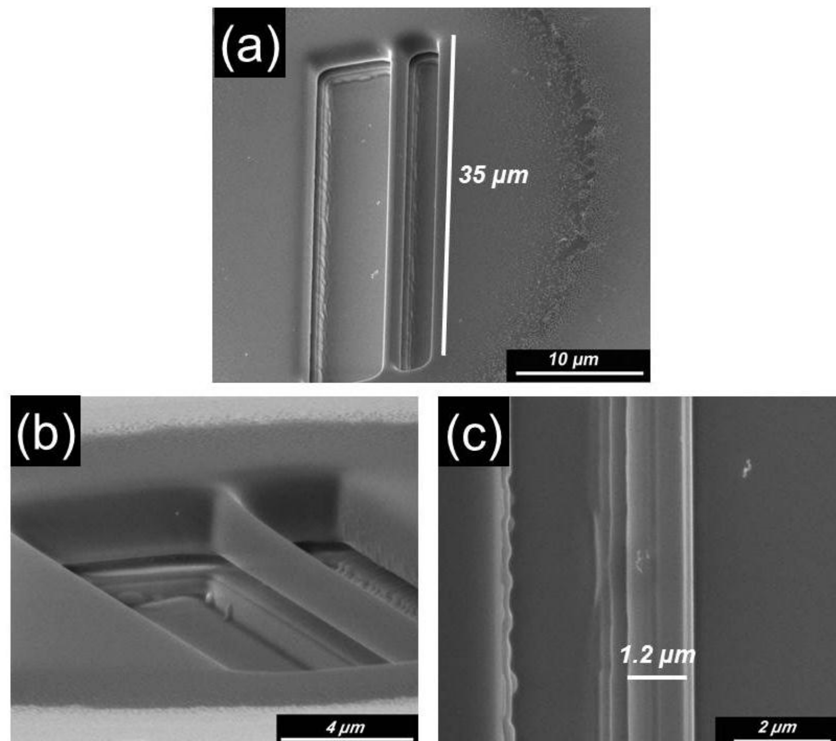

Figure 3.6: Fabricated suspended waveguide with a length of 35 μm, a width of 1.2 μm and an air gap of 1.1 μm. (a) View at an angle of 45°; (b) View at an angle of 70°; (c) Top view.

Figure 3.6 (b) shows the side view of this microwire structure. It can be clearly seen that the wire is suspended with a horizontally etched air gap of 1.1 μm which is good for optical isolation. As discussed in the previous section 3.2, the wire has the same thickness (1.7 μm) as that of the slab. The measured width of the wire after FIB milling is 1.5 μm, however, in Fig 3.6 (c) the SEM image shows that the width of the wire becomes smaller after wet etching (approximately 1.2 μm). It means that the suspended wire is also etched laterally by etching chemicals. This is mainly due to defects and distortion of the crystal lattice in the suspended area created by the ion implantation. From the SRIM simulations in the previous section 3.2 we can also notice that there are defects between the surface and sacrificial layers, although the concentration of the defects near the surface is much lower than in the sacrificial layer. This weak contrast of etch selectivity can significantly affect the fabrication of wires with narrow width. To demonstrate this, we fabricated a microwire structure with a designed width of 1 μm by FIB milling on the same sample. After the damaged layer was removed, the suspended bridge showed a different dimension, as shown in Fig. 3.7.

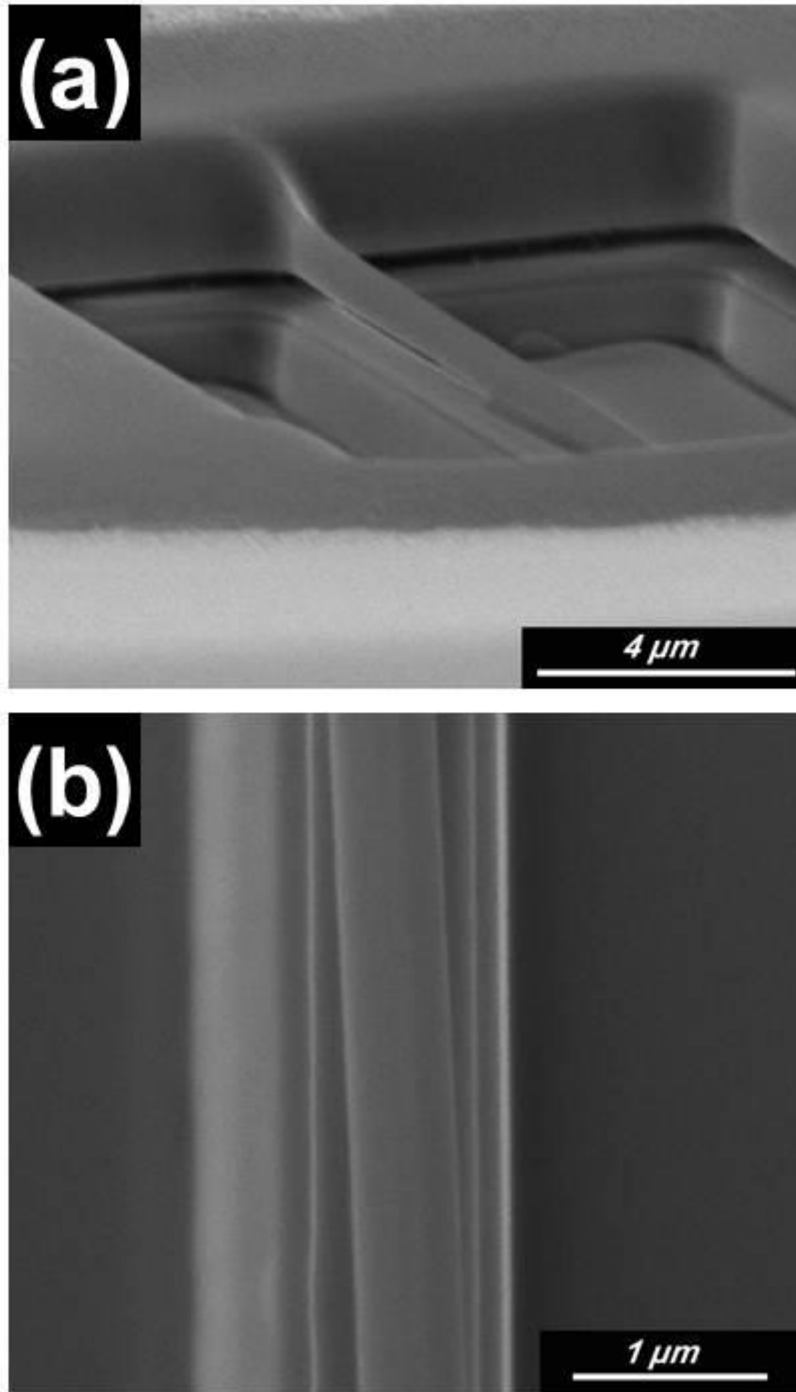

Figure 3.7: Fabricated suspended waveguide with a length of 35 μm, a width of 550 nm. (a) View at an angle of 45°; (b) Top view.

It can be seen from Fig. 3.7 (a) that the thickness of the bridge is about 800 nm, which is much smaller than the expected of 1.7 μm. From Fig. 3.7 (b) we can see that the width of the bridge is only 550 nm, which is only half of

the designed width. It is concluded that the dimension of a narrow structure is strongly altered after wet etching and is not easily reproducible. However, because the etch rate near the surface is an order of magnitude lower than the etch rate of the sacrificial layer, by careful control of the wet etching time a structure with larger dimensions will not be strongly affected.

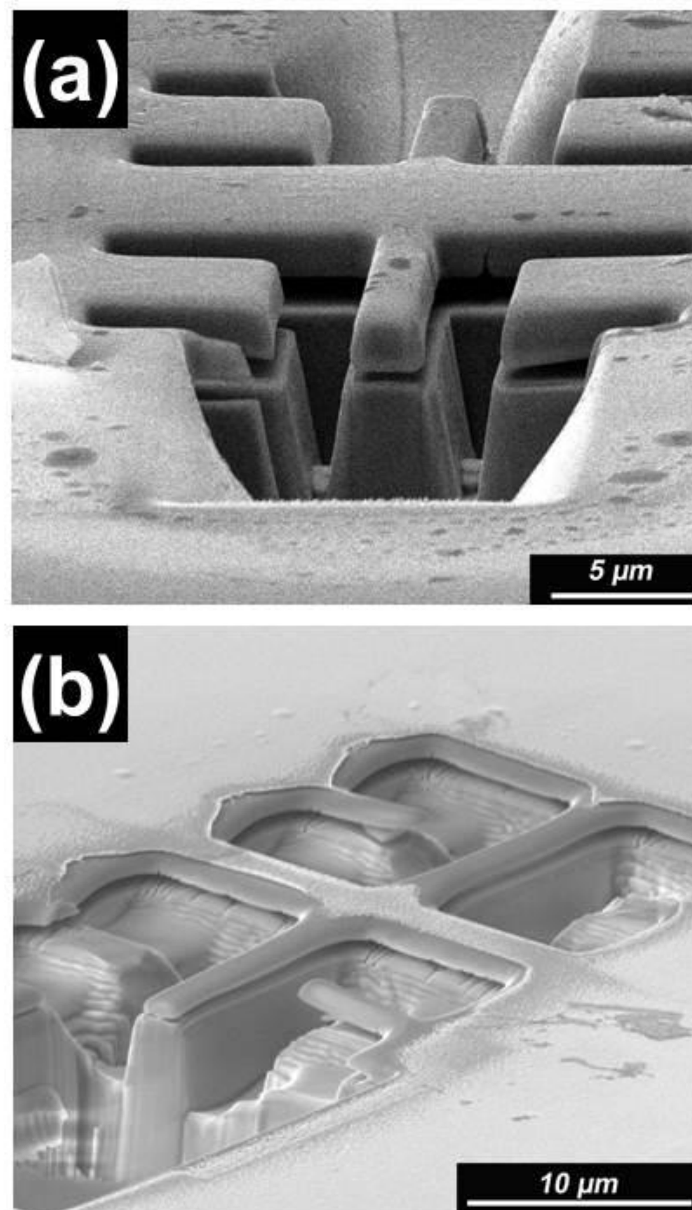

Figure 3.8: Two examples of the suspended structures with large width on samples implanted by (a) 1 MeV, 1.1 MeV and 1.23 MeV; (b) 400 KeV, 500 KeV and 650 KeV.

Figures 3.8 (a) and (b) show two examples of suspended structures with a large width fabricated on two samples implanted by different energies. Both SEM images show suspended waveguides with a width of 1.8 μm. In Fig. 3.8 (a) the thickness of the waveguide is 1.7 μm and the air gap is 1.1 μm. In Fig. 3 8 (b) the thickness of the waveguide is 900 nm and the air gap is 600 nm. We found that a lot of cracks appear in the suspended slab and the substrate when shallow implantation is carried out at low ion energies (Fig. 3.8 (b)). This problem may be due to the stress and re-emission of trapped gas [18]. The release of trapped gas will also cause surface blistering, especially in the implantation with high ion dose. This blistering phenomenon can be avoided by using low-temperature implantation [19].

3.3.2 Suspended microdisks

Microdisk resonators are an important optical component and have attracted a growing interest due to their high Q resonance. By milling a ring shape using FIB, a suspended microdisk resonator with flexible dimension can be easily fabricated. Fig. 3.9 shows an example of a ring shape fabricated by 20 min FIB milling. The ring width measured from the SEM image is 4.5 μm and the diameter of the microdisk is 13.3 μm. To fabricate it, a sample was placed in an acid mixture acid (65% HNO_3 : 49% HF =2:1) for 30 minutes which resulted in a lateral etch depth (in the air gap region) of 3 μm. Since the whispering-gallery mode of the optical wave is mainly localized near the outer sidewall [21], this lateral etch depth is enough for optical isolation.

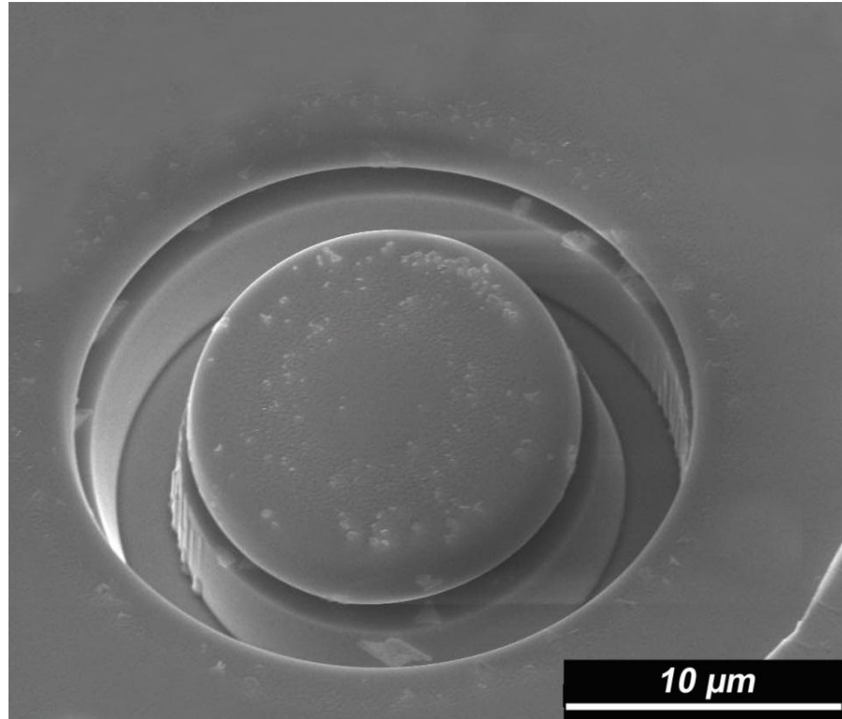

Figure 3.9: Fabricated suspended microdisk with a diameter of 13.3 μm and an air gap of 1.1 μm between micodisk and $LiNbO_3$ substrate.

3.3.3 Mechanical problems related to suspended microstructures

One problem encountered with the fabricated structures is the mechanical stress introduced in the fabrication process. After removing the sacrificial layer, there is a tensile residual stress in the suspended structure. In addition, when the sample is handled in the chemicals it suffers from the pressure of the liquid. Because no cracks are observed in the suspended waveguide, it is believed that these stresses are primarily responsible for the mechanical damage and breaking of the waveguide, as shown in Fig. 3.10. In addition, there is also a buckling phenomenon, which occurred on the cantilever due to the residual stress after removing the sacrificial layer. Fig. 3.11 shows an example of the deflection of a cantilever with 750 nm thickness in the vertical direction. The length of the cantilever is 6 μm and the displacement of the end part is about 670 nm. This phenomenon is only observed in the shallow implanted sample.

One can fabricate cantilevers without any deflection by choosing large ion implantation energies.

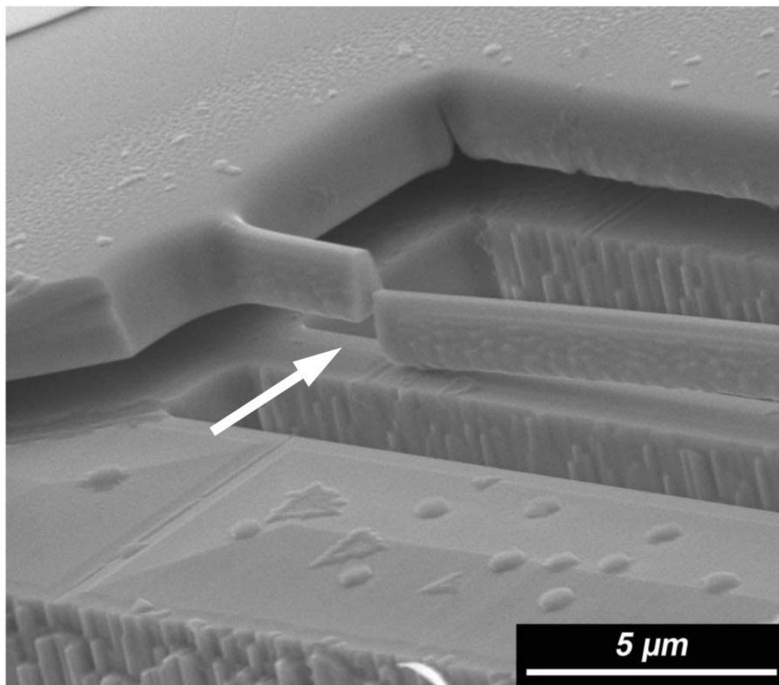

Figure 3.10: SEM image of a cracked suspended wire.

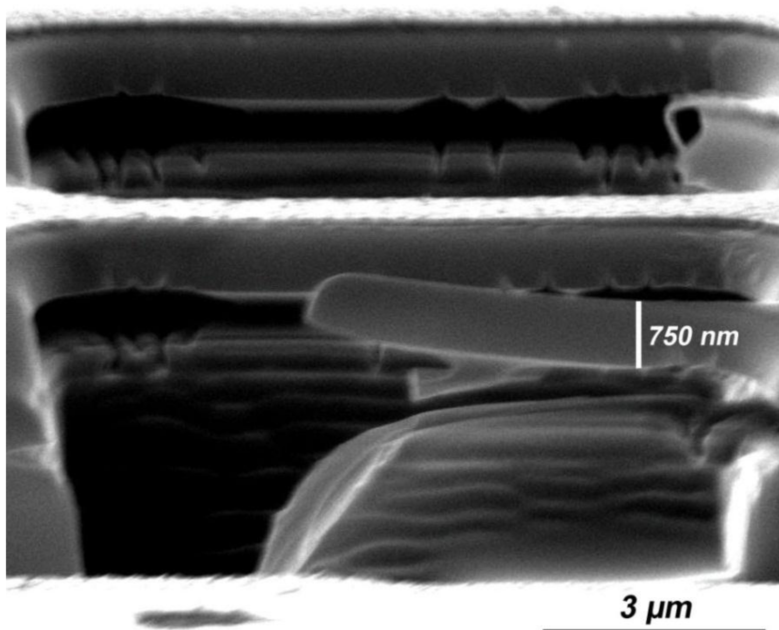

Figure 3.11: A buckling phenomenon occurred in a suspended wire.

3.3.4 The significance of PhC profile in a suspended membrane

A common problem in FIB milling is that etched holes do not have vertical sidewalls; FIB typically forms a conical shape instead of a cylindrical one. Fig. 3.12 (a) shows typical cross sections of FIB patterns. Different milling energies and times were used to achieve different depths of holes. However, all patterns show obvious conical shapes. This is mainly due to re-deposition of materials during etching. This conical shape of the holes, if actually used in an optical device, will lead to out-of-plane extrinsic losses in PhC waveguides. It will also strongly affect the performance of PhC based devices generally [20]. Our fabrication process allows the realization of cylindrical holes with vertical sidewalls, as shown in Fig. 3.12 (b). Due to the presence of an air gap, the milled cone is truncated and forms a PhC pattern with vertical air holes. It can be seen from Fig. 3.12 that the measured slope angle of sidewall is approximately 89°.

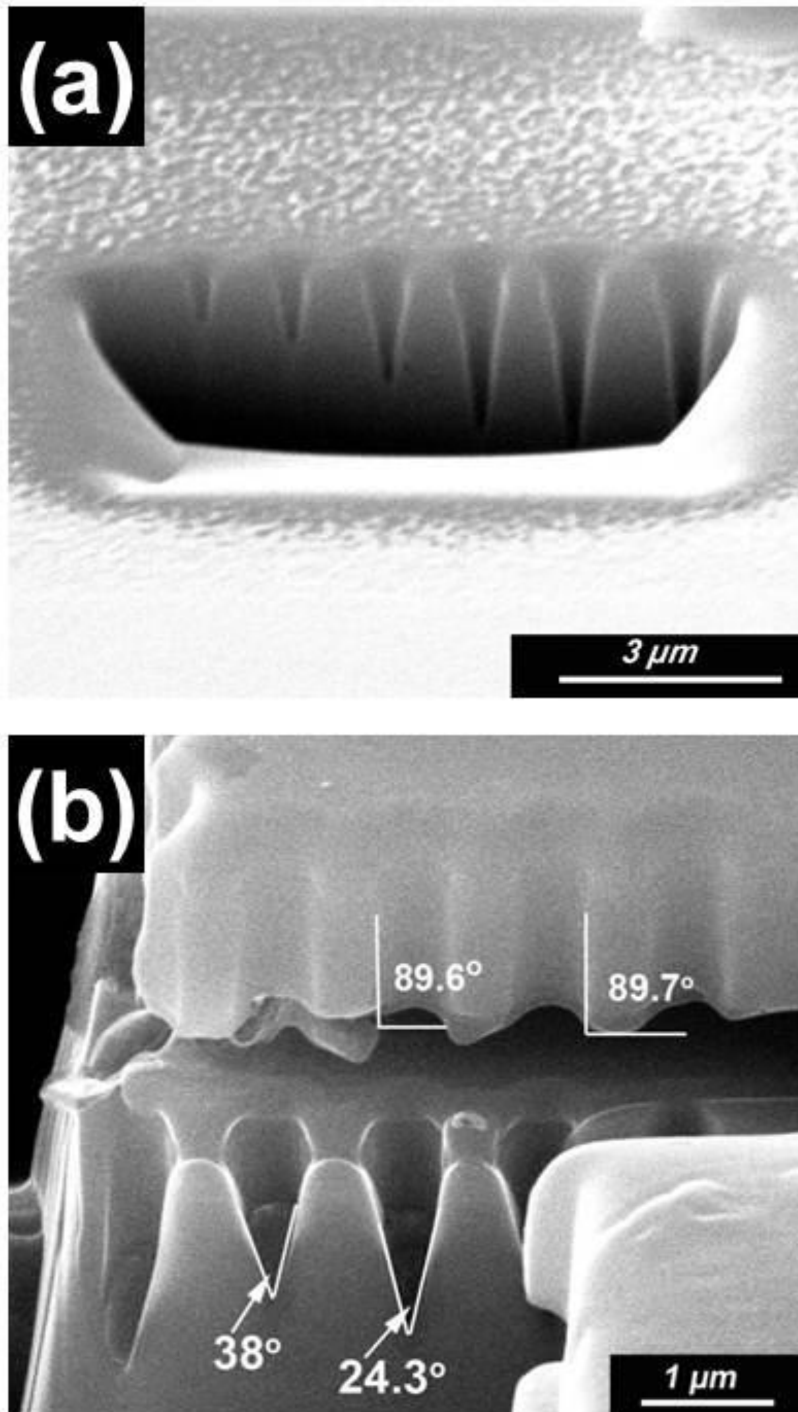

Figure 3.12: (a) Typical cross section of air holes milled by FIB; (b) cross section of truncated air holes in a suspended slab. The measured slope angle of the holes in the slab is 89°. The part of the hole with a conical shape is truncated by the air gap, of which the measured slope angle is less than 40°.

3.4 Conclusion

In this chapter we investigated the implantation properties of suspended structures in $LiNbO_3$ substrate by using He^+ ions with multi-energies. Different ion energies were determined to achieve different types of suspended structures like suspended slabs and ultrathin membranes. Experimental results agree well with SRIM simulations. Our structures show many advantages like high index contrast, adjustable slab thickness and milled holes with vertical sidewalls. The fabrication procedures that we have proposed here can be used to realize many different kinds of suspended optical components like microwires and microdisks.

References

[1] P. D. Townsend, P. J. Chandler, and L. Zhang, "Optical Effects of Ion Implantation," Cambridge University Press, Cambridge, 1994.

[2] P. J. Chandler, L. Zhang, J. M. Cabrera, and P. D. Townsend, "Missing modes in ion-implanted $LiNbO_3$ waveguides," Applied Physics Letters **54**, 1287-1289 (1989).

[3] H. Hu, F. Lu, F. Chen, B. Shi, x, Rong, K.-M. Wang, and D.-Y. Shen, "Monomode optical waveguide in lithium niobate formed by MeV Si^+ ion implantation," Journal of Applied Physics **89**, 5224-5226 (2001).

[4] H. Hu, R. Ricken, and W. Sohler, "Lithium niobate photonic wires," Optics Express **17**, 24261-24268 (2009).

[5] M. Levy, R. M. Osgood, Jr., R. Liu, L. E. Cross, G. S. Cargill, A. Kumar, and H. Bakhru, "Fabrication of single-crystal lithium niobate films by crystal ion slicing," Applied Physics Letters **73**, 2293-2295 (1998).

[6] P. Rabiei and W. H. Steier, "Lithium niobate ridge waveguides and modulators fabricated using smart guide," Applied Physics Letters **86**, 161115 (2005).

[7] A. Guarino, G. Poberaj, D. Rezzonico, R. Degl'Innocenti, and P. Gunter, "Electro-optically tunable microring resonators in lithium niobate," Nature Photonics **1**, 407-410 (2007).

[8] H. Hu, J. Yang, L. Gui, and W. Sohler, "Lithium niobate-on-insulator (LNOI): status and perspectives," Conference Proceedings of SPIE 84311 (2012).

[9] D. M. Gill, D. Jacobson, C. A. White, C. D. W. Jones, Y. Shi, W. J. Minford, and A. Harris, "Ridged $LiNbO_3$ modulators fabricated by a novel oxygen-ion implant/wet-etch technique," Journal of Lightwave Technology **22**, 887-894 (2004).

[10] H. Hartung, E.-B. Kley, A. Tünnermann, T. Gischkat, F. Schrempel, and W. Wesch, "Fabrication of ridge waveguides in zinc-substituted lithium niobate by means of ion-beam enhanced etching," Optics Letters **33**, 2320-2322 (2008).

[11] F. Schrempel, T. Gischkat, H. Hartung, T. Hoche, E. B. Kley, A. Tunnermann, and W. Wesch, "Ultrathin membranes in x-cut lithium niobate," Optics Letters **34**, 1426-1428 (2009).

[12] H. Hartung, E. B. Kley, T. Gischkat, F. Schrempel, W. Wesch, and A. Tunnermann, "Ultrathin high index contrast photonic crystal slabs in lithium niobate," Optical Materials **33**, 19-21 (2010).

[13] R. Geiss, S. Diziain, R. Iliew, C. Etrich, H. Hartung, N. Janunts, F. Schrempel, F. Lederer, T. Pertsch, and E. B. Kley, "Light propagation in

a free-standing lithium niobate photonic crystal waveguide," Applied Physics Letters **97**, 131109 (2010).

[14] T.-J. Wang, Y.-H. Tsou, W.-C. Chang, and H. Niu, "Fabrication of three-dimensional crystalline microstructures by selective ion implantation and chemical etching," Applied Physics A **102**, 463-467 (2011).

[15] T.-J. Wang, J.-Y. He, C.-A. Lee, and H. Niu, "High-quality $LiNbO_3$ microdisk resonators by undercut etching and surface tension reshaping," Optics Express **20**, 28119-28124 (2012).

[16] G. Y. Si, E. J. Teo, A. A. Bettiol, J. H. Teng, and A. J. Danner, "Suspended slab and photonic crystal waveguides in lithium niobate," Journal of Vacuum Science and Technology B **28**, 316-320 (2010).

[17] http://www.srim.org/

[18] J. Ehrenberg, R. Behrisch, and B. M. U. Scherzer, "Gas re-emission and surface structure due to implantation of helium in nickel," Nuclear Instruments and Methods in Physics Research **194**, 501-504 (1982).

[19] S. K. Erents and G. M. McCracken, "Blistering of molybdenum under helium ion bombardment," Radiation Effects **18**, 191-198 (1973).

[20] R. Ferrini, B. Lombardet, B. Wild, R. Houdre, and G. H. Duan, "Hole depth- and shape-induced radiation losses in two-dimensional photonic crystals," Applied Physics Letters **82**, 1009-1011 (2003).

[21] S. C. Hagness, D. Rafizadeh, S. T. Ho, and A. Taflove, "FDTD microcavity simulations: design and experimental realization of waveguide-coupled single-mode ring and whispering-gallery-mode disk resonators," Journal of Lightwave Technology **15**, 2154-2165 (1997).

Chapter 4 Fano resonances of free-standing $LiNbO_3$ PhC slabs

4.1 Introduction

Based on the ability to fabricate suspended structures in $LiNbO_3$ which was presented in Chapter 3, PhC slabs can be realized in bulk $LiNbO_3$ substrates. Such PhC slabs should have a vertical sidewall profile and show some interesting features. This Chapter presents detailed investigations of free-standing monolithic $LiNbO_3$ PhC slabs. Firstly a brief introduction of PhCs and guided resonances is given. Then a numerical analysis of Fano resonances in such slabs is demonstrated and the effects of slab thickness, of lattice types, of radius of air holes and of polarizations on optical properties are studied in order to give guidance in the design of PhC slabs in $LiNbO_3$. Furthermore, the fabrication results and the optical measurements of such slabs with different dimensions are presented.

4.1.1 Photonic crystals

PhCs are a type of artificial structure in which the dielectric permittivity (ε_r) and refractive index (n) change periodically in one or more dimensions. PhCs were originally proposed by Yablonovitch [1] and have received considerable attention because of their well-known band gap, enabling us to control the propagation of light. Similar to the energy band gap in semiconductors, a PBG refers to the fact that in the dispersion relationship there is a region in which the propagation of optical waves of certain

frequencies is forbidden. The reason why the band gap exists can be explained as follows: When optical waves pass through a PhC, the transmitted waves can interfere coherently with reflected waves. Consequently, waves with certain frequencies are completely reflected and not allowed to propagate through the PhC in every direction.

Depending on the directions of index modulation, there are three kinds of PhCs: one-, two- and three-dimensional PhCs. A most common example of a one dimensional PhC is a distributed Bragg reflector (DBR), which is already used as a high reflectivity mirror in vertical-cavity surface-emitting lasers (VCSELs). DBRs contain alternating layers of two different dielectric materials. However, DBRs require lots of layers of dielectric films to achieve a high reflectivity, which is not desirable for compact integrated devices. Three dimensional PhCs can have a complete band gap, which confine light in all directions. However, the fabrication of such complicated structures is still quite challenging [2].

Compared with 3D PhCs, 2D PhC slabs have been widely studied and developed because of their relatively simple fabrication processes and device integration techniques [3-5]. A 2D PhC slab consists of a 2D PhC fabricated in a high index guiding layer with a thickness on the order of the wavelength. A 2D PhC slab is a three dimensional structure, and the periodic refractive index modulation exists only in two directions along the slab, as shown in Fig. 4.1. 2D PhC slabs can provide optical confinement in both lateral and vertical directions. The light propagating in a slab is confined by Total Internal Reflection (TIR) in the vertical direction because of the index contrast between the slab and environment. In the in-plane direction the light is confined by the PhC lattice. This hybrid confinement allows 2D PhC slabs to

retain many of the important properties of 3-D PhCs. The restriction of a slab to a finite thickness gives rise to a significant difference in the band diagram compared with fully 2D PhCs of infinite height, as shown in Fig. 4.2. The most important feature of the band diagram of PhC slabs is the "light cone". The region in the light cone corresponds to radiation modes, of which light inside the slab can be coupled to external surroundings, leading to a radiation loss. Below the light cone they are discrete bands which correspond to guided modes. The light of guided modes is confined in the plane of the slab with nominally infinite lifetime and decays exponentially into the external surroundings [6]. It is noticed that there is not a complete band gap for a PhC slab. The band gap below the light cone indicates that light with a frequency inside the band gap cannot propagate in the plane of the slab but still can radiate into the external surroundings.

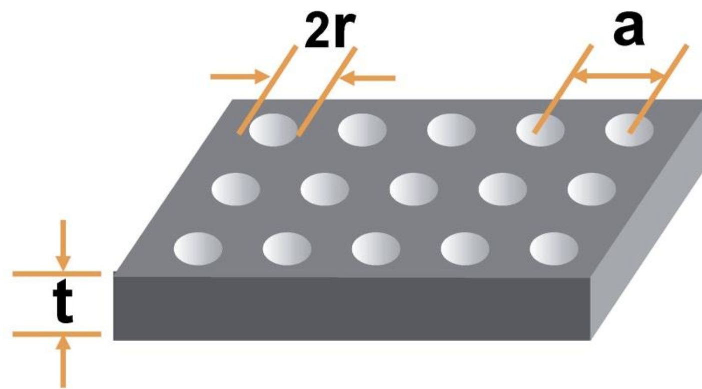

Figure 4.1: 2D PhC slab patterned by square lattice of holes in a dielectric slab with radius of air holes (*r*), lattice constant (*a*) and slab thickness (*t*) indicated.

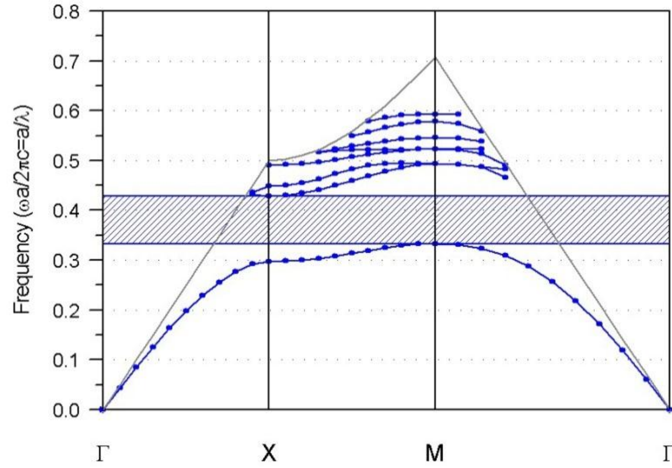

Figure 4.2: Band diagram of a typical 2D PhC slab.

4.1.2 Guided resonances – Fano resonances in PhC slabs

In a uniform slab without any pattern, the guided modes are completely confined inside the slab and cannot couple to the radiation modes. In a PhC slab, due to the Bragg scattering provided by the periodic index contrast, the guided modes in the band diagram are folded into the first Brillouin zone [7]. This folding in the band diagram brings modes above the light line, allowing them to couple to the radiation modes with a finite lifetime. These modes are called "guided resonances" [8]. They are a type of Fano resonance in PhC slabs.

The Fano resonance describes an interference phenomenon between a discrete energy state and a continuum of states. This kind of resonance has been discussed in a variety of physical systems like neutron scattering [9], microwave cavities [10], and plasmonic nanocavities [11]. One of main features of a Fano resonance is the asymmetric line shape in its spectrum. Fig. 4.3 (a) shows the schematic of a PhC slab under free-space illumination. Fano resonant peaks occur in the transmission and reflectance spectrum.

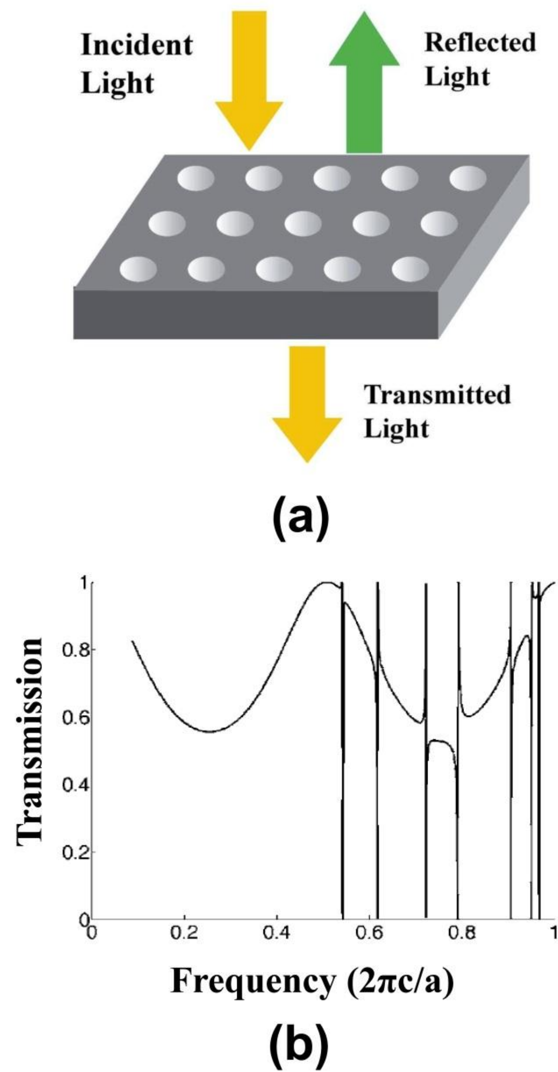

Figure 4.3: (a) Schematic of a PhC slab with square lattice of air holes under free-space illumination. Fano resonant peaks occur in the transmission and reflectance spectrum; (b) A simulated transmission spectrum of PhC slab under free-space illumination, which exhibits a sharp asymmetric shape due to the Fano resonance [7].

When a uniform dielectric slab without PhC structure is characterized, the transmission and reflection spectra are similar to Fabry-Perot oscillation. In PhC slabs, the guided modes that are folded back into the light cone act as the discrete state and the radiation modes represent the continuum state. The guided resonances in 2D PhC slabs have been theoretically investigated in [12]-[15]. When light is incident on a PhC slab with a normal-incident angle,

there are two pathways in the transmission process. One portion of the incident beam passes straight through the slab. The remaining portion of the incident beam excites the guided resonance. So the transmission spectrum is determined by the two pathways and contains typical narrow Fano line shapes superimposed on a Fabry-Perot background, as shown in Fig. 4.3 (b). The frequency and lifetime of guided resonances are determined by the dimensions of the PhC slabs.

This property of guided resonances provides a flexible method to design devices with different functions. In addition, the symmetry property of guided resonant modes also influences the coupling of these modes to external radiation modes. There are two classes of translational symmetry of the guided modes in the PhC slabs: singly degenerate modes and doubly degenerate modes. As reported in ref. [8], only doubly degenerate mode can couple with radiation modes.

4.1.3 Literature review of guided resonances

Guided resonances were firstly investigated in grating-incorporated dielectric thin-film structures [16-18]. Recently guided resonances based on 2D PhC slabs have attracted growing interest. Guided resonances in a variety of material systems were investigated, including Si, SiN and GaAs.

In 2004 Lousse *et al.* fabricated a suspended PhC structure in a silicon slab (thickness = 340 nm) and the angular dependence of the transmission property was investigated [19]. A high reflection was obtained over a wide angular range. In order to achieve polarization control, they proposed using rectangular holes instead of circular holes which were commonly used in most previous studies to reduce the rotational symmetry, as shown in Fig. 4.4. By

using rectangle holes, the simulation results suggested that there were differences in the transmission spectra among different polarizations of incident light. However, the idea proposed by the authors was difficult to realize in a fabrication process because such rectangular holes with dimensions at the nanometer scale usually became circularly shaped after etching.

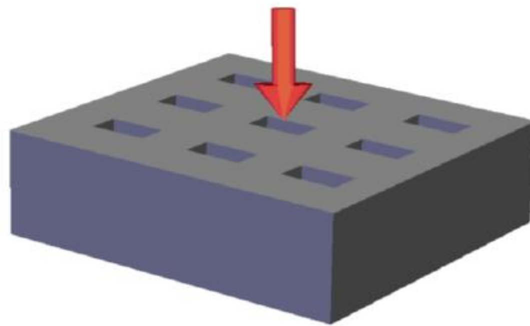

Figure 4.4: PhC slab structure with rectangular air holes in order to achieve polarization control on transmission spectrum [19].

Besides silicon, guided resonances were also realized in other materials and showed important applications. In 2012, Bui *et al.* fabricated PhCs in a commercial ultrathin SiNx membrane with a thickness of 50 nm [20]. The commerical SiNx membrane was an important component used in optomechanics systems due to its high mechanical Q factor. However there was a challenge that such membrane showed a low reflectivity which limited its applications. By employing PhCs in the membrane, they demonstrated a good enhancement of reflectivity of such membrane due to guided resonances. Their SiN_x PhC slab showed a great potential to be applied in optomechanics systems.

Symmetrical PhC slabs like free-standing membranes can provide a large index contrast on both sides of a slab; however, such suspended structures are

very fragile and easy to break. To solve this problem, asymmetrical PhC slabs have been proposed and investigated. Such an asymmetrical PhC slab is normally in contact with a substrate, which provides structural support for a thin film. To demonstrate the possibility of guided resonances in asymmetrical PhC slabs, in 2005 Rosenberg *et al.* fabricated a Fano resonance filter by milling holes in a GaN film on a sapphire substrate [21]. Two resonant modes were observed in the visible spectrum and the measured Q factor (200) in the asymmetrical PhC slab was comparable to similar resonances in symmetrical counterparts. This study provided clear evidence that guided resonances can still persist in an asymmetrical slab in spite of high radiative loss.

Interesting features in the asymmetrical lineshape in their spectra make PhC slabs useful for many applications. A distinct feature of the guided resonance in a PhC slab is strong reflectivity over a wide range of frequencies, especially for resonances with short lifetimes. This feature allows PhC slabs to act as optical mirrors which are very important in many optical MEMS devices. A PhC slab mirror can consist of only a single dielectric layer, which is more compact vertically than traditional mirrors made by dielectric stacks. For example, Kim *et al.* fabricated a PhC slab mirror by patterning air holes on a free-standing polysilicon membrane [22]. In order to reduce the compressive stress of the polysilicon membrane and obtain a flat mirror a tensile stressed silicon nitride layer was deposited on top of the polysilicon membrane to mitigate the compressive stress. A reflectivity more than 90% from 1565 nm to 1600 nm was achieved.

Following this work, a PhC mirror of 400 nm thickness was used in a MEMS application as a single-axis high reflectivity scanner actuated by in-chip plane electrostatic combdrives [23]. A total scan angle up to 120° was

achieved at a resonance frequency of 2.03 KHz. Such a PhC slab scanner showed low angular and polarization dependence, which are both important characteristics for use in scanners. However, a major drawback of this approach is that the working wavelength range of such a PhC scanner is fixed (reflectivity of > 95% in the wavelength range from 1380 to 1450 nm). Consequently, such a scanner cannot be tuned to a desired wavelength depending on different applications. The only way to change the reflectance spectrum is to vary the design parameters of the PhC slab, like the lattice constant, the hole radius and the slab thickness. The lack of tunability of such a PhC scanner can be solved by using $LiNbO_3$

Due to the unique properties of guided resonances in PhC slabs, some researchers explored a variety of innovative methods of employing such PhC slabs into flexible applications. For example, by using two PhC slabs as mirrors to form an optical cavity, a strong variation of transmission spectra was achieved with only a nano-scale displacement variation between slabs [24]. Such optical cavity can be used as an extremely compact displacement sensor with high sensitivity, which may play an important role in MEMS devices.

Besides mirrors, filters also can be constructed using PhC slabs. Zhou *et al.* demonstrated a type of Fano filter based on a single crystalline Si nano-membrane of 260 nm thickness transferred onto a polyethylene terephthalate (PET) substrate, as showed in Fig. 4.5 [25]. A dominant dip was observed at a wavelength of 1547 nm in the transmission spectra. In addition, this kind of filter showed unique bending properties because of the use of flexible PET substrates. There was a blue shift of wavelength in the transmission spectra at different bending conditions. However, such a

nano-mambrane transfer requires complicated processes and several hours to release the top Si membrane.

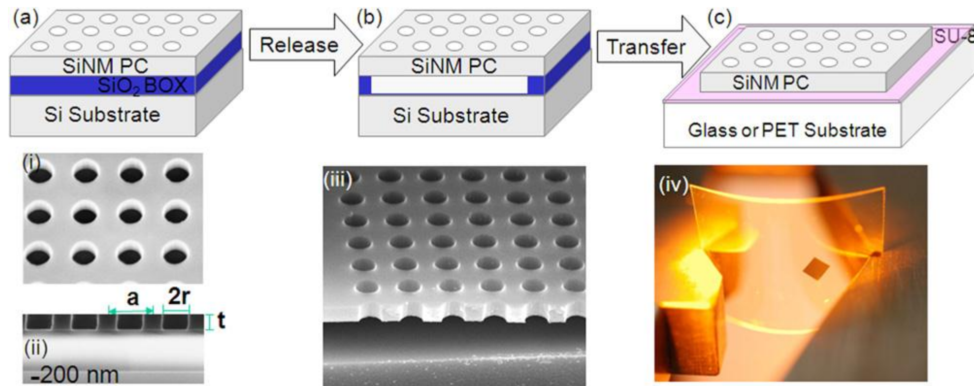

Figure 4.5: Fabrication process for PhC slabs transferred on PET substrate. (a) Single layer PhC pattern; (b) Release; (c) Transfer; (i) SEM image of top and (ii) side view of patterned Si PhC slabs on SOI substrate; (iii) SEM image of patterned Si PhC slab after removing the oxidation layer; (iv) a micrograph of a 3 × 3 mm patterned Si PhC slab transferred onto 1 inch × 1 inch flexible PET substrate [25].

4.1.4 Motivation of investigating guided resonances of free-standing $LiNbO_3$ PhC slabs

Based on the above review, it is clear that the 2D PhC slab is a preferred choice to fabricate PICs due to its compact size and flexible functions. However, so far devices based on 2D PhC slabs have been mainly fabricated in Si and Si_3N_4 membranes, which show low or nonexistent EO coefficients and/or slow response speeds (Si shows no Pockels effect, so index can be modulated only through other mechanisms such as thermal or carrier-induced index changes). Consequently it is worthwhile to employ 2D PhC slabs in $LiNbO_3$ substrates and examine its properties for further practical applications. The advantages of employing PhC slabs into $LiNbO_3$ are the following:

1) Due to its ultrafast EO response, it would be an attractive prospect to

fabricate $LiNbO_3$ EO tunable PhC devices of small size, which can provide more flexible applications. For example, tunable spatial light modulators and filters based on $LiNbO_3$ would provide a promising solution for free space communications, and the material would offer much faster operation than traditional spatial light modulators. Such tunable filters also can be used in wavelength division multiplexing (WDM) systems.

2) This incorporation of nonlinear materials into PhC slabs is important for enhancing nonlinear light-matter interaction in general, as this can be useful for future quantum information processing tasks and also in optical logic elements.
3) The birefringence property of $LiNbO_3$ can also provide a new platform for polarization selective applications. Since the Fano resonance is a characteristic feature of quantum interference [26], this incorporation can potentially open new opportunities for exploiting physical phenomena in quantum optics as well.

In remaining sections of this chapter we conduct a theoretical and experimental study of the guided resonance of free-standing $LiNbO_3$ PhC slabs. We first perform a detailed numerical analysis on the transmission characteristics by using the 3D FDTD (Finite-Difference Time-Domain) method. The effect of slab thickness, of radius of holes, and of lattice type on transmission properties is discussed. Next, the polarization effect of PhC slabs is analyzed. Then a monolithic approach to fabricate free-standing $LiNbO_3$ PhC slabs is presented. Finally free-space illumination measurements of the reflectance spectrum at normal incidence over a broadband wavelength are performed to analyse the optical properties of various fabricated PhC slabs.

4.2 Numerical modeling of $LiNbO_3$ PhC slabs

In the modeling, we consider a square lattice of air holes in a $LiNbO_3$ slab. As $LiNbO_3$ is a bifringent crystal with an ordinary (y-polarization) and extraordinary (z-polarization) refractive index, we first consider a simple case in which only the ordinary index (n_0) plays a role (n_0=2.227 at 1200 nm wavelength) for a specific polarization in the investigations of slab thickness, lattice type and radius dependence. Then both ordinary and extraordinary indices are considered in the investigation of polarization dependence.

In our modeling, the Finite-Difference Time-Domain (FDTD) method was used to analyse the transmission spectra of $LiNbO_3$ PhC slabs. The FDTD method is widely used as a propagation solution technique in many photonic devices. It directly solves Maxwell's equations by discretizing the equations via difference in time and space [27]. Consequently there are no approximations (other than discretization) and theoretical restrictions. In our case a software package Rsoft FullWAVE v6.1 was used to perform the 3D FDTD simulations. The material properties of $LiNbO_3$ were directly specified in FullWAVE material library.

Figure 4.6 shows an example of the side view of our simulation model. A simulation domain with two monitors is shown with purple lines. In order to save computational time and memory, we only choose a single unit cell in which to perform the simulation. The boundary conditions were set to be "Periodic" along the z and y axes and they can be mathematical expressed in Equation $(4-1)$. This configuration indicates the structure will be infinite along the z and y axes.

$$E(x_i) = E(x_i + \Delta)e^{ik_i x_i} \qquad (4-1)$$

Meanwhile, Perfectly Matched Layer (PML) boundary conditions were used at the x axis boundaries to absorb the transmitted light. One monitor (Monitor 1) was placed behind the slab to collect the transmitted power and another monitor (Monitor 2) was place behind the source to collect the reflected power. Because we used periodic boundary conditions in the z and y directions, a rectangle launch field profile was used to launch a Gaussian pulse with plane wave profile in spatial domain, and the size of source was wider than the simulation domain width.

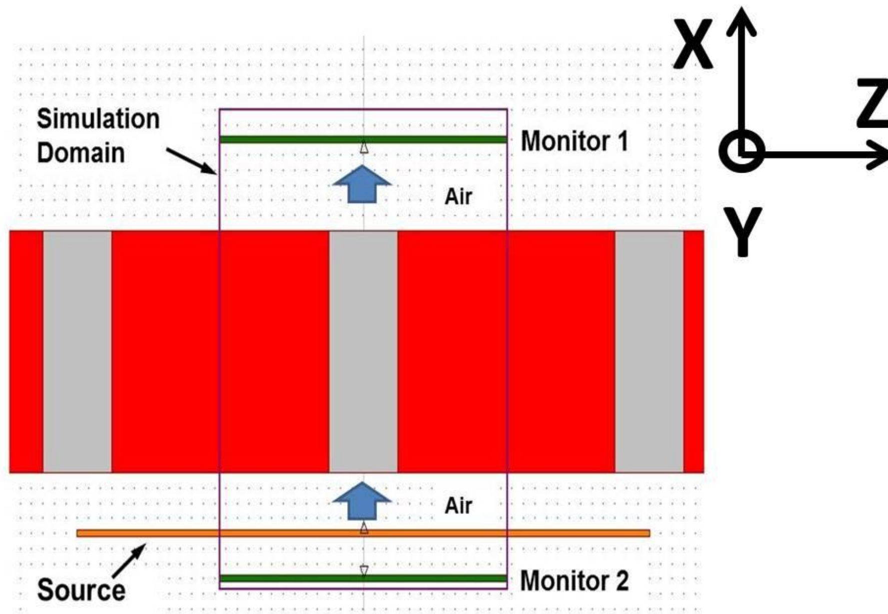

Figure 4.6: Side view of a 3D FDTD simulation layout. The entire simulation domain with two monitors is shown with purple lines. The top right of the layout shows the coordinate system.

Then a fast Fourier transform (FFT) of the time monitor output was performed to obtain the frequency response of the system. This allowed us to obtain the frequency spectrum with a single simulation run. In order to

improve the accuracy of the simulation results, a convergence study was performed and a 0.01 μm grid size was chosen, which was smaller than λ/10 = 0.12 μm at wavelength of 1200 nm (λ/10 is considerable to be a reasonably small grid spacing value to carry out an accurate simulation in the FDTD method). The parameters of the 3D FDTD setup are summarized in Table 4.1.

Table 4.1: 3D FDTD simulation parameter setup for 2D PhC $LiNbO_3$ slab.

Category	Parameters	Value
Global	Grid size	0.01 μm
	Time step	Grid size / 2
	Stop time	2^16 × time step
Source	Source temporal type	Gaussian
	Size of source	2×lattice constant in X and Y direction
	Source location	Center at (0,0.0.3)
Monitors	Monitor 1 (transmission) size	lattice constant
	Monitor 1 (transmission) location	Center at (0,0,0.6 + Slab Thickness)
	Monitor 2 (reflection) size	lattice constant
	Monitor 2 (reflection) location	Center at (0,0,0)
Boundary Conditions	Z direction	PML
	X and Y direction	Periodic

4.2.1 The effect of slab thickness on transmission properties

As discussed in Chapter 3, the energies of implanted ions can be adjusted to achieve a suspended slab with desirable thickness. Consequently it is worthwhile to study how Fano resonant modes change with slab thickness. Fig. 4.7 shows the simulated transmission spectra at normal incidence for $LiNbO_3$

PhC slabs with thicknesses 300 nm, 700 nm and 1.5 µm. The lattice constant (a) and radius (r) of holes are kept at a = 900 nm and a ratio of r/a = 0.28. In Fig. 4.7, when the slab thickness increases, the Fabry-Perot oscillation background becomes more obvious in the infrared region, indicating increased Fabry-Perot interference inside the slab.

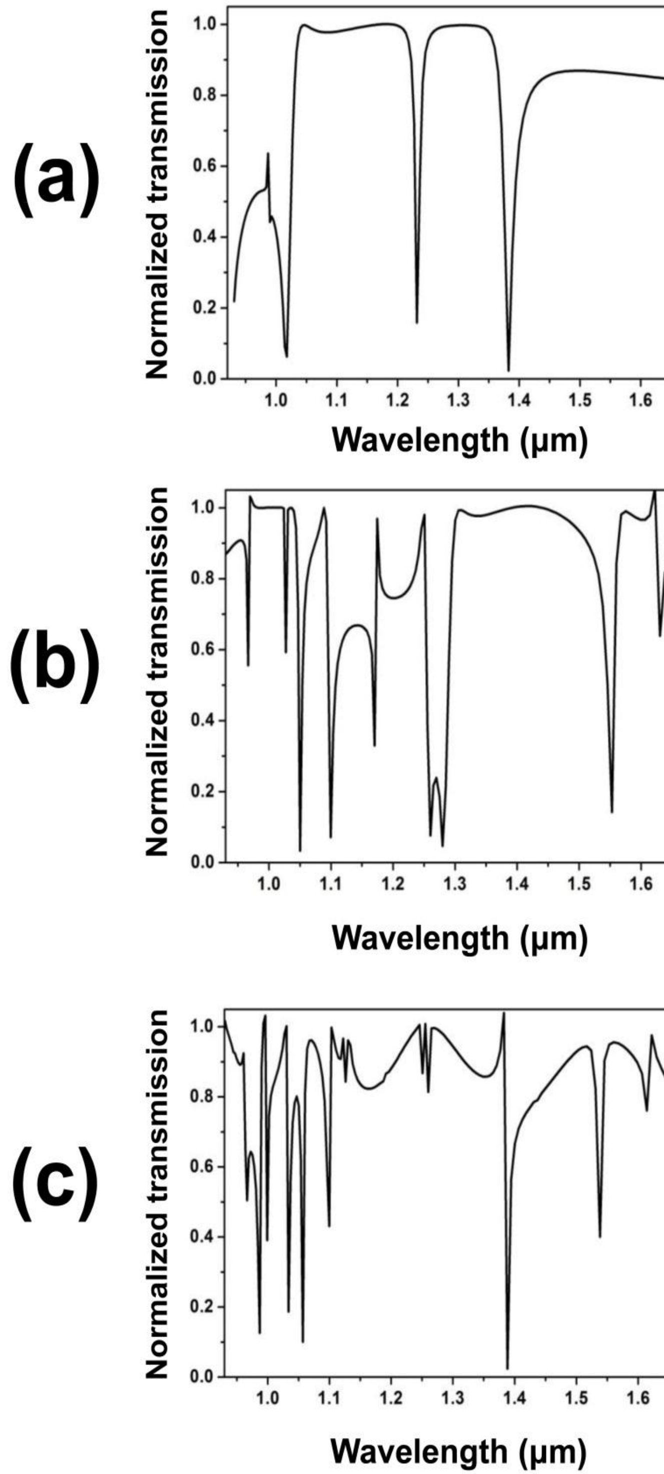

Figure 4.7: Simulated normal-incident transmission spectra of PhC slabs with various slab thicknesses (a) 300 nm; (b) 700 nm; (c) 1500 nm. The lattice constant (a) and radius (r) of holes keep the same value: $a = 900$ nm and a ratio of $r/a = 0.28$.

Fig. 4.7 (a) shows the transmission spectrum of a slab of 300 nm

thickness with two sharp Fano resonant peaks in the wavelength range of 1200 nm to 1400 nm. When the slab thickness increases, a stronger Fano resonance occurs, leading to a larger number of modes, as shown in Figs. 4.7 (b) and (c). As the slab thickness decreases, the resonance moves to a slightly shorter wavelength. It has been reported in [28] that decreasing a slab thickness leads to an increase of the delayed length of the resonance, lowering the effective index. Note that it is worthwhile to analyze the slab thickness dependence because the fabrication method presented in this work allows tunability of slab thickness by changing ion implantation energy. This method provides an effective way to design the functionality of the PhC slabs for different applications such as filters and sensors. For example, a tunable filter working in the mid-infrared region can be created by choosing a large slab thickness which leads to guided resonance modes with lower frequencies.

4.2.2 The effect of lattice types on transmission properties

Different types of lattices (square lattice or triangular lattice) will also affect the transmission properties of PhC slabs. In this section we study how the transmission spectra of PhC slabs change with lattice type. Fig. 4.8 plots the transmission spectra for triangular and square lattices. We choose two groups of structural parameters for square and triangular lattices: one has slab thickness t = 800 nm, r = 80 nm and periodicity a = 800 nm (Fig. 4.8 (a)), and the other has slab thickness t=800 nm, r = 250 nm and periodicity a = 800 nm (Fig. 4.8 (b)). It is similar to the calculation domain of the square lattice except for the unit cell geometry. The main difference between a triangular lattice and square lattice is the air hole filling factor. The air hole filling factor of the triangular lattice is higher than that of the square lattice.

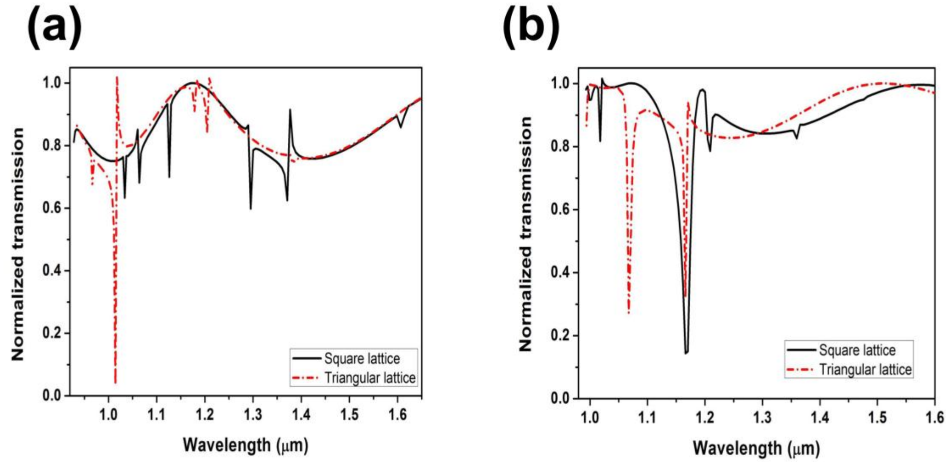

Figure 4.8: Comparison of simulated transmission spectra of PhC slabs for different lattice types. The transmission spectra of PhC slabs with a square lattice are shown with solid lines, while transmission spectra of PhC slabs with a triangular lattice are shown with dashed lines. (a) The structure consists of a slab thickness t = 800 nm, lattice constant a = 800 nm and the ratio of r/a = 0.1; (b) The structure consists of a slab thickness t = 800 nm, lattice constant a =800nm and the ratio of r/a = 0.31.

It can be seen that with both groups of structural parameters, fewer resonance modes can be excited at near infrared wavelengths in the triangular lattice compared with the square lattice. In square lattices, as the operating wavelength increases, more spurious high order modes are generated. In addition the line shape of the triangular lattice shows sharp peaks, resulting in a higher Q factor than the square lattice. For example, we estimated the Q factor from the full-width at half-maximum in Fig. 4.8 (b). The calculated Q factor at resonance peak in the wavelength of 1166 nm is approximately 51 for the square lattice and 134 for the triangular lattice. By using the triangular lattice, the Q factor has been improved by 62%. Moreover, from Fig. 4.8 (a) it can be seen that there is a sharp resonance peak at a wavelength of 1014 nm with a Q factor of ~218 for a triangular lattice but no peak for the square lattice. These features of the triangular lattice make it more suitable for optical

switches and modulators due to the lower number of resonance peaks within a certain wavelength range.

4.2.3 The effect of radius of air holes on transmission properties

The dimensions of the PhCs like radius of air holes will influence the transmission properties of PhC slabs significantly. In addition, the designed radii of air holes may be altered after many fabrication steps. Consequently it is worthwhile to study the effect of radius of air holes. To demonstrate this, we plot the transmission spectra with ratio r/a varying from 0.1 to 0.31, as shown in Fig. 4.9 (a)-(d). The other parameters are identical (a triangular lattice with slab thickness t=800 nm). From Fig. 4.9 we can see that as the radius increases, more Fano resonances are generated and a smooth Fabry-Perot oscillation feature splits into more sharp peaks. Compared with Fig. 4.9 (a), four more Fano resonance peaks are generated in the wavelength range 900 nm to 1200 nm in Fig. 4.9 (d). Note that the resonance modes have a blue shift as the radius increases. For example, in Fig. 4.9 (a) it can be seen that there is a resonance peak at the wavelength of ~1020 nm (highlighted with an arrow). As the radius increases, the wavelength of this peak shifts to the region of ~850 nm. Furthermore, it is evident that a decrease in the radius leads to the line shape becoming sharper, resulting in a higher Q factor. For the resonance with the arrow in Fig. 4.9 (a)-(d), the Q factor varies from approximately 218 at r/a = 0.1, to 78 at r/a = 0.31.The reason why the Q factor decreases as the radius of holes increases is that strong in-plane scattering happens in the slab with a large hole radius, resulting in a short photon lifetime. Consequently one can realize filters with a very high Q factor by simply decreasing the radius of air holes. Note that to realize a filter, the slab thickness must be comparable to

the wavelengths of interest in order to minimize the density of resonant modes [21]. Without the coupling of nearby modes, a high Q factor can be obtained to meet the requirement of a filter. On the other hand, a broadband reflector with high reflectivity could be realized by enlarging the radius of air holes, as reported in [22].

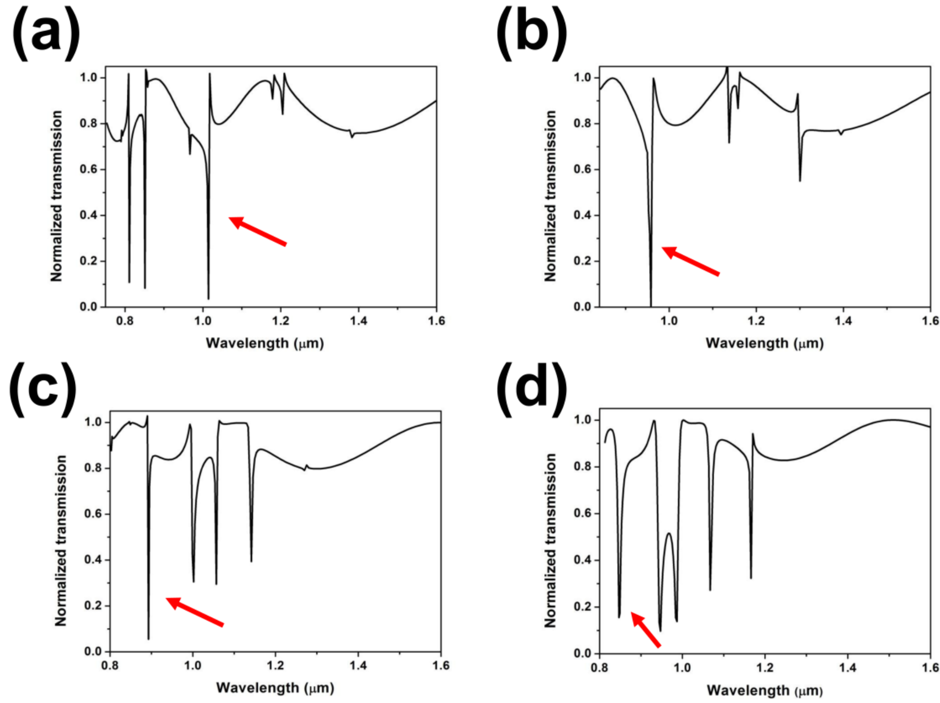

Figure 4.9: Comparison of simulated transmission spectra of triangular lattice PhC slabs with a radius of (a) $r / a = 0.1$; (b) $r / a = 0.153$; (c) $r / a = 0.26$; (d) $r / a = 0.31$. The lattice constant (a) and slab thickness (t) are kept at: a =800 nm, t =800 nm.

4.2.4 The effect of polarization of incident light on transmission properties

In Si and other common materials, due to rotational symmetry at normal incidence, the transmission spectra would be independent of polarization. However, an x-cut $LiNbO_3$ crystal, which has negative uniaxial anisotropy, does not show rotational symmetry at normal incidence. In addition, when the rotational symmetry of the structure is reduced in $LiNbO_3$, many unique

polarization dependent devices can be created. Consequently, it is worthwhile to study the polarization dependence of $LiNbO_3$ PhC slabs.

In $LiNbO_3$, the birefringence creates an index difference between y-polarized and z-polarized light of 0.0762 at a 1064 nm wavelength [29]. In the coordinate system of the crystal slab, light polarized in the y direction (y-polarized) will see the ordinary refractive index while light polarized in the z direction (z-polarized) will see the extraordinary refractive index. In calculation we use the ordinary index (n_o=2.227) for y-polarized light modeling and extraordinary index (n_e=2.149) for z-polarized light modeling.

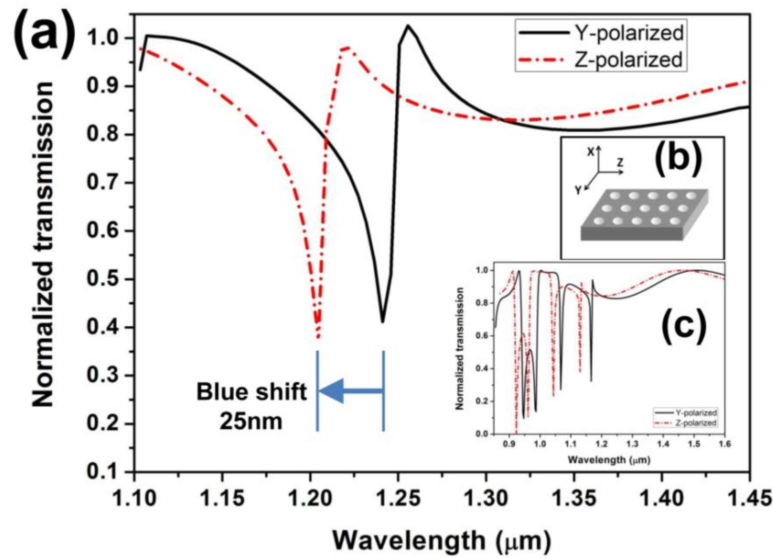

Figure 4.10: (a) Comparison of simulated transmission spectra of polarized light normally incident on a $LiNbO_3$ PhC slab. The transmission spectra of y-polarized light are shown with solid lines, while the transmission spectra of z-polarized light are shown with dashed lines. The structure consists of a square lattice with a slab thickness *t* of 800 nm, a lattice constant *a* of 800 nm, and a radius *r* of 150 nm. The inset (b) shows the coordinate system of the slab. The inset (c) also shows the comparison of simulated transmission spectra of polarized light on a different structure, which consists of a triangular lattice with a slab thickness *t* of 800 nm, a lattice constant *a* of 800 nm, and a radius *r* of 250 nm.

Figure 4.10 (a) shows a comparison of the transmission spectra of polarized light normally incident on a $LiNbO_3$ PhC slab. The structure we simulated consists of a square lattice with a slab thickness *t* of 800 nm, a lattice constant *a* of 800 nm, and a radius *r* of 150 nm. The coordinate system of the slab is shown in Fig. 4.10 (b). A significant shift (~25 nm) for different polarizations can be observed in Fig. 4.10 (a). A resonant mode at around the 1250 nm wavelength range is observed for y-polarized light while nearly 100% transmission is observed for z-polarized light. It is concluded that y-polarized light will lead to more resonance modes than z-polarized light. This is also in agreement with [30] that lowering the slab refractive index will reduce the number of modes in a PhC slab generally. This is predicted by the empty lattice approximation.

In order to confirm the phenomenon of polarization dependence in $LiNbO_3$ PhC slabs, we simulated another structure with different parameters (a triangular lattice with slab thickness of 800 nm, lattice constant of 800 nm and radius of 250 nm), as shown in Fig. 4.10 (c). The result also shows good correspondence with the previous one. This unique property of $LiNbO_3$ PhC slabs has many potential applications such as polarization selective filters.

4.2.5 The effect of asymmetrical structures on transmission properties

In previous sections we considered the case of symmetrical PhC slabs. The slabs were assumed to be free-standing membranes surrounded by infinite air regions. However, as we showed in Chapter 3, the structures fabricated by ion implantation and wet etching are suspended above $LiNbO_3$ substrates.

In order to investigate the effect of the substrates, in this section we study

a structure consisting of periodic air holes that are patterned on a $LiNbO_3$ membrane and suspended a certain distance above a $LiNbO_3$ substrate, as shown in Fig. 4.11, which is a more realistic model.

The comparison of the transmission spectra between a free standing membrane and a slab over a substrate with only a 200 nm air gap is shown in Fig. 4.12. The small air gap between the membrane and substrate weakens the Fano line shape significantly, resulting in a smooth oscillation. It may be due to the fact that the guided resonance confined within the slab leaks into the $LiNbO_3$ substrate causing short life time for these modes. This effect could be avoided in the fabrication process by using multi energy implantations to increase the air gap thickness.

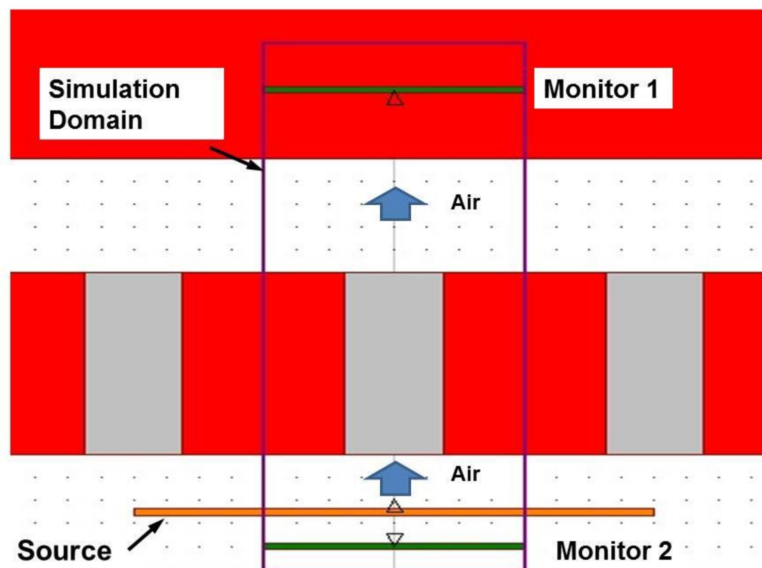

Figure 4.11: Side view of 3D FDTD simulation layout for the asymmetrical structure in a $LiNbO_3$ PhC slab.

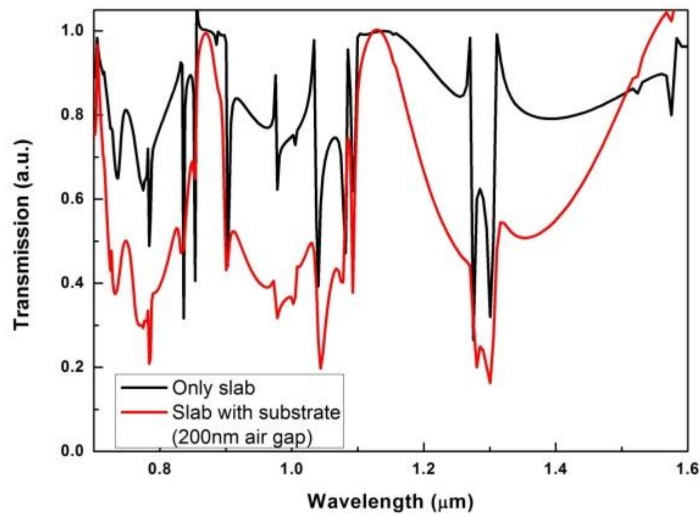

Figure 4.12: Comparison of the transmission spectra between a free standing membrane and a slab over a substrate with only a 200 nm air gap.

4.3 Fabrication of free-standing $LiNbO_3$ PhC slabs

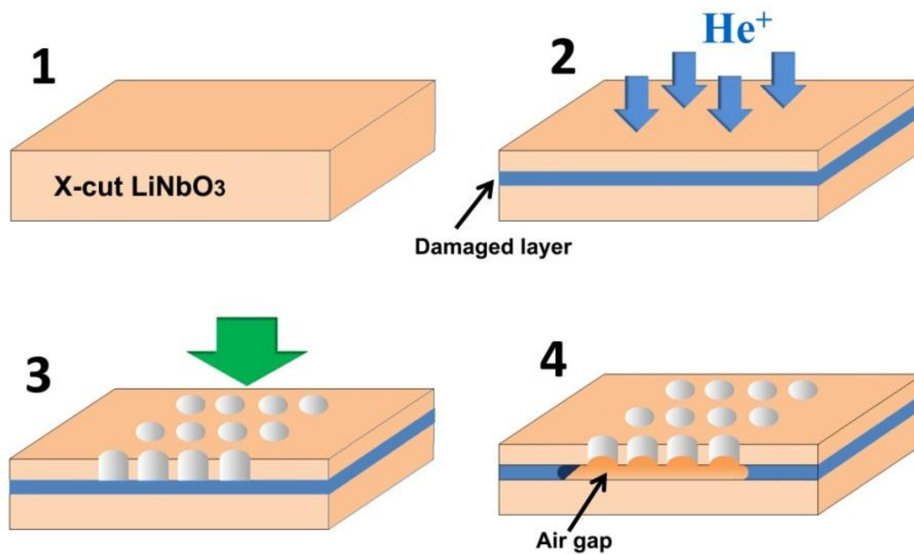

Figure 4.13: Fabrication process of free-standing PhC Slabs. 1. The x-cut $LiNbO_3$ wafer; 2. He implantation with multi-energy; 3. Focused ion beam milling to pattern PhCs; 4. Wet etching by immersing the wafer into acid. The acid reaches the damaged layer through the air holes to form the suspended PhC slabs.

The fabrication steps are shown in Fig. 4.13. The $LiNbO_3$ samples used in our experiments were x-cut with two sides polished. Firstly, He^+ ions with different beam energies over an area of 1 cm×1 cm were implanted on the surface of bulk $LiNbO_3$ samples. Then the PhCs were patterned as square arrays of air holes on the implanted samples with a FIB. The beam current used in our experiment was 100 pA and the acceleration voltage was 30 KV. Before milling, a 20 nm Au layer was evaporated on top of the $LiNbO_3$ substrate in order to avoid charging effects. In order to complete wet etching step, the air holes were milled thicker than the slab. In our case, approximately 1.5 μm etch was sufficient to remove the damaged layer. After that, wet etching was performed by immersing samples into an acid (65% HNO_3 : 49% HF =2:1). Acid will go through the air holes patterned by FIB and reach the damaged layer. A very high etching rate of the damaged layer (~100 nm/min) can be obtained. Compared with the damaged layer, the top layer with lower damage shows a very low etching rate which can be neglected. Consequently after wet etching the suspended structures with air gap were formed. To confirm whether the damaged layer has been removed completely, we added trench on one of fabricated structures, as shown in Fig. 4.14. It can be seen that the fabricated PhC slab is fully undercut and the sidewalls of etched holes are smooth and vertical. Au particles remaining on the surface of $LiNbO_3$ substrate are also obvious.

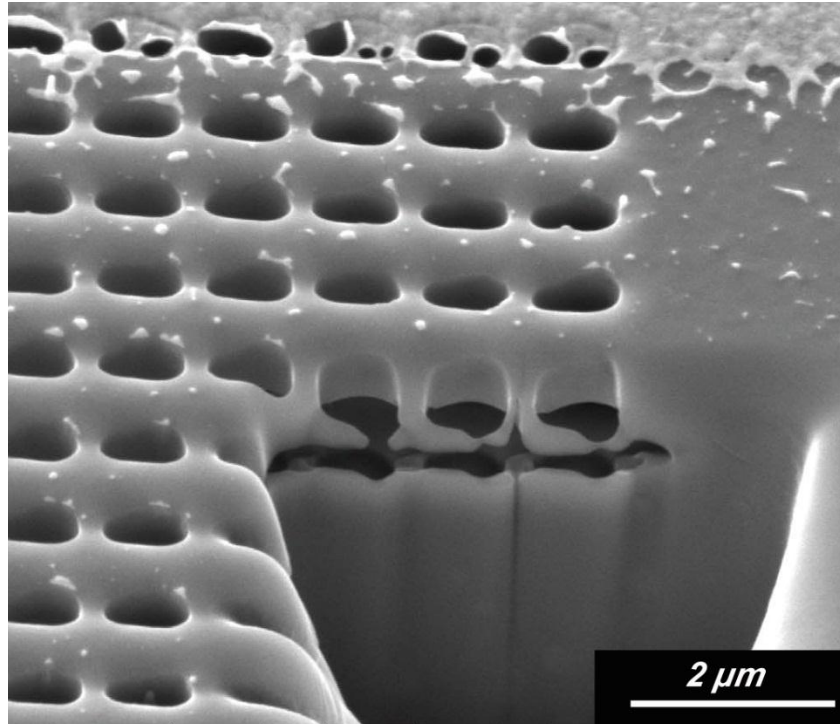

Figure 4.14: SEM image showing a cross section of free-standing PhC slabs. An air gap formed by wet etching is clearly visible.

We successfully fabricated free-standing $LiNbO_3$ PhC slabs with different radii of air holes and slab thicknesses. Fig. 4.15 shows two examples of fabricated PhC slabs. In Fig. 4.15 (a) and (b), the structure consists of a 750 nm thick slab patterned with a square lattice of air holes. The PhC consists of a lattice constant a = 800 nm and r/a = 0.308. The air gap between the slab and $LiNbO_3$ substrate is approximately 500 nm. In Fig. 4.15 (c) and (d), the structure consists of a 800 nm thick slab patterned with a square lattice of air holes. The PhC consists of a lattice constant a = 1000 nm and r/a = 0.15. The air gap between the slab and $LiNbO_3$ substrate is approximately 250 nm.

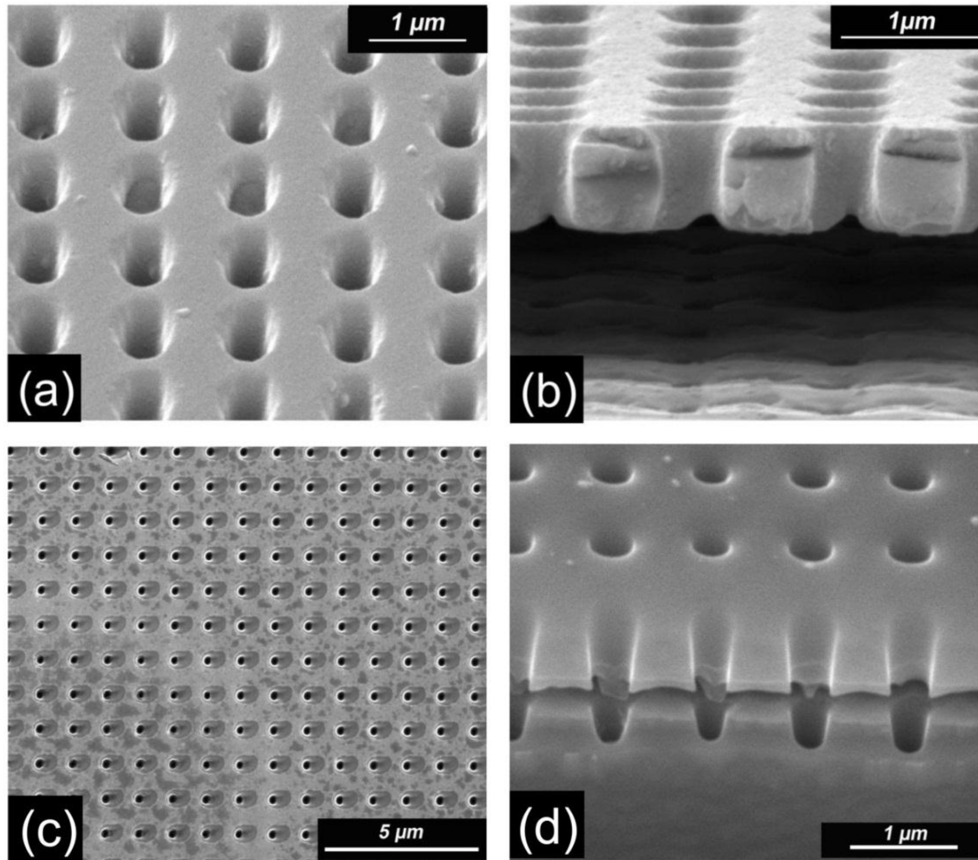

Figure 4.15: SEM images of the fabricated free-standing PhC slabs in $LiNbO_3$. 1. Square lattice with lattice constant a = 800 nm and r/a = 0.308 (a) view with a tilt angle of 45°; after wet etching the air holes become slightly elliptically shaped instead of circularly shaped; (b) Side view; 2. Square lattice with lattice constant a =1000 nm and radius of r/a = 0.15 (c) view with a tilt angle of 45°; (d) Side view.

It is worthwhile to point out that our procedure is different from the one described in ref. [31], which is usually used in fabrication processes. In their procedure a free-standing membrane was firstly fabricated, followed by patterning of PhCs and selective etching. In such etching of slabs, the etching proceeds laterally inwards from a vertical cutline along the damaged layer. However, the material close to the exposed area is attacked longer by the etchant than material further in. This causes a lateral wedge-shaped undercut etch, which can be seen in Fig. 4.16 (a); the undercut is not uniform laterally.

Additionally, a long etching time was required to form large area membrane. By contrast, in our procedure PhCs are firstly patterned. The air holes also serve as trenches which provide access for acid to etch the damaged layer. Consequently, a uniform suspended slab can be obtained, as shown in Fig 4.16 (b). In addition, because only small areas between holes in the damaged layer are required to be removed, large area PhC slabs can be fabricated within a short etching time.

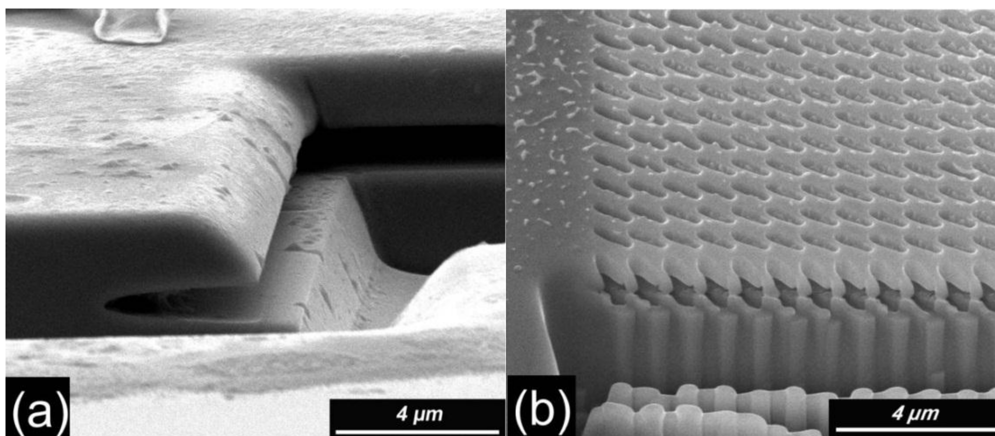

Figure 4.16: (a) Side view of the etching profile in a suspended membrane. The thickness of membrane is not uniform; (b) Side view of PhC slabs fabricated in our procedure. The uniform slab thickness is obvious.

4.4 Optical characterization

4.4.1 Measurement setup

Optical characterization of the suspended PhC slabs was performed using a UV-Visible-NIR microspectrophotometer (CRAIC Tech Ltd.). The measurement setup and principle of reflection measurement in the micro-spectrophotometer is shown in Fig. 4.17 (a) and (b). A lamp was used to generate a broadband light of wavelength range from about 800 nm to 2000 nm.

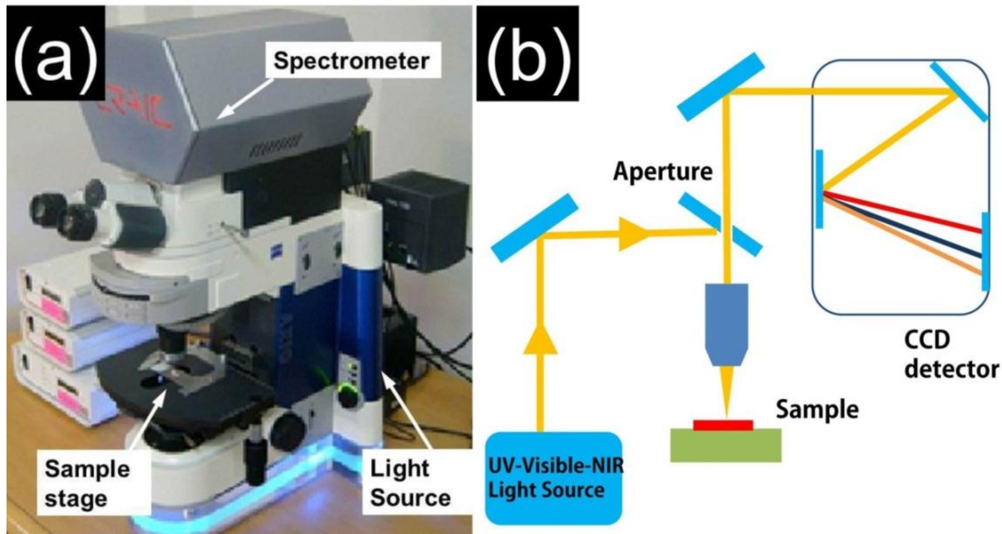

Figure 4.17: (a) microspectrophotometer; (b) Schematic for reflection measurement.

The reflected beam passed through a beam splitter and a mirrored aperture then was detected by a CCD detector. In our experiment a small aperture of 6 μm diameter was used to improve the measurement accuracy. Firstly a reference sample without any pattern was measured to make sure the spectrum is source independent. Then samples with PhC slabs were measured and final results are reflectance spectra relative to the reference.

4.4.2 Measurement results of free-standing $LiNbO_3$ PhC slabs with different dimensions

The measured reflectivity for normal incidence is plotted in Fig. 4.18 (the solid line). The reflectivity spectrum shows a smooth slope instead of a sharp peak because of the small air gap between the membrane and substrate. FDTD simulation was performed to compare with the measured data (the dashed line in Fig. 4.18). The structural parameters for simulation were estimated from the SEM image (Figs. 4.15 (c) and (d)) after fabrication, which consist of a square lattice of air holes with a lattice constant a =1000 nm and r/a = 0.15, a slab

thickness t = 800 nm and an air gap g = 250 nm above the substrate.

In the experiment an x-cut sample and an un-polarized light source were used. Consequently we calculated the reflection spectrum by using the ordinary and extraordinary indices for the same structure respectively and averaging the spectra. From Fig. 4.18 it can be seen that the calculated spectrum agrees well with the measured one. Because the spectra shift for different indices, it seems the guided resonance peaks are "smoothed" and broadened in the average spectrum. In addition, two Fano resonance peaks can be observed in the wavelength range 1400 nm to 1500 nm. It shows excellent agreement with the two wide dips in measured spectra.

In order to investigate the radius dependence of our PhC slabs, the reflection spectra of two PhC slabs which have the same initial design parameters except for the radius of air holes are measured and plotted in Fig. 4.19.

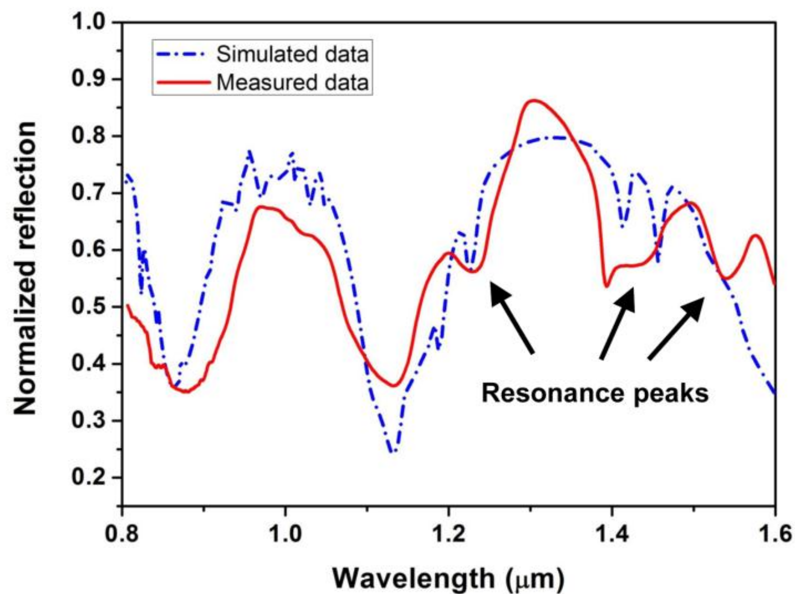

Figure 4.18: Reflection spectra of un-polarized light incident normally on a fabricated PhC slab. Red solid line—measured reflection spectra. Blue dashed line—simulated reflection spectra.

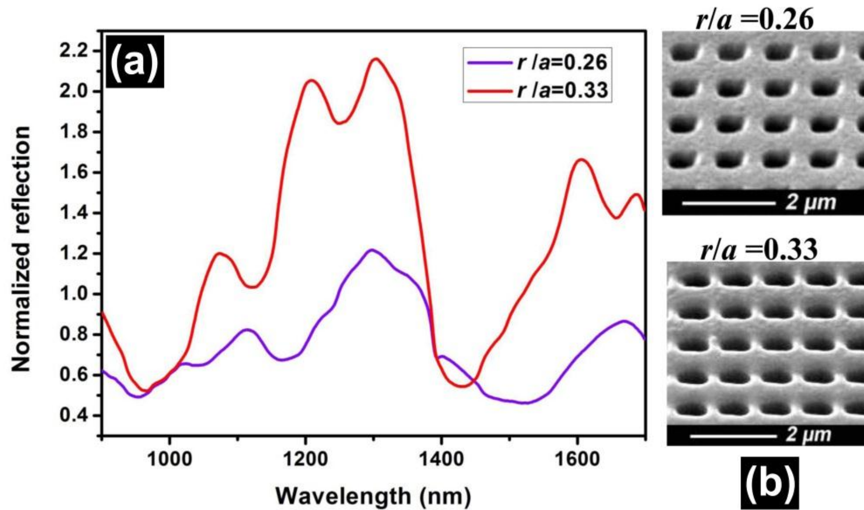

Figure 4.19: (a) Comparison of measured normal-incidence reflection spectrum of the fabricated PhC slabs with square array of holes with different radii: 260 nm and 330 nm.The lattice constant for both structures is the same: a =1000 nm; (b)SEM images of the two PhC slabs viewed with a tilted angle of 60°.

SEM images in Fig. 4.19 (b) show that both structures consist of a square lattice with a lattice constant a =1 μm, a slab thickness t =770 nm and an air gap g =520 nm above the substrate. After fabrication processing the average hole radii of the two structures are 260 nm and 330 nm, respectively. As predicted by simulations previously, the measured reflection spectra of the structure with a larger air hole radius shows more resonance peaks (three dips at λ=1130 nm, 1245 nm and 1660 nm, which are not obvious in spectra with r/a = 0.26). In addition, it can be seen that a slight shift in the spectra happens in Fig. 4.19 (a). This agrees with simulation results that the resonance modes have a blue shift as the radius increases.

Fig. 4.19 (a) also indicates that the overall reflectivity of the structure with r/a = 0.33 is higher than the one with r/a = 0.26. It should be noted that for the PhC slab with a larger radius, the reflectivity of the peak at the center of the spectrum is higher than 1 (the highest reflectivity is 2.1). It means that

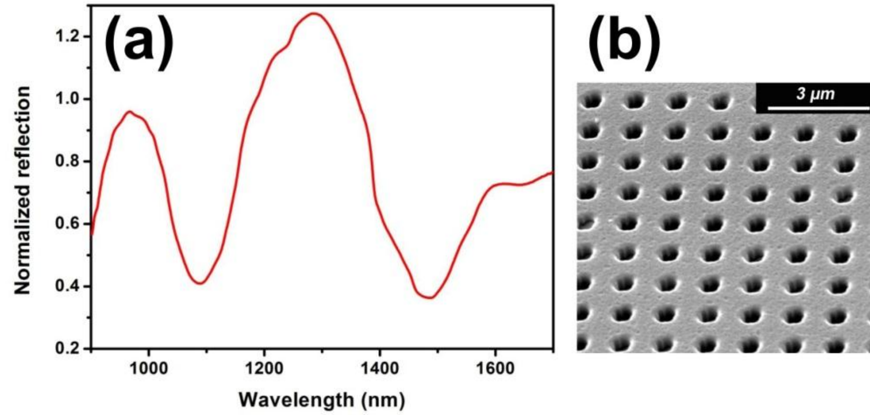

Figure 4.20: (a) Measured normal-incidence reflection spectrum of the fabricated PhC slabs with square array of holes with a lattice constant of 1.2 μm and radius of 300 nm; (b) SEM images of the PhC slab viewed with a tilted angle of 45°.

the PhC slab has a higher reflectivity than a bulk $LiNbO_3$ sample due to the guided resonances. This feature of PhC slabs makes them useful for the devices in which high reflectivity membranes and mirrors are needed.

In order to investigate the variation of the lattice constant of the PhC slabs, we also fabricated a PhC slab which consists of a square lattice of air holes with a lattice constant a =1.2 μm and radius r =300 nm (r/a = 0.258), as shown in Fig. 4.20 (b). The measured reflection spectrum is shown in Fig 4.20 (a). It can be seen the reflectivity spectrum shows a smooth slope instead of a sharp peak. This result indicates that the variation of the lattice constant has a significant influence on the shape of the reflection spectrum.

4.5 Conclusion

In conclusion, the transmission characteristics of monolithic free-standing $LiNbO_3$ PhC slabs based on Fano resonances have been systematically analyzed numerically and experimentally demonstrated for the first time. The simulation results show that the optical properties of PhC slabs are very sensitive to geometrical variations like slab thickness, radius of air holes and

lattice type. We demonstrate that by decreasing the slab thickness or using a triangular lattice, a lower number of modes will be generated, leading to better performance for filter and modulator applications in $LiNbO_3$. In addition, the quality factor of these resonances can be improved by decreasing radius of holes. Furthermore, polarization-dependent transmission properties were also investigated and the results show that in x-cut $LiNbO_3$ similar spectra can be obtained for different polarizations but there is around a 25 nm blue shift for z-polarized light. Our $LiNbO_3$ PhC slab provides a greater flexibility for controlling the polarization dependence of the reflectance. These investigations will give guidance in the design of PhC slabs in $LiNbO_3$.

Then free-standing monolithic $LiNbO_3$ PhC slabs with different dimensional parameters are successfully fabricated by a simple method combined with ion implantation and FIB milling. Our ability to form such structures as reported here is important not only for traditional photonics applications, but for potential quantum optical information processing applications. Optical measurements of slabs over a broad spectral range of 900-1600 nm indicate that more guided modes can be excited with larger radii, which verify the simulation results. The measured results also show high reflectivity over a 200 nm band in the near infrared region. Moreover, excellent agreement was obtained between measurement results of the reflection spectra and simulation analysis results from 3D FDTD.

Our results shows that free-standing $LiNbO_3$ PhC slabs based on Fano resonances have potential applications for various photonic devices like tunable optical filters, sensors, and quantum optics applications where a high quality, single crystal $LiNbO_3$ may be useful.

References

[1] E. Yablonovitch, "Inhibited spontaneous emission in solid-state physics and electronics," Physical Review Letters **58**, 2059-2062 (1987).

[2] S. Y. Lin, J. G. Fleming, D. L. Hetherington, B. K. Smith, R. Biswas, K. M. Ho, M. M. Sigalas, W. Zubrzycki, S. R. Kurtz, and J. Bur, "A three-dimensional photonic crystal operating at infrared wavelengths," Nature **394**, 251-253 (1998).

[3] Z. Zhang and M. Qiu, "Compact in-plane channel drop filter design using a single cavity with two degenerate modes in 2D photonic crystal slabs," Optics Express **13**, 2596-2604 (2005).

[4] W. Park and C. J. Summers, "Extraordinary refraction and dispersion in two-dimensional photonic-crystal slabs," Optics Letters **27**, 1397-1399 (2002).

[5] L.-M. Li, "Two-dimensional photonic crystals: Candidate for wave plates," Applied Physics Letters **78**, 3400-3402 (2001).

[6] S. G. Johnson, S. Fan, P. R. Villeneuve, J. D. Joannopoulos, and L. A. Kolodziejski, "Guided modes in photonic crystal slabs," Physical Review B **60**, 5751-5758 (1999).

[7] K. B. Crozier, V. Lousse, O. Kilic, S. Kim, S. Fan, and O. Solgaard, "Air-bridged photonic crystal slabs at visible and near-infrared wavelengths," Physical Review B **73**, 115126 (2006).

[8] S. Fan and J. D. Joannopoulos, "Analysis of guided resonances in photonic crystal slabs," Physical Review B **65**, 235112 (2002).

[9] R. K. Adair, C. K. Bockelman, and R. E. Peterson, “Experimental corroboration of the theory of neutron resonance scattering,” Physical

Review **76**, 308 (1949).

[10] A. B ̈arnthaler, S. Rotter, F. Libisch, J. Burgd ̈orfer, S. Gehler, U. Kuhl, and H.-J. St ̈ockmann, “Probing decoherence through fano resonances,” Physical Review Letters **105**, 056801 (2010).

[11] F. Hao, Y. Sonnefraud, P. V. Dorpe, S. A. Maier, N. J. Halas, and P. Nordlander, "Symmetry breaking in plasmonic nanocavities: Subradiant LSPR sensing and a tunable Fano resonance," Nano Letters **8**, 3983-3988 (2008).

[12] K. Koshino, "Analytic approach to the optical response of one-dimensional photonic crystal slabs," Physical Review B **67**, 165213 (2003).

[13] S. Fan, W. Suh, and J. D. Joannopoulos, "Temporal coupled-mode theory for the Fano resonance in optical resonators," Journal of the Optical Society of America A **20**, 569-572 (2003).

[14] L. Babi and M. J. A. de Dood, "Interpretation of Fano lineshape reversal in the reflectivity spectra of photonic crystal slabs," Optics Express **18**, 26569-26582 (2010).

[15] P. Pottier, L. Shi, and Y.-A. Peter, "Determination of guided-mode resonances in photonic crystal slabs," Journal of the Optical Society of America B **29**, 109-117 (2012).

[16] R. Magnusson, D. Shin, and Z. S. Liu, “Guided-mode resonance Brewster filter,” Optics Letters **23**, 612–614 (1998).

[17] D. L. Brundrett, E. N. Glytsis, and T. K. Gaylord, “Normal-incidence guided-mode resonance filters: Design and experimental demonstration,” Optics Letters **23**, 700–702 (1998).

[18] Z. S. Liu, S. Tibuleac, D. Shin, P. P. Young, and R. Magnusson,

“High-efficiency guided-mode resonance filter,” Optics Letters **23**, 1556–1558 (1998).

[19] V. Lousse, W. Suh, O. Kilic, S. Kim, O. Solgaard, and S. Fan, "Angular and polarization properties of a photonic crystal slab mirror," Optics Express **12**, 1575-1582 (2004).

[20] C. H. Bui, J. J. Zheng, S. W. Hoch, L. Y. T. Lee, J. G. E. Harris, and C. W. Wong, "High-reflectivity, high-Q micromechanical membranes via guided resonances for enhanced optomechanical coupling," Applied Physics Letters **100**, 021110 (2012).

[21] A. Rosenberg, M. Carter, J. Casey, M. Kim, R. Holm, R. Henry, C. Eddy, V. Shamamian, K. Bussmann, S. Shi, and D. Prather, "Guided resonances in asymmetrical GaN photonic crystal slabs observed in the visible spectrum," Optics Express **13**, 6564-6571 (2005).

[22] S. Kim, S. Hadzialic, A. S. Sudbo, and O. Solgaard, "Reflectivity and polarization dependence of polysilicon single-film broadband photonic crystal micro-mirrors," Optics Express **20**, 6306-6315 (2012).

[23] J. Il Woong, S. Kim, and O. Solgaard, "High-Reflectivity Broadband Photonic Crystal Mirror MEMS Scanner With Low Dependence on Incident Angle and Polarization," Journal of Microelectromechanical Systems **18**, 924-932 (2009).

[24] W. Suh, M. F. Yanik, O. Solgaard, and S. H. Fan, "Displacement-sensitive photonic crystal structures based on guided resonance in photonic crystal slabs," Applied Physics Letters **82**, 1999-2001 (2003).

[25] Z. Weidong, M. Zhenqiang, Y. Hongjun, Q. Zexuan, Q. Guoxuan, P. Huiqing, C. Li, Y. Weiquan, C. Santhad, and Z. Deyin, "Flexible photonic-crystal Fano filters based on transferred semiconductor

nanomembranes," Journal of Physics D **42**, 234007 (2009).

[26] Lj. Babić and M. J. de Dood, "Interpretation of Fano lineshape reversal in the reflectivity spectra of photonic crystal slabs," Optics Express **18**, 26569–26582 (2010).

[27] A. Tavlove, "Computational Electrodynamics: The Finite-Difference Time-Domain Method," Artech House, Norwood, 1995.

[28] W. Suh, O. Solgaard, and S. Fan, "Displacement sensing using evanescent tunneling between guided resonances in photonic crystal slabs," Journal of Applied Physics **98**, 033102 (2005).

[29] S. D. Smith, H. D. Riccius, and R. P. Edwin, "Refractive indices of lithium niobate," Optics Communications **17**, 332–335 (1976).

[30] K. B. Crozier, V. Lousse, O. Kilic, S. Kim, S. Fan, and O. Solgaard, "Air-bridged photonic crystal slabs at visible and near-infrared wavelengths," Physical Review B **73**, 115126 (2006).

[31] F. Schrempel, T. Gischkat, H. Hartung, T. Hoche, E. B. Kley, A. Tunnermann, and W. Wesch, "Ultrathin membranes in x-cut lithium niobate," Optics Letters **34**, 1426-1428 (2009).

Chapter 5 $LiNbO_3$ PhC waveguide

5.1 Introduction

Integrated optical devices based on waveguides have received considerable attention due to the rapid expansion of optical communication systems. PhCs, which can provide PBGs, are one of the most promising tools to reduce the size of optical components and realize condensed PICs. Light in PhC waveguides can be very effectively guided, resulting in 100% transmission through sharp bends [1]. In addition, by incorporating PhC waveguides into an MZI configuration, modulators with interaction length on the order of hundreds of micrometers can be accomplished [2, 3].

However, such PhC waveguides are mostly fabricated on SOI [4] and GaAs [5]. These materials show low EO coefficients and/or slow responses. Consequently, it is important to apply PhCs in active and nonlinear materials, which offer the ability to tune the PhC properties flexibly. Moreover, the incorporation of nonlinear materials into PBG structures is important for the enhancement of nonlinear light-matter interaction. In order to accomplish these aims, fabrication know-how must be mastered yet it remains relatively uncharted for $LiNbO_3$.

In this chapter we demonstrate PhCs in APE $LiNbO_3$ waveguides produced by FIB milling. The thickness and the composition profiles of the APE waveguides were measured using the secondary ion mass spectroscopy (SIMS) method. Then experimental characterization of the PhC waveguides was performed.

5.1.1 APE technique

$LiNbO_3$ waveguides have been traditionally fabricated by the Ti indiffusion method. This method is a preferred fabrication technique and is widely used to produce commercial modulators. However, problems still exist: 1. The indiffusion process requires high temperatures (normally > 1000°C) and long diffusion durations (usually > 10 hours). In addition, during the high temperature process, Ti indiffusion is usually accompanied by Li_2O outdiffusion. This outdiffusion gives rise to an increase of extraordinary refractive index, leading to the formation of an additional planar waveguide when a channel waveguide is chiefly desired. Moreover, Ti indiffused waveguides have a low photorefractive damage threshold, which means irradiation with even a low power beam can induce the index changes. This phenomenon is a nonlinear optical effect and is caused by the titanium which is considered as an ionizable impurity. As a result, Ti indiffused waveguides can only work with incident light of only a few microwatts power at $\lambda = 633$ nm. These drawbacks lead researchers to investigate other fabrication techniques.

An alternative method is the APE technique in which only a low temperature less than 250°C is required. In the 1980s Jackel *et al.* investigated metal exchange in $LiNbO_3$ and concluded that hydrogen entering into a wafer gave rise to the formation of waveguides [6]. After this breakthrough work the first PE waveguide was fabricated by using benzoic acid [7]. The measurement results showed that after the PE process the refractive index profile of $LiNbO_3$ near the surface was step-like and the extraordinary index change was $\Delta n_e = 0.12$ at $\lambda = 632.8$ nm. For a longer wavelength, the

refractive index change became smaller. As reported in [8], the index change was $\Delta n_e = 0.096$ at $\lambda = 1150$ nm.

The depth of the PE waveguide can be given by the standard diffusion relationship:

$$\mathrm{d} = 2\sqrt{D(T) \times t} \qquad (5-1)$$

where d is the waveguide depth, $D(T)$ is the diffusion coefficient which is dependent on the temperature (T), and t is the exchange time. By using the normalized step index equations Clark *et al.* calculated the diffusion coefficient and found that it obeyed Arrhenius' Law [9]:

$$D(T) = D_0 e^{-E_A/(kT)} \qquad (5-2)$$

where D_0 is the diffusion constant, E_A is the activation energy in electron volts, T is the exchange temperature in degrees Kelvin, and k is Boltzman's constant. Many measured data showed that the x-cut diffusion coefficient is larger than the z-cut coefficient [7, 10]. This is due to the low activation energy in the x-cut $LiNbO_3$ which leads to a faster reaction. It indicates that PE waveguides can be fabricated more easily on x-cut samples with lower temperature and shorter exchange time compared with z-cut samples.

The PE technique is only applied on the x and z-cut $LiNbO_3$ samples due to a surface damage problem occurring in y-cut $LiNbO_3$. However, researchers found that the refractive index of such PE waveguides was not stable and the EO and nonlinear coefficients were reduced. After PE, the exchange region became a cubic lattice structure which exhibited little EO property. To solve these problems, two methods have been developed. One is to use benzoic acid diluted with lithium benzoate which can slow the PE reaction [11]. Another method is to use post thermal annealing at a suitable temperature after the exchange process. As reported in [12], post annealing can reduce the index

instabilities and restore the EO and nonlinear coefficients. In addition, post annealing can reduce scattering and insertion loss. After annealing, the step-like index profile of such APE waveguide becomes a graded index profile.

The APE technique only increases the extraordinary index, while the ordinary index is left virtually undisturbed or even decreased. Consequently APE waveguides are polarizing waveguides: only TE modes are supported in x-cut APE waveguides and TM modes are supported in z-cut APE waveguides. Although a lot of work has been carried out on APE waveguides, it is clear that fabrication imperfection strongly affects waveguide performance and this created the need for further research to fabricate practical devices.

5.1.2 PhCs in APE waveguides

The fabrication of PhCs on $LiNbO_3$ is a crucial task toward practical PhC-based active photonic devices. However, PhC structures are very hard to realize on $LiNbO_3$ substrate due to its well-known resistance towards standard machining techniques. Many etching techniques are applied to patterned $LiNbO_3$ such as wet etching by HF based etchants [13], ICP [14], and FIB milling. FIB milling is one of the most attractive techniques for fabricating micro and nano patterns with a high aspect ratio [15]. It can define patterns directly on most dielectrics without using any mask. Recently PhC structures on APE waveguide have been realized by the FIB method [16-18]. It has been demonstrated theoretically as well as experimentally that PhC-based devices realized in $LiNbO_3$ show numerous interesting effects.

In 2005, Baida's group fabricated 2D PhCs on a $LiNbO_3$ substrate by FIB milling [19]. An APE waveguide was realized through PE at 180^oC for 1.5

hours and annealing at 333°C for 9 hours. They showed that a PBG with an extinction ratio of 12 dB was observed in the transmission spectrum. Based on this work, the first EO tunable PhC in $LiNbO_3$ has been realized, as shown in ref. [16]. However, in these demonstrations, the depth of etched air holes was much smaller than the broadly distributed optical modes in APE waveguides. As a result, holes did not reach the center of the optical mode and the contrast of allowed band and prohibited band was quite low. Besides the PhCs with perfect lattice, PhCs with nanocavities also have been fabricated in recent years. Bernal *et al.* realized a PhC with a line defect on an x-cut $LiNbO_3$ substrate [20]. A guided mode was successfully observed by near field characterization.

Recently, in order to overcome the problem of small overlap between the shallow PhC and the buried optical mode, thin film $LiNbO_3$ was used to fabricate PhCs and better transmission properties were obtained. Based on the CIS technique a single-crystalline $LiNbO_3$ film patterned by triangular air holes was fabricated with a BCB barrier layer [21]. Experimentally measured data showed a broad transmission dip between 1300 nm and 1550 nm with an extinction ratio of 15 dB. Very recently, the EO tunability of a 1D PhC with a defect in the middle fabricated on a $LiNbO_3$ thin film was investigated [22]. The transmission band could be shifted by 1.2 nm by applying 30 V but the extinction ratio was less than 2 dB and no distinct PBG was observed. In addition, the CIS technique requires expensive high energy ion implantation engineering, which increases the fabrication cost.

Besides the CIS technique, some other methods have been demonstrated. For example, in a recent work a 380 nm thin film $LiNbO_3$ was deposited on an MgO substrate by pulsed laser deposition [23]. Due to the almost vertical

sidewall of the etched holes, a photonic stop-band edge sharpness was improved and a wavelength shift of only 3 nm was necessary to go from stop band to transmitted band. However there were many drawbacks like poor extinction ratio and a rough surface. Moreover, the deposited $LiNbO_3$ layer was polycrystalline and the EO and nonlinear properties were worse than in the bulk material.

In this Chapter we demonstrate PhCs in APE waveguides produced by FIB milling. The refractive index and the thickness of the waveguide layers can be well controlled in the PE process. The composition of the PE layers is investigated by SIMS. To characterize the performance of the PhCs, the optical transmission spectra of the PhC waveguides are measured and a PBG with clear gap edge is observed.

5.2 Fabrication procedures

In this work, we chose benzoic acid for our PE process because it was less toxic and the required temperature for exchange was low. The $LiNbO_3$ samples used in our experiments were x-cut with two sides polished. It is well known that r_{33} is the highest EO coefficient in $LiNbO_3$. TE polarized light propagating along the y axis is always parallel to the z axis so r_{33} can be utilized. Fig. 5.1 shows a schematic for fabricating the APE waveguides and the PhCs. Firstly, a Cr film with thickness of 100 nm was deposited on the samples by electron beam evaporation. Then a positive photoresist (AZ5214E) was spin-coated onto the surface and the channel waveguide pattern was transferred to the photoresist by standard photolithography. After that, an Ar ion milling was performed to etch the Cr film and form a metal mask for the PE process. The samples were mounted on a stage held at 180 °, which rotated over the duration of the etching.

This led to a uniform etch and smooth sidewalls. Subsequently, photoresist was removed by immersing samples in acetone using an ultrasonic bath for 3 minutes. Then the PE process was performed in molten benzoic acid at 235 ℃ for 5 hours. The process was followed by an annealing of the optical waveguides at 300 ℃ for 2 hours in order to reduce propagation loss. After the channel APE waveguide was formed, the Cr layer was been removed by a commercial Cr etchant. Finally, the samples were cleaved perpendicular to the waveguides, and FIB was used to polish facets at both ends of the waveguide.

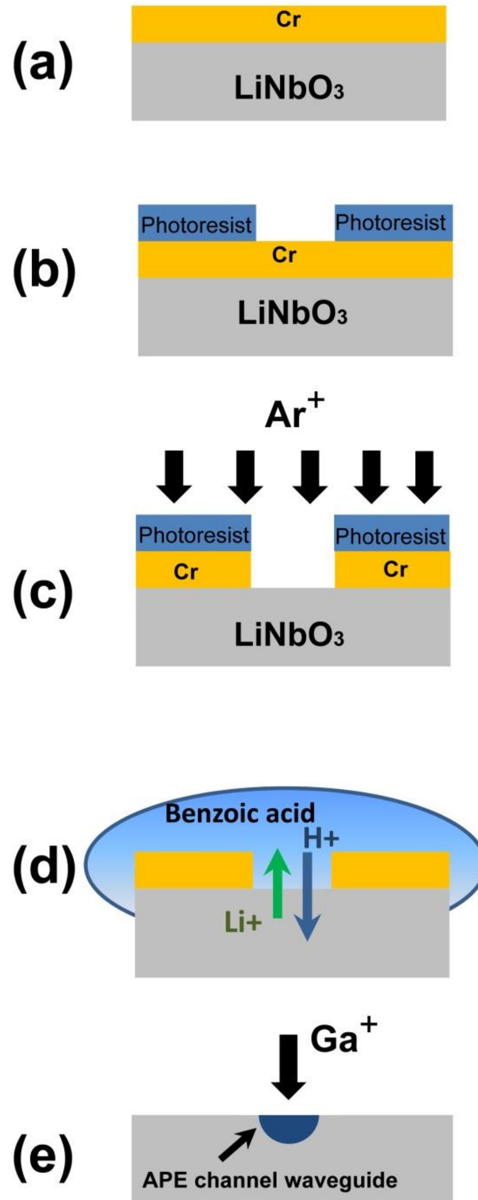

Figure 5.1: Illustration of the process steps to create PhC in an APE waveguide. (a) Cr deposition; (b) Photolithography; (c) Ion milling; (d) PE process; (e) PhC milled by FIB.

FIB was used to mill PhCs consisting of a 13×11 square array of air holes on the surface of the channel waveguides. The beam current used in our experiment was 100 pA and the acceleration voltage was 30 KV. The large current used in this experiment could help to reduce the milling time, which caused the reduction of re-deposition of material onto the sidewalls that would

lead to conical holes. After some calibrations we found that a large current could lead to a larger etching depth, which reached the central location of guided more easily in the APE waveguides. Consequently we decided to etch air holes with large depth because performance strongly depends on the vertical confinement of the propagating guided mode. The total milling time was 26 minutes and the measured etching depth was 2 μm (measurement was performed on a reference sample with the same FIB parameters; a cross section was cut after milling for this). Before etching, a gold layer was coated on the samples for charge dispersal. The designed PhC consists of a lattice constant *a* = 650 nm and *r/a* = 0.308 (*r* is the radius of the air hole).

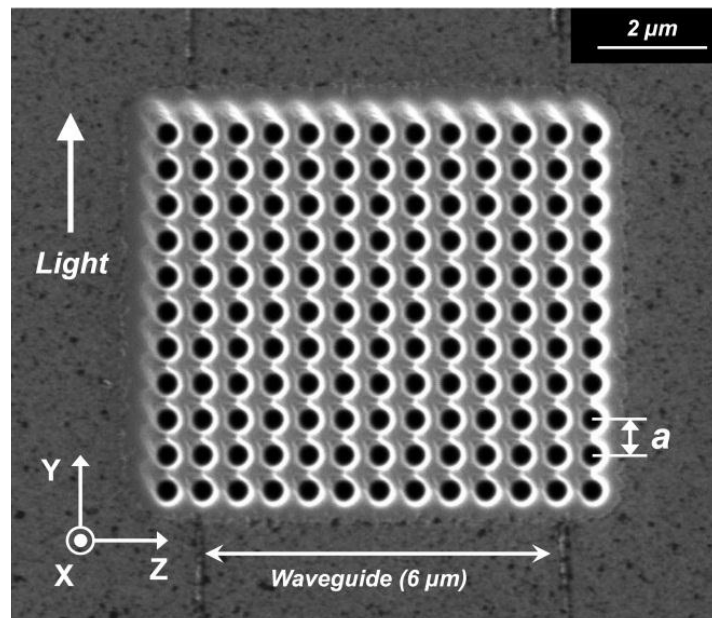

Figure 5.2: SEM image of a fabricated squared lattice PhC on a 6 μm APE waveguide. Light propagates along the y direction of the $LiNbO_3$ crystal.

Figure 5.2 shows the SEM image of a PhC structure milled on an APE waveguide. It can be seen that this type of $LiNbO_3$ PhC illustrated in Fig. 5.2 was fabricated without serious defects. It can be observed that the width of the patterned PhC is slightly larger than the APE waveguide with a width of 6 μm. The reason why we fabricated APE waveguides with large width is that: as

reported, the large width of an APE waveguide could expand the optical mode in the horizontal direction, leading to a confinement of the mode in the vertical direction [17].

5.3 Composition characterization by SIMS

SIMS has already been successfully used to measure H^+ and Li^+ profile simultaneously in a PE $LiNbO_3$ sample [24]. SIMS performs a direct observation of the ion concentration profile as a function of depth and determines the dimensions of a proton exchanged waveguide. In the SIMS analysis, a $LiNbO_3$ wafer is bombarded with heavy ions and a mass spectrometer is used to measure the sputtered ion clusters. In SIMS hydrogen is not sensitive to detection but lithium, niobium and oxygen can be observed directly.

In our experiment, before SIMS measurement a gold layer was coated to prevent charging. Also, in order to prevent charging problems, an electron beam was used to achieve charge compensation. The depth profiles of Li and Nb elements were obtained as shown in Fig. 5.3. It can be seen that an estimated waveguide depth of 3 μm was obtained. From Equation (5-1), the diffusion coefficient which can be estimated in our experiment is 0.45 μm^2/hour for x-cut $LiNbO_3$, which is very close to the value in the reference [25]. From the SIMS curve we can see the Li depletion profile is nearly step-like. There is a small surface peak which is caused by the SIMS equilibration process in the first few nanometers. The Li concentration is quite low near the sample surface and demonstrates a rapid change after the depth of 2.75 μm. Note that the profile is obtained before annealing treatment. Normally after post annealing, the depth of the PE layer will be extended.

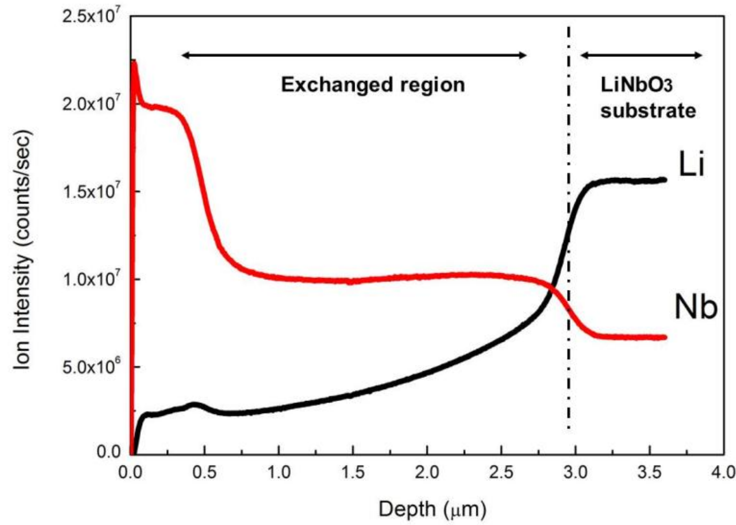

Figure 5.3: SIMS profile of the concentration of Li and Nb vs depth, obtained after PE at 235°C for 5 hours without annealing.

5. 4 Optical characterization

5.4.1 APE waveguide measurement results

In order to measure the spectral transmission of the APE waveguide we used the experimental setup described in Fig. 5.4. A white light source (NKT Photonics Ltd.) was coupled to the APE waveguide through a linear polarizer and a 20 X objective lens. The output beam of white light source contained a broad spectrum ranging from 500 nm to 2000 nm with the peak output power occurring at 1064 nm. A digital microscope was placed on top of the sample to

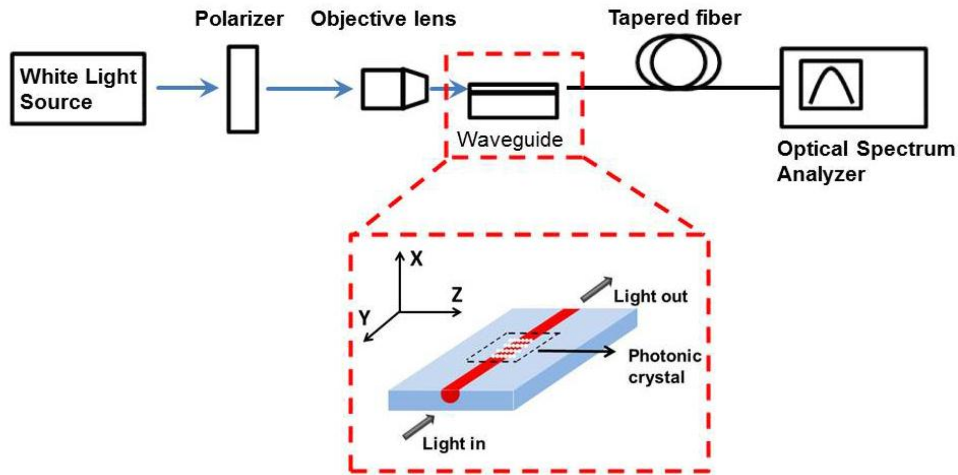

Figure 5.4: Schematic of the transmission spectra measurement.

obtain a top view of the waveguides. It is well known that an x-cut proton exchanged waveguide can only support a TE mode while a z-cut waveguide can only support a TM mode. The polarizer was used to make sure the incident light was TE polarized.

Figure 5.5 (a) and (b) show top view of light incident into APE waveguide with a width of 6 μm. It can be seen from Fig. 5.5 (a) that TE polarized light can be strongly coupled into the waveguide. By contrast, a weak coupling occurs between TM polarized light and waveguide, as shown in Fig. 5.5 (b). Firstly the near-field image of waveguide output was observed by an infrared camera through an objective lens. Fig. 5.5(c) shows the output image from the APE waveguide. A good confinement was observed in the channel waveguide. In order to obtain broadband transmission spectrum, the transmitted light was collected in an optical spectrum analyzer (Agilent 8614A) using a lensed fiber, as shown in Fig. 5.5(d).

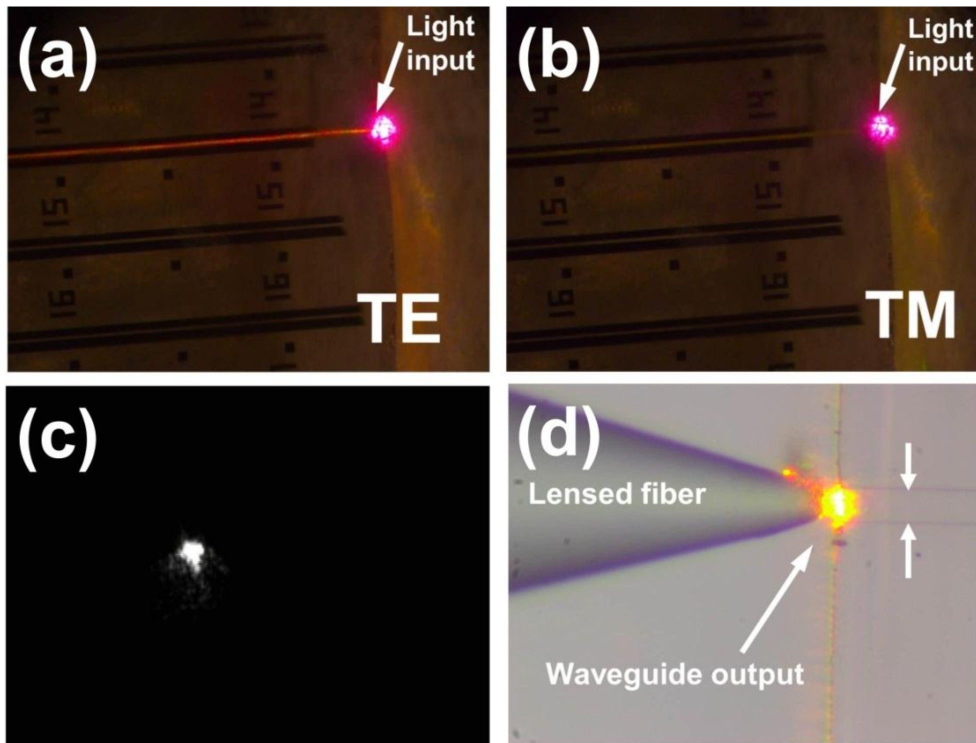

Figure 5.5: (a) Light of TE mode propagates a 6 μm APE waveguide; (b) light of TM mode incidents to the APE waveguide and a weak coupling occurs; (c) CCD image of the APE waveguide illuminated at a wavelength of 532 nm; (d) the output of waveguide is collected using a lensed fiber.

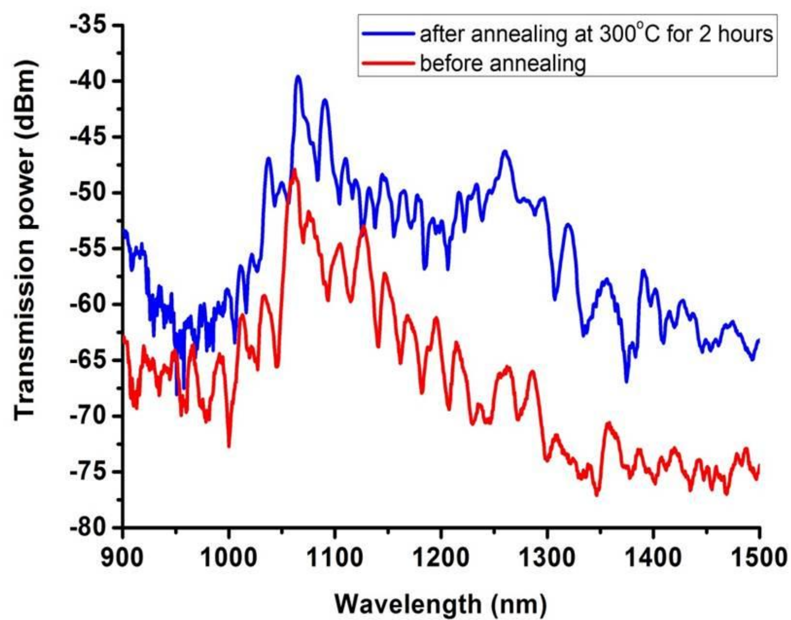

Figure 5.6: Transmission spectra of the APE channel waveguide before and after thermal annealing.

Figure 5.6 shows the broadband transmission characteristics of the APE channel waveguide before and after thermal annealing. From Fig. 5.6 we can see a considerable difference in the transmitted power. After thermal annealing, the propagation loss of the APE waveguide was significantly reduced. At a wavelength of 1064 nm, the transmitted power was increased from -47.9 dBm to -39.8 dBm. Annealing affects the transmission characteristics stronger in the longer wavelength range (1200-1500 nm) than in the shorter wavelength range (900-1000 nm). It can be concluded that in order to achieve good waveguide performance, thermal annealing is necessary in APE waveguide fabrication processes. Not that the oscillations in the spectrum may due to the Fabry–Pérot resonances reflected at the polished facets of the sample.

5.4.2 Transmission spectrum of PhC waveguide

Figure 5.7 (a) shows the top view as TE polarized light propagates through a PhC waveguide. It can be seen that a large scattering loss is introduced due to the PhC. Fig. 5.7 (b) shows the measured transmission spectra for the APE waveguide before and after milling PhC. A PBG can be observed clearly in the PhC waveguide, which does not appear in the transmission though the standard APE waveguide. It can be seen from Fig. 5.7 (b) that a sharp PBG edge is obtained. This result indicates that the performance of PhCs can be improved by enlarging the depth of air holes and widening the width of the APE waveguide. An extinction ratio is estimated from Fig. 5.7 (b) to be approximately 15 dB.

From Fig. 5.7 (b) it can also be seen that the milled PhC causes additional propagation loss compared with a standard APE waveguide. This is mainly due to the weak optical confinement of the APE waveguide. The curve in Fig. 5.7 (b)

shows low contrast between the photonic permitted and forbidden bands, and the stop band is very narrow. This is due to the effects of finite hole depth and non-cylindrical hole shape. It is reported that conical holes of any depth fail to produce well defined stop-bands in the transmission spectra unless the sidewall angle is within 0.5 of vertical [26]. However, it is very hard to realize in a standard $LiNbO_3$ substrate by FIB milling.

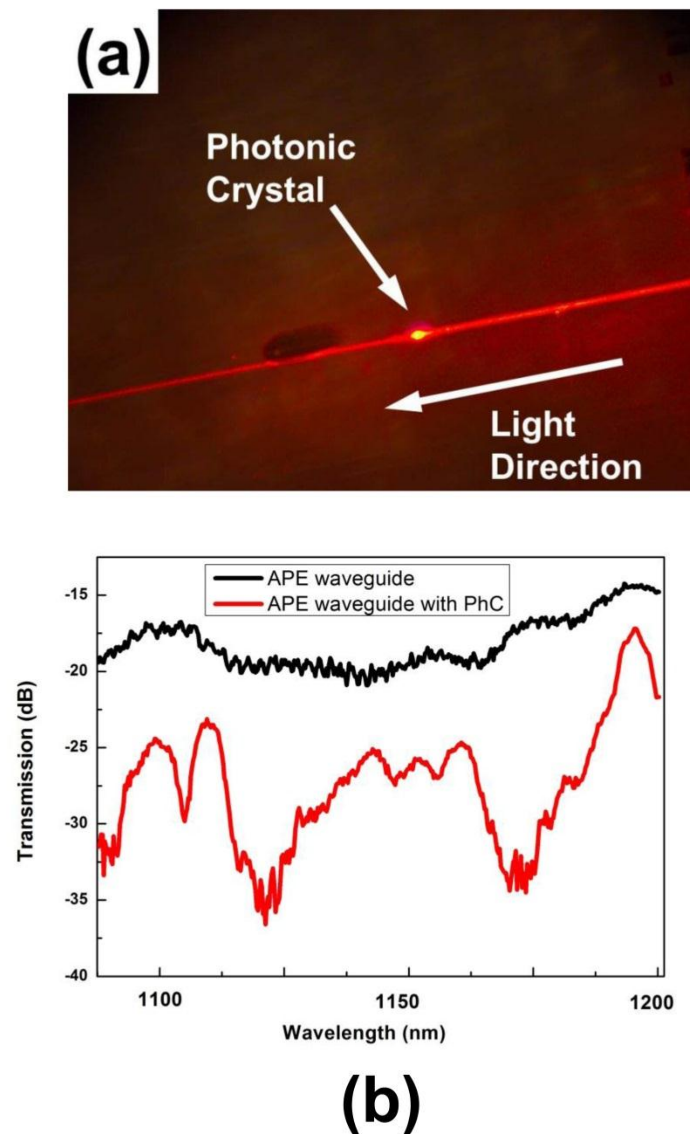

Figure 5.7: (a) Light of TE mode propagates through a PhC waveguide; (b) Measured optical transmission spectra through the PhC (red line) and through a standard APE $LiNbO_3$ waveguide (black line).

5.5 Conclusion

In this work we successfully fabricated and measured PhCs patterned on a $LiNbO_3$ APE waveguide. SIMS data indicate that after 5 hours exchange time a PE layer of 3 μm can be obtained. The depth of holes was 2 μm by applying a large milling current. We presented experimental characterization of the PhC waveguide and a well-defined PBG was observed from the transmission spectra. An extinction ratio was estimated to be approximately 15 dB. Optical transmission results indicate that deep air holes can lead to a sharp band edge. This PhC waveguide is a good candidate for further development of an ultra-compact, low-voltage $LiNbO_3$ modulator.

References

[1] R. D. Meade, A. Devenyi, J. D. Joannopoulos, O. L. Alerhand, D. A. Smith, and K. Kash, "Novel applications of photonic band-gap materials - low-loss bends and high q-cavities," Journal of Applied Physics **75**, 4753-4755 (1994).

[2] X. Chen, Y. Chen, Y. Zhao, W. Jiang, and R. T. Chen, "Capacitor-embedded 0.54 pJ/bit silicon-slot photonic crystal waveguide modulator," Optics Letters **34**, 602-604 (2009)

[3] L. Gu, W. Jiang, C. Xiaonan, L. Wang, and R. T. Chen, "High speed silicon photonic crystal waveguide modulator for low voltage operation," Applied Physics Letters **90**, 071105 (2007).

[4] A. Lupu, E. Cassan, S. Laval, L. El Melhaoui, P. Lyan, and J. Fedeli, "Experimental evidence for superprism phenomena in SOI photonic crystals," Optics Express **12**, 5690-5696 (2004).

[5] Liang Chen and Elias Towe, "Design of high-Q microcavities for proposed two-dimensional electrically pumped photonic crystal lasers," IEEE Journal on Selected Topics in Quantum Electronics **12** 117-123 (2006).

[6] J. L. Jackel and C. E. Rice, "Variation in waveguides fabricated by immersion of $LiNbO_3$ in $AgNO_3$ and $TlNO_3$: The role of hydrogen," Applied Physics Letters **41**, 508-510 (1982).

[7] J. L. Jackel, C. E. Rice, and J. J. Veselka, "Proton exchange for high-index waveguides in $LiNbO_3$," Applied Physics Letters **41**, 607-608 (1982).

[8] C.Canali, A.Garnera,G.Della Mea, R.M.De La Rue"Proton-exchange LiNbO3 waveguides: material analysis and optical characteristics", Proc. SPIE, vol. 460, pp. 49-55, 1984.

[9] D. F. Clark, A. C. G. Nutt, K. K. Wong, P. J. R. Laybourn, and R. M. De La Rue, " Characterization of proton-exchange slab optical waveguides in z-cut $LiNbO_3$," Journal of Applied Physics **54**, 6218-6220 (1983).

[10] M. Digonnet, M. Fejer, and R. Byer, "Characterization of proton-exchanged waveguides in MgO:$LiNbO_3$," Optics Letters **10**, 235-237 (1985).

[11] M. De Micheli, J. Botineau, S. Neveu, P. Sibillot, D. B. Ostrowsky, and M. Papuchon, "Independent control of index and profiles in proton-exchanged lithium niobate guides," Optics Letters **8**, 114-115 (1983).

[12] A. Loni, G. Hay, R. M. De La Rue, and J. M. Winfield, "Proton-exchanged $LiNbO_3$ waveguides: the effects of post-exchange annealing and buffered melts as determined by infrared spectroscopy,

optical waveguide measurements, and hydrogen isotopic exchange reactions," Journal of Lightwave Technology **7**, 911-919 (1989).

[13] H. Hu, R. Ricken, W. Sohler, and R. B. Wehrspohn, "Lithium niobate ridge waveguides fabricated by wet etching," Photonics Technology Letters **19**, 417-419 (2007).

[14] J. Deng, W. Jia, E. P. Png, G. Y. Si, J. Son, H. Yang, and A. J. Danner, "Deep anisotropic $LiNbO_3$ etching with SF_6/Ar inductively coupled plasmas," Journal of Vacuum Science and Technology B **30**, 011208 (2012).

[15] F. Lacour, N. Courjal, M. P. Bernal, A. Sabac, C. Bainier, and M. Spajer, "Nanostructuring lithium niobate substrates by focused ion beam milling," Optical Materials **27**, 1421–1425 (2005).

[16] M. Roussey, M. P. Bernal, N. Courjal, D. Van Labeke, F. I. Baida, and R. Salut, "Electro-optic effect exaltation on lithium niobate photonic crystals due to slow photons," Applied Physics Letters **89**, 241110-241111 (2006).

[17] Nadège Courjal, Jean Dahdah, Gwenn Ulliac, Pierre Sevillano, Blandine Guichardaz, and Fadi Baida, "Optimization of $LiNbO_3$ photonic crystals: toward 3D $LiNbO_3$ micro-components," Optics Express **19**, 23008-23016 (2011).

[18] N. Courjal, S. Benchabane, J. Dahdah, G. Ulliac, Y. Gruson, and V. Laude, "Acousto-optically tunable lithium niobate photonic crystal," Applied Physics Letters **96**, 131103 (2010).

[19] M. Roussey, M.-P. Bernal, N. Courjal, and F. I. Baida, "Experimental and theoretical characterization of a lithium niobate photonic crystal," Applied Physics Letters **87**, 241101-241103 (2005).

[20] M. P. Bernal, N. Courjal, J. Amet, M. Roussey, and C. H. Hou, "Lithium

niobate photonic crystal waveguides: Far field and near field characterisation," Optics Communications **265**, 180-186 (2006).

[21] F. Sulser, G. Poberaj, M. Koechlin, and P. Günter, "Photonic crystal structures in ion-sliced lithium niobate thin films," Optics Express **17**, 20291-20300 (2009).

[22] H. Lu, B. Sadani, N. Courjal, G. Ulliac, N. Smith, V. Stenger, M. Collet, F. I. Baida, and M. P. Bernal, "Enhanced electro-optical lithium niobate photonic crystal wire waveguide on a smart-cut thin film," Optics Express **20**, 2974-2981 (2012).

[23] S. Diziain, S. Harada, R. Salut, P. Muralt, and M. P. Bernal, "Strong improvement in the photonic stop-band edge sharpness of a lithium niobate photonic crystal slab," Applied Physics Letters **95,** 101103 (2009).

[24] C. Canali, A. Carnera, G. Della Mea, P. Mazzoldi, S. M. Al Shukri, A. C. G. Nutt, and R. M. De La Rue, "Structural characterization of proton exchanged $LiNbO_3$ optical waveguides," Journal of Applied Physics **59**, 2643-2649 (1986).

[25] S. Forouhar, C. Warren, R. X. Lu, and W. S. C. Chang, "Techniques For Fabricating High Index Overlay Films On $LiNbO_3$," Proceedings of SPIE **408**, 6-13 (1983).

[26] G. W. Burr, S. Diziain, and M. P. Berna, "The impact of finite-depth cylindrical and conical holes in lithium niobate photonic crystals," Optics Express **16**, 6302-6316 (2008).

Chapter 6 Conclusion and Future Work

6.1 Conclusion

In this thesis, different fabrication methods have been explored and developed toward the goal of PICs on the $LiNbO_3$ platform. Three main types of structures, deep anisotropic ridges, free-standing structures and PhCs were successfully fabricated in bulk $LiNbO_3$ substrates.

In order to fabricate ridge waveguides, which would be key components in future compact integrated devices, ICP etching properties of $LiNbO_3$ were investigated. It was found that surface roughness can be avoided significantly by carefully choosing etching conditions like metallic mask and gases. Deep and highly anisotropic ridge structures with ultra-smooth surfaces and vertical sidewalls were achieved. In order to achieve sidewall smoothness of etched ridges, Ar GCIB irradiations were employed in the post etching process and ridges with both smooth surfaces and sidewalls were obtained. The significance of the GCIB method is that it provides a powerful tool to reduce sidewall roughness, which is a major problem in $LiNbO_3$ etching techniques. These results are of considerable importance since they provide low loss deep ridge waveguides, which are crucial to fabricate $LiNbO_3$ modulators with low driving voltage and compact size.

This study also developed a novel monolithic approach to fabricate suspended $LiNbO_3$ structures by employing ion implantation and selectively wet etching. SRIM simulation was used to design implantation profiles and results were in good agreement with fabrication results. Suspended slabs with different thicknesses were obtained by choosing different implantation

energies. An air gap with thickness over 1 μm between suspended slab and substrate was achieved by multiple energy implantations, which was good for optical isolation. By incorporating FIB milling into the monolithic approach, complicated optical components including suspended waveguides and microdisks were realized in bulk $LiNbO_3$. One major contribution of these suspended structures with smooth surfaces is that they have high refractive index contrast and unique functionalities, which allow more flexible design of PICs on $LiNbO_3$ platform instead of only waveguides.

In addition, another important contribution of this monolithic method is that it allows the realization of cylindrical holes with vertical sidewalls, which is important for PhC devices but is hard to obtain by standard FIB milling. Thanks to this, free-standing $LiNbO_3$ PhC slabs with controllable thickness and vertical PhC profile were successfully fabricated. The out-of-plane properties of such slabs under free-space illumination were theoretically analyzed using 3D FDTD simulation. It was found that the transmission spectrum of such slabs show some interesting peaks because of the Fano resonance and can be controlled by varying design parameters such as radius of holes, slab thickness and polarization of incident light. Optical measurements of fabricated free-standing $LiNbO_3$ PhC slabs with different dimensional parameters were carried out and the results were in agreement with simulation. This study is the first one to demonstrate Fano phenomena in $LiNbO_3$ PhC slabs theoretically and experimentally. These findings are significant since they suggest a new perspective of the application of $LiNbO_3$ in free-space tunable devices and provide a new platform to study nonlinear light-matter interaction.

Since photonic crystals have a great potential to reduce the size and

increase the functionality of PICs, we also performed an exploratory study on in-plane transmission properties of photonic crystals in conventional APE $LiNbO_3$ waveguides. Fabrication procedures were demonstrated and it was found that annealing is a critical issue to obtain low loss APE waveguides. Measurement of transmission spectra of PhC waveguides was performed and photonic band gaps of PhC were observed. The significance of PhCs in APE waveguides, in view of its slow light effect, is that it provides a new strategy to reduce the interaction length of $LiNbO_3$ modulators, allowing the realization of modulators in micrometer scale.

6.2 Future Work

Based on the experimental results obtained from this study, some potential areas for further investigations are highlighted below.

6.2.1 Extended research on free-standing PhC slabs

A direct extension of this work is to introduce point and line defects into PhC slabs and to exam their optical performance under free-space illumination. In order to obtain accurate measurement results, large area PhCs need to fabricated. However, such PhC slabs with large area would be broken easily due to lattice defects introduced by implantations. To address this problem, further fabrication methods need to be explored. For example, thermal annealing after implantations may be a good choice.

One of the most important features of $LiNbO_3$ is its EO response. However, being a preliminary study, this work only showed passive measurements on free-standing $LiNbO_3$ PhC slabs. Thus further research is needed to investigate the EO tunability of such slabs. To achieve this, more

fabrication steps like photolithography and electrodes deposition are required. Because the free-standing slabs are fragile, a possible solution is to deposit electrodes prior to the formation of suspended slabs.

6.2.2 Optical microcavities fabrication in APE waveguides and nonlinear effect investigation

Since the fabrication methods for different structures in micrometer and nanometer scales in $LiNbO_3$ have been developed well in this thesis, one interesting avenue for future work is to realize optical microcavities embedded in APE waveguides. Such optical cavities at the micrometer scale volume could provide a strong optical resonance in $LiNbO_3$, which is expected to enhance nonlinear light-matter interactions [1]. For example, SHG in $LiNbO_3$ could be enhanced greatly. One possible strategy to explore is to create a Fabry–Perot cavity by two Bragg gratings. Another method is to introduce a point defect in 2D PhCs. In both ways resonance modes could be confined to the interior of the cavities by Bragg reflection in the lateral direction and APE waveguiding in the vertical direction.

The first step towards this exploration has been carried out in this study. SHG was demonstrated in an APE waveguide in z-cut $LiNbO_3$ substrate. The waveguide was fabricated by immersing $LiNbO_3$ substrates in melted benzoic acid at 230 ^{o}C for 3 hours, followed by annealing at 330 ^{o}C for 2 hours. A light with the peak output power occurring at 1064 nm was coupled into the waveguide and green light was generated, as shown in Fig. 6.1. By employing optical microcavities, the conversion efficiency of such SHG could be greatly improved.

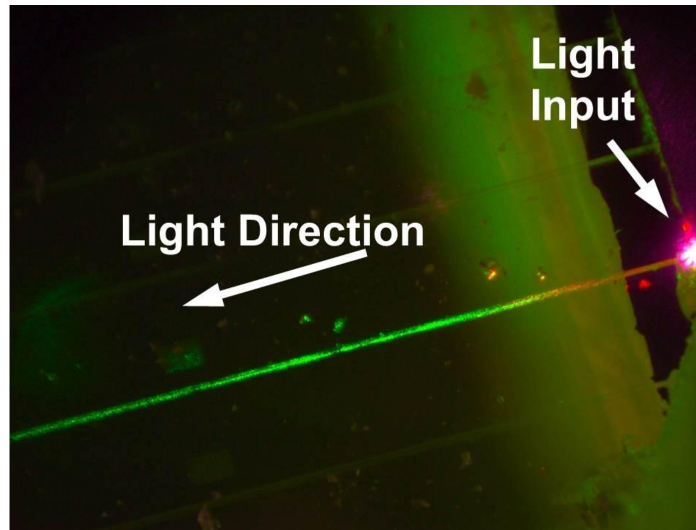

Figure 6.1: Optical microscope image showing SHG in an APE $LiNbO_3$ waveguide.

6.2.3 Ring resonators used in microwave photonics

Although APE waveguides have been studied for many years, there is still much work that can be done to develop new devices, like ring resonators. Ring resonators, which have compact size and good wavelength-selective properties [2], are promising components to be embedded in PICs. They have been realized in a variety of materials including SOI [3], GaAs [4] and polymers [5]. However, few ring resonators have been realized in $LiNbO_3$. Ring resonators in $LiNbO_3$ allow direct electrical control, leading to an ultrafast modulation response. Additionally, $LiNbO_3$ ring resonators promise to become important components in mm-wave modulation with simultaneous RF and optical resonances [6, 7]. Moreover, such resonators also provide a straightforward way to couple between optical and microwave fields, enabling potential quantum information processing capabilities [8].

To demonstrate the possibilities of further research in this area, a ring resonator was fabricated in x-cut $LiNbO_3$ substrate by the APE method. A Cr film which served as a hard mask was deposited by electron beam evaporator.

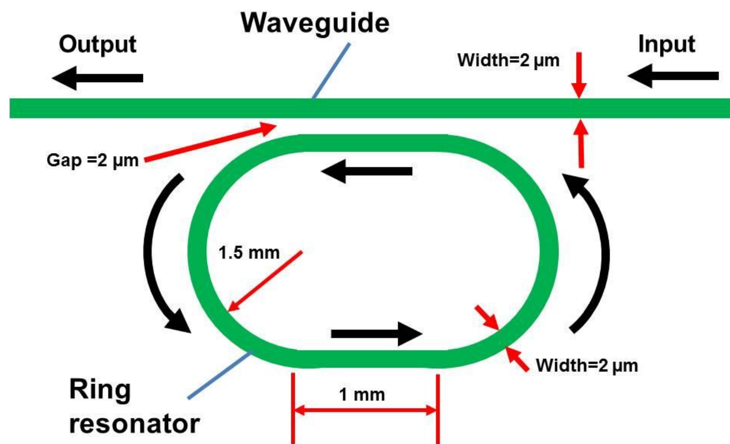

Figure 6.2: Configuration of a ring resonator in $LiNbO_3$.

A ring structure and bus waveguide were patterned by electron beam lithography. After the channel waveguides were formed, the Cr film was removed by a commercial Cr etchant. Fig. 6.2 shows the racetrack configuration of the ring structure and bus waveguides. The width of ring and bus waveguide was 2 μm. The coupling gap between the ring and the bus waveguide was also 2 μm. After thermal annealing, the width of channel APE waveguides was increased so the coupling gap was probably less than 2 μm.

A white light source was used to couple light into the ring resonator. The output beam of the white light source used has a broad spectrum ranging from 500 nm to 1600 nm with the peak output power occurring at 1064 nm. A digital microscope was placed on top of the sample to obtain a top view of the waveguides. The transmitted light was collected into an optical spectrum analyzer using a lensed fiber. Fig. 6.3 shows the top view of the coupling area when light passed through the waveguide. It can be seen that the light is well confined within channel waveguides and efficient coupling occurs between the bus waveguide and the ring structure.

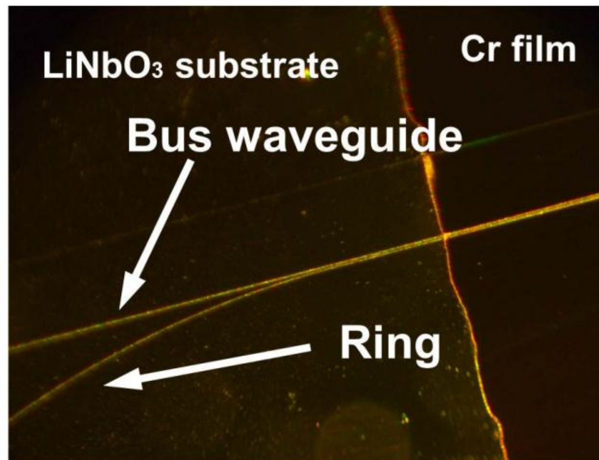

Figure 6.3: Top view of the coupling area when light passed through the waveguide.

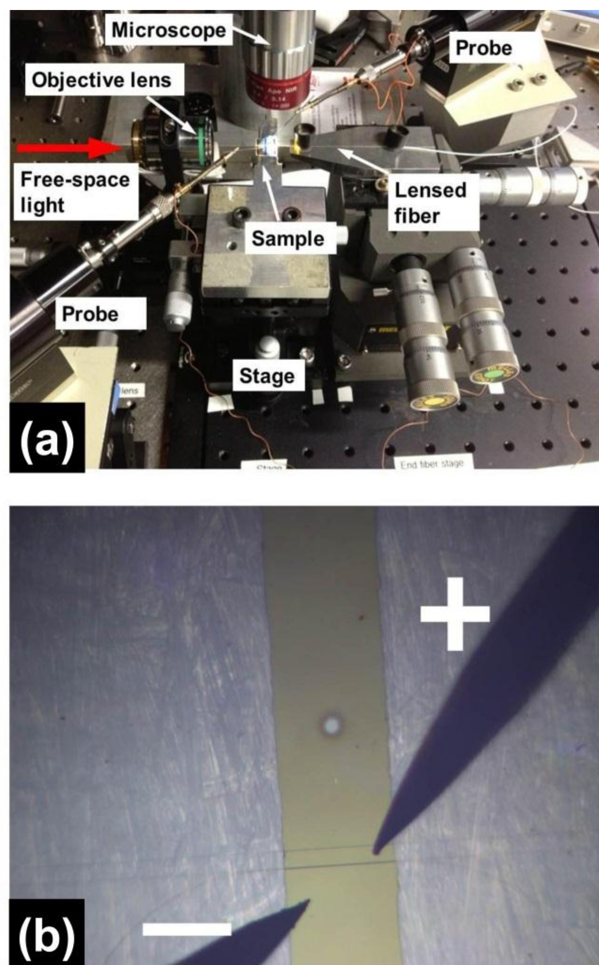

Figure 6.4: (a) Measurement setup to test EO tunability of the $LiNbO_3$ ring resonator; (b) Optical microscope image showing the two probes.

In order to test device tunability via the electro-optic effect, we left part of the Cr film on the coupling area to serve as two electrodes. A source meter was used to apply a DC voltage via two probes. The active measurement setup is shown in Fig. 6.4 (a) and (b).

We examined the tunability in a wavelength region from 741 nm to 751 nm, as shown in Fig. 6.5. The measured extinction ratio is approximately 13 dB when no external voltage is applied. It can be seen that the resonance is blue shifted when a voltage of 150 V is applied. We have measured the shift for different resonance peaks and estimated the tuning rate for this ring resonator is about 2 pm/V. It can be also seen that the blue shift becomes stronger at longer wavelengths. We believe the ring resonators in $LiNbO_3$ can play an important role in the quantum optics experiments.

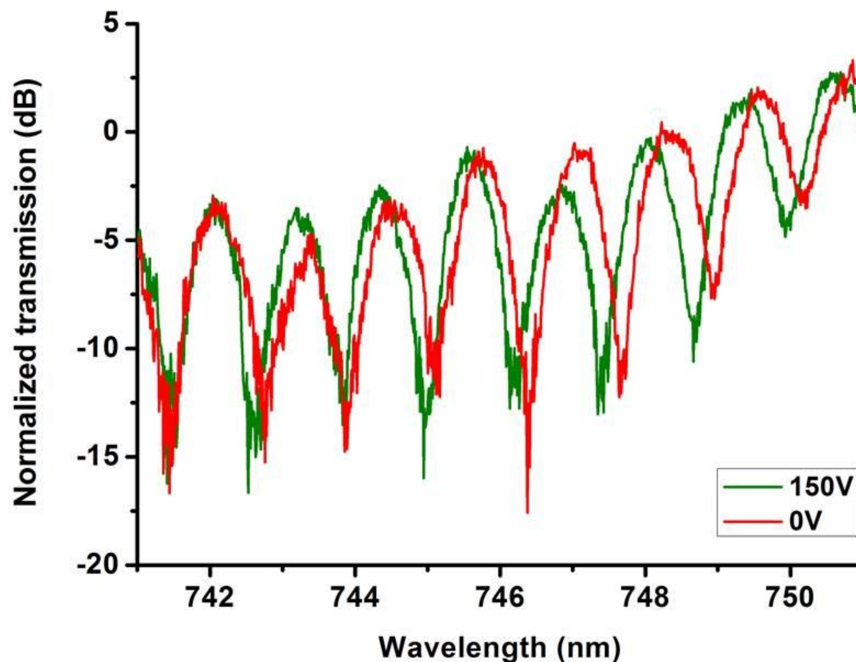

Figure 6.5: Normalized transmission spectra of the ring resonator before (red line) and after (green line) applying voltage (150 V).

References

[1] K. J. Vahala, "Optical microcavities," Nature **424**, 839-846 (2003).

[2] B. E. Little and S. T. Chu, "Toward very large-scale integrated photonics," Optics & Photonics News **11**, 24 (2000).

[3] W. R. Headley, G. T. Reed, S. Howe, L. Ansheng, and M. Paniccia, "Polarization-independent optical racetrack resonators using rib waveguides on silicon-on-insulator" Applied Physics Letters **85**, 5523-5525 (2004).

[4] L. Ding, C. Baker, P. Senellart, A. Lemaitre, S. Ducci, G. Leo, and I. Favero., "High frequency GaAs nano-optomechanical disk resonator" Physical Review Letters **105**, 263903 (2010).

[5] B. Bortnik, Y. C. Hung, H. Tazawa, S. Byoung-Joon, L. Jingdong, A. K. Y. Jen, W. H. Steier, H. R. Fetterman, "Electrooptic polymer ring resonator modulation up to 165 GHz" IEEE Journal of Selected Topics in Quantum Electronics **13**, 104-110 (2007).

[6] D. A. Cohen, M. Hossein-Zadeh, and A. F. J. Levi, "Microphotonic modulator for microwave receiver," Electronics Letters **37**, 300-301 (2001).

[7] M. Hossein-Zadeh and A. F. J. Levi, "Self-homodyne RF-optical $LiNbO_3$ microdisk receiver," Solid-State Electronics **49**, 1428-1434 (2005).

[8] M. Tsang, "Cavity quantum electro-optics," Physical Review A **81**, 063837 (2010).

Appendix: publications

Journal Papers

1. Jun Deng, Sajid Hussain, Vanga S. Kumar, Wei Jia, Ching E. Png, Lim S. Thor, Andre A. Bettiol, and Aaron J. Danner, "Modeling and experimental investigations of Fano resonances in free-standing $LiNbO_3$ photonic crystal slabs," Optics Express **21**, 3243-3252 (2013).
2. Jun Deng, Wei Jia, Ching E. Png, Gangyuan Si, Jaesung. Son, Hyunsoo Yang, and Aaron J. Danner, "Deep anisotropic $LiNbO_3$ etching with SF_6/Ar inductively coupled plasmas," Journal of Vacuum Science and Technology B **30**, 011208 (2012).
3. Wei. Jia, Jun Deng, Ajeesh. M. Sahadevan, Hong Wu, Liyong Jiang, Xiangyin Li, Charanjit. S. Bhatia, Hyunsoo Yang, and Aaron J. Danner, "Design and fabrication of high efficiency power coupler between different photonic crystal waveguides," Applied Physics Letters **98**, 241102 (2011).
4. Wei Jia, Jun Deng, Hong Wu, Xiangyin Li, and Aaron J. Danner, "Design and fabrication of high-efficiency photonic crystal power beam splitters," Optics. Letters **36**, 4077-4079 (2011).
5. Wei Jia, Jun Deng, Benjamin P. L. Reid, Xu Wang, Christopher C. S. Chan, Hong Wu, Xiangyin Li, Robert A. Taylor, and Aaron J. Danner, "Design and fabrication of optical filters with very large stopband (≈ 500 nm) and small passband (1 nm) in silicon-on-insulator," Photonics and Nanostructures **10**, 447-451 (2012).

Conference Papers

1. Jun Deng, Sajid Hussian, Soham Saha, Ching Eng Png, Mankei Tsang, Aaron Danner, "Optical microring resonators in lithium niobate for

classical and quantum microwave photonics," IEEE Conference on Optical MEMS & Nanophotonics, Kanazawa, Japan (2013).

2. Jun Deng, Vanga S. Kumar, Sajid Hussian, H. Gao, S. T. Lim, C. E. Png, X. Ning, A. A. Bettiol, and A. J. Danner, "Free-standing monolithic $LiNbO_3$ photonic crystal slabs," Proceedings of SPIE Photonics West **8632**, San Francisco, USA (2013).
3. Jun Deng, Wei Jia, Vanga. S. Kumar, Ching E. Png, Andrew. A. Bettiol, and Aaron J. Danner, "Photonic crystals in proton-exchanged $LiNbO_3$ waveguides for photonic applications," IEEE Photonics Global Conference, Singapore (2012).
4. Jun Deng, Guangyuan Si, and Aaron J. Danner, "Dry etching of $LiNbO_3$ using inductively coupled Plasma," IEEE Photonics Global Conference, Singapore (2010).